Photoacoustic sensor for in-vivo non-invasive blood glucose measurements

Author:
Said El-Busaidy

Supervisors:
Lars Duggen
Bernd Baumann
Marcus Wolff

A thesis submitted in fulfillment of the requirements for the degree of Doctor of Philosophy

at the

Mads Clausen Institute
University of Southern Denmark

January 8, 2021

Declaration of Authorship

I, Said El-Busaidy, declare that this thesis titled, "Photoacoustic sensor for in-vivo non-invasive blood glucose measurements" and the work presented in it are my own except as cited in the references.

Name: Said El-Busaidy
Signature:

Date:

Abstract

Photoacoustic spectroscopy is an effective techniques for measuring the blood glucose levels non-invasively. The technique detects an acoustic signal generated by probing glucose molecules using mid-infrared radiation. To amplify the generated photoacoustic signal an acoustic resonator is used. One of the resonator ends is left open during the glucose measurements to prevent the build up of humidity inside the resonator that can affect the measurements. The open resonator end deteriorates the signal and thus the sensitivity of the photoacoustic glucose measurements.

This work aims to contribute towards the development of a non-invasive glucose sensor by improving the sensitivity of the measurements. Resonance amplification is strongly dependent on the geometry of the resonator. The resonator geometry is therefore optimized for maximum signal strength and hence improved sensitivity.

The procedure for optimizing the acoustic resonator is described. Accurate simulation models that can calculate the photoacoustic signal from solid samples are developed and evaluated against experimental measurements. The ability of the models to accurately simulate the photoacoustic signal in both the open and closed resonator configuration is demonstrated. One of the models is employed in a numerical shape optimization of the resonator to maximize the detected photoacoustic signal. The optimization results show a significant signal increment that represent a step forward towards developing a non-invasive photoacoustic blood glucose sensor.

Acknowledgements

I would like to express my sincerest appreciation and gratitude to my supervisors Assoc. Prof. Dr. Lars Duggen, Prof. Dr. Bernd Baumann and Prof. Dr. Marcus Wolff. Their patience, advice and guidance made this work possible. I am also thankful to my colleagues at the Heinrich-Blasius Institute Dr. Henry Bruhns, Dr. Alian Loh. Dr. Yannick Saalberg and M.Sc. Sander Vervoot for the numerous technical discussions and for creating a pleasant and joyful research environment.

Furthermore, I would like to thank the Hamburg University of Applied Science Promotionsförderung for funding my doctoral studies.

Finally, I would like to thank my parents for their unconditional trust and support over the years.

Contents

Declaration of Authorship iii

Abstract v

Acknowledgements vii

1 Introduction 1
- 1.1 Diabetes . . . 1
- 1.2 Glucose . . . 1
  - 1.2.1 Structure . . . 1
  - 1.2.2 Invasive measurement . . . 2
- 1.3 Non-invasive glucose measurement . . . 3
  - 1.3.1 Non-optical methods . . . 4
  - 1.3.2 Optical methods . . . 5
- 1.4 Thesis aim and structure . . . 8

2 Photoacoustic spectroscopy 11
- 2.1 Fundamentals . . . 11
  - 2.1.1 Optical source . . . 12
  - 2.1.2 Acoustic resonator . . . 17
  - 2.1.3 Acoustic detector . . . 19
- 2.2 PA glucose measurement . . . 20

3 Numerical simulation of a PA resonator 23
- 3.1 Introduction . . . 23
- 3.2 Finite element method . . . 25
  - 3.2.1 Amplitude mode expansion model . . . 26
  - 3.2.2 Viscothermal model . . . 28
- 3.3 Modelling of a closed resonator . . . 30
  - 3.3.1 Convergence study . . . 31
- 3.4 Modelling of the open resonator . . . 33
  - 3.4.1 Perfectly matched layers . . . 33
  - 3.4.2 Boundary element method . . . 37

4 PA measurement setup 41
- 4.1 Overview . . . 41
- 4.2 Optical source . . . 41
  - 4.2.1 Diode laser . . . 43
  - 4.2.2 Quantum cascade laser . . . 43
- 4.3 Acoustic resonator . . . 45

4.4 Acoustic detector 46
4.5 Results 48
4.5.1 Closed resonator 48
4.5.2 Open resonator 53

5 Optimization of an open PA resonator **57**
5.1 Introduction 57
5.2 Numerical optimization of PA resonators 58
5.3 Optimization method 59
5.3.1 Resonance cylinder sweep 60
5.3.2 Cavity cylinder sweep 63
5.3.3 Optimization model 65
5.4 Optimization results 68
5.4.1 Simulation of optimized resonator 70
5.4.2 Measurement of optimized resonator 70

6 Conclusion and outlook **73**

A MEMS microphone PCB **75**

Bibliography **77**

Chapter 1

Introduction

1.1 Diabetes

Diabetes mellitus is a wide spreading metabolic disease affecting 422 million people as of 2014, and attributed to 1.6 million deaths in 2016 [1]. It is characterized by increment of blood glucose levels caused by either the body's inability to produce insulin (type 1 diabetes) or ineffective use of insulin (type 2 diabetes) [1]. The physiological glucose range for a healthy person is typically between 72 mg/dl to 180 mg/dl [2], [3]. When the blood glucose levels are too low (less than 70 mg/dl), a condition known as hypoglycemia, a person can lose consciousness, have a seizure or even die [4]. In situations where the blood glucose levels are higher than 180 mg/dl, a condition known as hyperglycemia, health complications such as kidney damage, blindness, heart attacks or neuropathy can occur [5].

A cure for diabetes does not exist. Instead patients are required to monitor their glucose levels and regulate it using insulin injection. The insulin dose is not fixed and can vary depending on factors such as level of physical activities, meal size, type of meal and the actual glucose level [6]. Therefore, patients are required to regularly measure their blood glucose levels in a day. Continuous glucose measurement and control can greatly reduce mortality and other medical complications in diabetics [7], [8].

1.2 Glucose

1.2.1 Structure

Glucose is the central carbohydrate of human physiology with the chemical formula $C_6H_{12}O_6$ and molecular weight of 180.156 g/mol. It has two optical isomers: D- and L- glucose [9]. D-glucose is naturally occurring and involved in human metabolism while L-glucose is synthetically manufactured

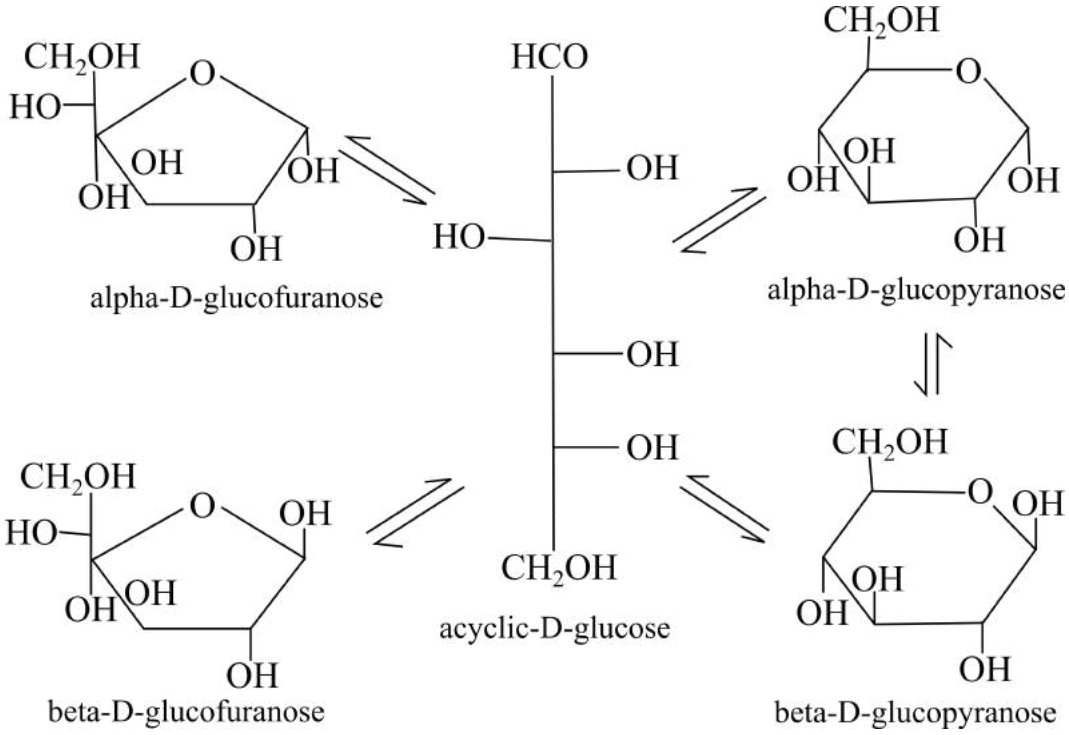

FIGURE 1.1: Anomers of D-glucose in aqueous solution [11]

and cannot be used by human cells. In this article, glucose refers to the D-isoform. Glucose is hydrophobic and in an aqueous solution, exists in five anomeric forms as seen in Figure 1.1.

Glucose is the most important form of energy in the human body and is stored as glycogen. When the body needs energy, glycogen stores are broken down into glucose through a process called glycogenolysis and transported throughout the body via blood. Apart from blood, glucose is present in other biofluids such as intracellular fluid, interstitial fluid, urine, sweat, aqueous humour and saliva [10].

1.2.2 Invasive measurement

The common method for monitoring the blood glucose level involves pricking the patient's fingertip with a lancing device to extract a drop of blood. The blood is placed on an enzymatic test strip and analyzed using an electrochemical reaction. The glucose in the blood is initially oxidized using the enzyme glucose oxidase in the presence of water and oxygen. The enzyme is specific to glucose and its mainly used to determine glucose in body fluids [12], [13] by converting it to hydrogen peroxide and gluconic acid.

$$\text{Glucose} + H_2O + O_2 \xrightarrow{\text{glucose oxidase}} \text{Gluconic acid} + H_2O_2$$

The glucose concentration is then determined using electro-chemical methods such as amperometry or potentiometry. The concentration is directly proportional to the amount of consumed oxygen and concentration of gluconic acid or hydrogen peroxide produced [10]. During amperometric measurements for example, hydrogen peroxide is oxidized at the anode of an electro-chemical probe to produce an amperometric signal (current) that is proportional to the glucose concentration [14]. This finger pricking method is the most accurate method for glucose measurements due to its high sensitivity and reliability [15].

Patients are recommended by doctors to measure their glucose levels several times a day which makes finger pricking method relatively painful, uncomfortable and it poses the risk of developing an infection at the site where the skin is pricked. As a result, diabetics are unwilling to check their glucose levels regularly as recommended by doctors [16]. There is a need for the development of a reliable, painless and non-invasive method for measuring the glucose levels.

1.3 Non-invasive glucose measurement

A lot of effort has been devoted to developing an alternative method for measuring glucose non-invasively. It would improve the quality of life of diabetics and improve their compliance to frequently monitor their blood glucose levels. For a method to be adopted into a glucose measuring sensor, the following requirements need to be fulfilled:

- Stability. This refers to how a measurement device performs over a long period of time. A device should have high precision such that measurements are reproducible for the same concentration. In addition, it should provide high degree of accuracy such that measurements do vary over time.
- Sensitivity. It refers to the smallest concentration that a sensor can detect. A blood glucose sensor should be able to detect glucose concentrations as low as 30 mg/dL [17].
- Selectivity. The measurement method should be able to discriminate the glucose signal from signals from other substances. Glucose in the human body is found in aqueous solutions that contains ions or proteins which may produce a signal that interferes with the glucose measurements.
- Portability. The measurement device should be small and easy to carry.

Due to the challenge of directly accessing blood for non-invasive glucose measurement, biofluids that are easily accessible such as urine [18], saliva

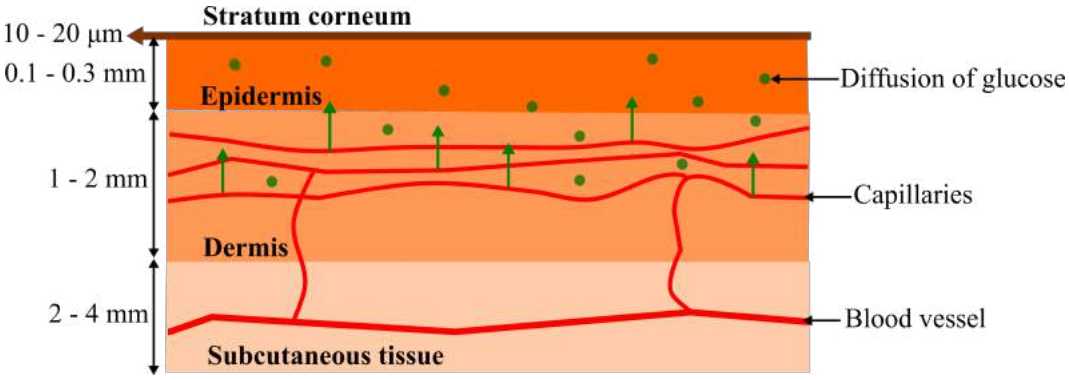

FIGURE 1.2: Schematic of the human skin [25].

[19], tears [20], [21] and sweat [22] have been investigated as alternatives to measuring glucose in blood. However, the glucose levels in these fluids have poor correlation with the blood glucose levels [23] and long lag time [24] making them unsuitable. Glucose measurements of saliva are affected by changes of the pH value that can occur after eating acidic foods.

A suitable alternative to measuring glucose concentration directly from blood vessels is by probing the interstitial fluid (ISF) in the epidermal layer of the human skin. A cross-section of the human skin is presented in Figure 1.2 which consists of the stratum corneum, epidermis, dermis and subcutaneous tissue. The epidermis layer is a few micrometers under the outermost skin layer the stratum corneum. The layer has no blood vessels and the cells are nourised by the interstitial fluid. Blood capillaries are found deeper in the dermis layer which is approximately a few millimeters deep.

The intersitial fluid is an extracellular fluid that diffuses through blood capillaries. Probing ISF for glucose is advantageous as it contains fewer proteins in its matrix compared to blood since some of the blood proteins cannot diffuse across the blood capillaries. The glucose concentration in ISF is similar with blood glucose [26] and follows blood glucose variations with a delay of approximately 5 minutes to 15 minutes depending on the skin location probed [24], [27], [28]. The ISF is located about 15 µm to 20 µm under the stratum corneum layer.

Non-invasive methods are broadly classified as either optical or non-optical methods.

1.3.1 Non-optical methods

Non-optical methods include reverse iontophoresis, ultrasound (sonophoresis), bioimpedance spectroscopy, electromagnetic and metabolic heat confirmation.

Reverse iontophoresis [29] is a process where a weak electric current is transported between the cathode and anode placed on the skin surface. The current causes ions in the interstitial fluid to move to the skin surface by electro-osmotic flow carrying with it glucose molecules [14]. The glucose concentration in the fluid is determined by the enzymatic method using glucose oxidase. The movement of the interstitial fluid to the skin surface is slow and as a result, the measurements have around 20 minutes lag to blood glucose reading [10]. The accuracy of the method is considerably affected by sweat and the flow of electric current causes skin irritation.

Sonophoresis (ultrasound) [30], [31] like reverse iontophoresis is based on extraction of the interstitial fluid at the skin surface then measuring the glucose concentration using the enzymatic method. The method employs piezoelectric transducers to generate low frequency ultrasound that increases the skin's permeability to the interstitial fluid through a process referred to as skin cavitation. The technique is commonly used to transport drugs into the body and has no adverse effects on the skin. However, it is susceptible to temperature fluctuations and pressure changes [14].

Bioimpedance spectroscopy [32] measures changes in tissue impedance levels using an electric current. Changes in blood glucose levels, changes the osmolarity of the blood serum. This causes the redistribution of potassium and sodium ions in the surrounding tissue and blood that changes the permittivity and conductivity of tissue that can be correlated to the blood glucose levels [14], [15]. The method is relatively simple and potentially affordable to implement into a portable glucose measuring sensor. However, human tissue morphology is different from one individual to another which causes different tissue impedance between individuals that is not related to glucose variations. The technique is susceptible to motion artifacts, sweating and tissue temperature changes that affects tissue impedance [15].

Metabolic heat conformation method measures the heat generated from glucose oxidation, the blood flow rate and blood oxygen levels at the fingertip [14]. Statistical methods are then used to extract the glucose concentration from the measurements. The method is susceptible to environmental conditions such as temperature [33] and thus used to provide auxiliary data for glucose quantification [34].

1.3.2 Optical methods

Optical methods utilize laser radiation to probe glucose molecules within the human body. Glucose concentration is then correlated to a change in either the light's intensity, polarization or wavelength after interacting with glucose molecules. Optical methods are highly selective even in complex matrix like blood, quick and the radiation is not harmful to the human body

as the intensity used obeys laser protection guidelines and is non-ionizing making them suitable for in vivo glucose measurements.

Initially, most of the methods have been investigated in the near-infrared (NIR) region [35]–[38]. This is due to the optical or therapeutic window where light absorption by water is low and hence the radiation can penetrate several millimeters deep into the human tissue and reach the blood vessels for glucose measurements [39], [40]. NIR measurements probe harmonic overtones of glucose vibrations [41] and, as a result, the glucose absorption is relatively weak compared to the background water absorption. The accuracy of the measurements is limited by strong interference from tissue and other blood components with similar absorption spectra [6], [35], [36], [38]. Furthermore, NIR measurements are affected by strong tissue scattering compared to mid-infrared light.

Mid-infrared radiation (MIR) has penetration depth of around 100 µm in tissue due to strong attenuation by water. As a result, MIR measurements probe ISF for glucose measurements. Glucose has isolated absorption bands in the MIR due to fundamental vibrational modes between 1000 cm^{-1} to 1245 cm^{-1} which improves the selectivity of glucose from other components of the ISF and enables easy quantification of glucose concentration [24]. MIR glucose absorption is strong which improves the sensitivity of measurements to small glucose concentration. Furthermore, MIR radiation is less scattered in tissue compared to NIR radiation hence more photons can be detected.

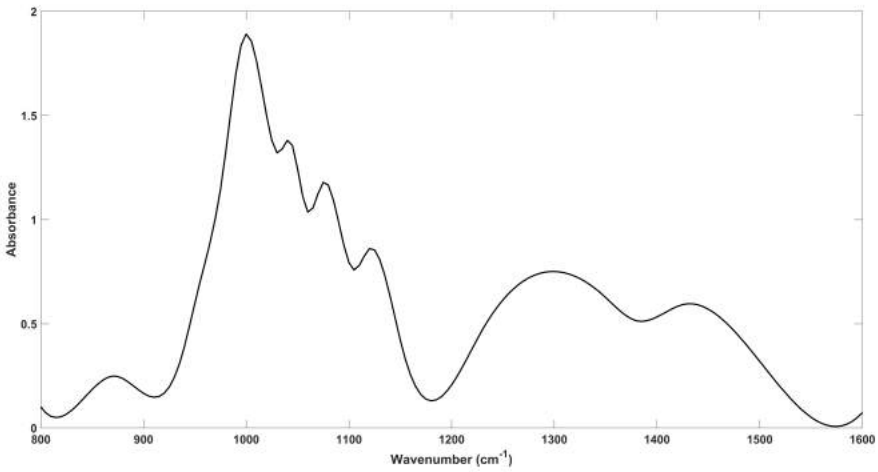

FIGURE 1.3: Absorption spectrum for aqueous glucose in the MIR region extending from 800 cm^{-1} to 1600 cm^{-1} (wavelength of 6.25 mm to 11 mm) [41].

The absorption spectra of aqueous glucose is shown in Figure 1.3. Water absorption has been subtracted from the spectra. The absorption bands between represents the glucose fingerprint region are attributed to fundamental stretching and bending modes of glucose [11], [42].

Figure 1.3 shows the absorption spectra of aqueous glucose in the MIR region. Water absorption has been subtracted from the spectra. Glucose absorption peaks are identified at around 920 cm^{-1}, 1037 cm^{-1}, 1060 cm^{-1}, 1085 cm^{-1}, 1109 cm^{-1}, 1150 cm^{-1}, 1365 cm^{-1} and 1435 cm^{-1} [24], [41]. The region with the strongest glucose absorption between 900 cm^{-1} and 1200 cm^{-1} is the glucose fingerprint region. The peaks are attributed to stretching and bending modes of C – O – H [11], [24].

Various optical spectroscopic techniques have been explored in the search for a non-invasive blood glucose measurement. Among them is Raman spectroscopy [43]–[46] which monitors inelastically scattered light to determine the vibrational spectrum of glucose with the intensity of the Raman shifted light related to the glucose levels. Raman spectra compared to infrared spectra, have less overtones and spectra overlap. As a result, glucose has narrow bands which enable spectral selectivity against blood and tissue components [23], [47]. Furthermore, water has a small Raman scattering cross-section which fosters glucose detection is aqueous media. However, Raman signal is weak due to the low excitation efficiency of Raman scattering. Thus Raman measurements require long integration time to improve the signal to noise ratio of the measurements. The measurements are also greatly affected by tissue autofluorescence which produce a fluorescence signal that is larger than or equal to the Raman signal.

Polarimetry [48]–[50] is a technique which correlates the glucose levels with the degree of rotation of linearly polarised light by aqueous glucose molecules. Polarimetric measurements in and through the skin are not effective because the skin is a highly scattering tissue and will depolarise the light. The ideal measurement location is through the eye where light scattering is minimum to measure glucose in the aqueous humour. Polarimetric measurement of aqueous humour has a lag time of around 30 minutes [48] which is not ideal for continuous glucose monitoring. The degree of rotation of the polarised light is affected by temperature and presence of albumin and ascorbic acid which are optically active materials [51].

Diffuse reflectance spectroscopy [52], [53] takes advantage of the strong scattering properties of the skin. A light beam is focused on a small area of the skin, the reflected light intensity is detected and used to determine the absorption co-efficient μ_a and reduced scattering co-efficient μ_s' of the skin. Glucose levels are correlated to the changes in the reduced scattering coefficient of the skin [54], [55]. The reduced scattering coefficient depends on the difference in the refractive index between extracellular fluids (such as ISF) and tissue scatters (cell membrane and cellular components) [56]. However, changes in osmolytes (urea, NaCl and KCl ions) have been shown to significantly change the reduced scattering coefficient [57] and hence affect the accuracy of the measurements.

Optical coherence tomography (OCT) [58], [59] uses an interferometer to

combine back scattered radiation from the skin with radiation from a reference arm to produce an interferometric signal. Glucose concentration is correlated with the scattering coefficient μ_s that is calculated from the interferometric signal. The OCT signal can be measured at a specific tissue layer depth whereas diffuse reflectance spectroscopy integrates the signal over the entire photon path which can consist of numerous layers [14], [15]. As a result, OCT can significantly reduce the interference signal from other scattering effects within the tissue and hence provide higher accuracy. The accuracy of OCT is susceptible to patient motion, changes in tissue temperature and osmolytes [15].

Photoacoustic spectroscopy (PAS) [60]–[62] unlike the other optical methods, detects acoustic waves produced from optical excitation. The amplitude of the photoacoustic signal correlates with the glucose levels. Photoacoustic (PA) measurements provide high sensitivity since acoustic waves are more immune to tissue scattering than photons and unlike conventional absorption spectroscopy, scattered light doesn't contribute to the signal. PA glucose measurements have been shown to provide good selectivity and stability, however, the technique does not provide enough sensitivity.

1.4 Thesis aim and structure

Despite all the numerous attempts, a non-invasive glucose measurement method is presently not available to diabetic patients. This project work contributes to the development of a photoacoustic sensor by improving the sensitivity of PA measurements. Photoacoustic glucose measurements utilize an open T-shaped resonator for signal amplification. In this work, a numerical shape optimization of the open T-shaped resonator is performed for maximum PA signal and hence improved sensitivity. This requires numerical models that can accurately simulate the photoacoustic signal.

The project work can be broadly split into three steps.

- In the first step, PA simulation models using the viscothermal (VT) and amplitude mode expansion model (AME) are developed for solid samples. Their performance in accurately modelling the PA signal in a closed macroscopic T-shaped resonator is analyzed and validate using experimental measurements.
- In the second step, the VT and AME models are adopted for the simulation of an open resonator configuration using perfectly matched layers (PML) and boundary element method (BEM). Three approaches for simulating an open resonator are presented, that is, the viscothermal model with perfectly matched layers (VT-PML), viscothermal with

boundary element method (VT-BEM) and the amplitude mode expansion model with perfectly matched layers (AME-PML).

- In the final step, the most suitable simulation approach is implemented in a shape optimization of the open T-shaped resonator with the aim of maximizing the photoacoustic signal. The optimization finds the best the resonator radii and lengths that will result in the greatest signal amplification.

In Chapter 2, the photoacoustic process is described. The most important components of a typical photoacoustic set up are explained. Then the state of the art of photoacoustic glucose measurements is reviewed. In Chapter 3, PA the simulation models are described for both the open and closed resonator configuration. The implementation of the models in a T-shaped resonator is described for both the configurations. In Chapter 4 the experimental set up used to validate the simulation results is described. The simulation results of the open and closed resonator along with experimental measurements are presented. In Chapter 5, the optimization procedure is presented along with the results from the optimization process. The report is concluded in Chapter 6 where the contributions from this work are highlighted along with suggestion for future investigations that would help realize the development of a photoacoustic sensor for non-invasive measurement of blood glucose.

Chapter 2

Photoacoustic spectroscopy

2.1 Fundamentals

Photoacoustic spectroscopy (PAS) is based on the photoacoustic effect that was discovered by Alexander Bell in 1880 when he realized that thin discs produce sound when illuminated with rapidly interrupted sunlight [63]. The photoacoustic effect was later detected in liquids by Preece [64] and in gases by Tyndall [65] and Röntgen [66]. The applicability of the effect was initially limited but the development of laser technology and pressure detection devices resulted in increased interest. PAS using lasers was first demonstrated by Kerr and Atwood to detect carbon dioxide using a continuous wave CO_2 laser in 1968 [67].

PAS is a special variation of absorption spectroscopy where acoustic waves are detected instead of photons. When molecules absorb photons, they are excited to higher energy levels. The molecules can decay back to the ground state either radiatively by releasing a photon (for example fluorescence) or non-radiatively by collisional relaxation, where the absorbed photon energy is transformed into translation energy. When the radiative lifetime of the molecules is longer than non-radiative lifetime, collisional relaxation dominates. This is usually the case for vibrational excitation at wavelength of above 10 µm where the radiative decay has characteristic lifetime of 10^{-2} s while non-radiative lifetime is typically 10^{-3} s at atmospheric pressure [68]. Non-radiative lifetime is pressure dependent and can vary between 10^{-3} to 10^{-8} s. During collisional relaxation, the absorbed photon energy is released as heat causing temperature increment of the surrounding. When the radiation source is modulated, photon absorption and subsequent heat release to the surrounding is periodic, thus generating a pressure wave. It is this pressure wave that is detected and referred to as the photoacoustic signal.

Photoacoustic spectroscopy has been widely demonstrated in trace gas detection [69], [70], medical application [71]–[73], condensed matter analysis [74], [75] and food industry [76]. PAS has numerous advantages over other spectroscopic methods:

- Compared to conventional absorption spectroscopy it provides higher sensitivity. This is because PAS measures energy absorbed by the sample instead of decrease in the light intensity after being transmitted through the sample [77]–[79]. The PA signal is not produced when an absorbing sample is not present unlike in conventional absorption spectroscopy where the transmitted signal can be affected by light scattering or reflection.
- Unlike absorption spectroscopy, PAS does not require long interaction path between the sample and the excitation light source.
- PAS can measure concentrations as low as parts per trillion [80], [81].
- The method is relatively cheap since the measurement equipment such as microphones are not expensive compared to infrared optical detectors [80].
- Possible to reduce the system size into a portable measurement instrument [70], [82].
- The method can be used to detect optically opaque samples unlike traditional absorption spectroscopy [77], [79].
- It is a nondestructive method for sample evaluation with little to no sample preparation required. The probe remains unchanged after measurement and can be re-used [82], [83].
- The method is capable of detecting multiple species [70], [84].

A typical photoacoustic set up consists of an optical excitation source, an acoustic resonator and an acoustic detection system as shown in Figure 2.1.

FIGURE 2.1: Schematic of a typical photoacoustic setup.

2.1.1 Optical source

Molecular energy is quantized into electronic, vibrational and rotational energy levels that uniquely characterise each molecule. This property is utilised in optical spectroscopy to identify and quantify molecules. Molecules in the ground state, the lowest energy level, can be excited to a higher energy level by absorbing photons. The absorption of photons by a molecule occurs if the photon energy E_{photon} corresponds to the difference of two energy levels of the molecule ΔE.

$$\Delta E = E_2 - E_1. \tag{2.1}$$

The photon energy E_{photon} is related to its wavelength λ using

$$E_{photon} = hv = hc/\lambda \tag{2.2}$$

where h is Plank's constant, v the frequency of the photons and c the speed of light. The molecular transitions are related to the wavelength (thus energy) of the photons. The transition between ground state to an excited electronic state requires photons with wavelengths in the visible and ultraviolet region. Photons in the infrared spectral range cause vibrational transition while microwaves are responsible for rotational transitions.

Since the excited states are unstable, molecules eventually return to the stable ground state through several different paths as illustrated in Figure 2.2.

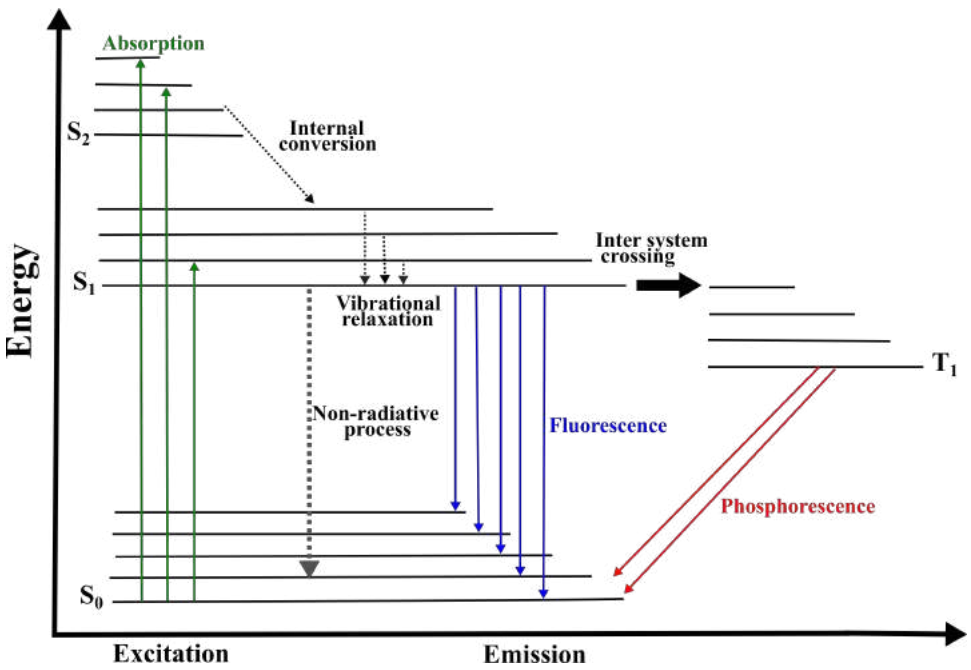

FIGURE 2.2: The Jablonski diagram showing the different molecular transitions [85]

The energy levels labelled S_0, S_1, S_2 are the electronic energy levels for which the sum of the electron spin quantum number is zero (singlet state) while T_1 is a triplet state for which the spin of an electron has changed sign. The molecular decay from an excited state can occur through:

- Radiative decay by luminescence. When the photon emitted occurs between an excited state and a ground state with the same spin, the radiation is called fluorescence. The molecules in the excited state can transition to a triplet state before decaying to the ground state, the emission is called phosphorescence. Fluorescence emission has a characteristic lifetime of nanoseconds and the emission has shorter wavelength compared to phosphorescence.
- Non-radiative decay by inter system crossing. Inter system crossing occurs when the spin state changes from a singlet to a triplet. The transition is quantum mechanically forbidden and occurs at a typical time scale of 10^{-8} s.
- Non-radiative decay by internal conversion and vibrational relation. When a molecule is excited to a higher energy level, it decays rapidly to the lowest vibrational state of the excited energy level S_1. The decay is very rapid in the time scale of picoseconds.
- Non-radiative decay due to collision of molecules a process referred to as quenching.

Photoacoustic effect is produced by non-radiative relaxation of molecules. The molecular excitation for the photoacoustic process can be achieved using light sources with emission ranging from the ultraviolet region to the far infrared. However, in the ultraviolet and visible spectral range, the radiative lifetime of molecules is shorter than non-radiative lifetime and hence fluorescence de-excitation dominates. In the infrared region, non-radiative lifetime is typically shorter than the radiative lifetime hence PA measurements are mainly performed in the infrared range

Broadband infrared lamps were initially employed for PA excitation as they are cost effective and provide wide spectral coverage [68]. Infrared lamps have been used for PA absorption spectra of trace gas elements with sensitivity to parts per million level [86].

The invention of lasers in 1960 increased interest in PA measurements due to the inherent properties of laser light that makes them suitable for spectroscopic applications. The intensity of laser radiation is orders of magnitude higher than conventional light sources which improves the sensitivity of measurements. The light has spectral line widths that are narrower than molecular absorption line widths [80] which enables selective excitation of specific molecules in a complex mixture. Additionally, laser light has good spatial coherence thus provides good spatial resolution of measurement sample and allows for remote/ non-invasive measurement. Lasers are tunable over a wide spectral range that allows the excitation of numerous atomic or molecular transition.

Both, pulsed and continuous wave (CW) laser sources are used for PA application. For a CW laser source, the laser intensity is modulated at a duty

cycle of 50 %. This is mostly achieved using a mechanical chopper [68], [77], [87], [88] that periodically blocks the laser beam using a rotating chopper disc that is driven using a motor. A mechanical chopper has several disadvantages. The mechanical system generates coherent noise to the modulated photoacoustic signal. Separating the chopper noise from the PA signal is difficult which decreases the signal to noise ratio of the measurements. Mechanical systems are liable to wear and imperfection in the mechanical design may alter the chopper modulation frequency.

Alternatives to the mechanical chopper are an electro-optical [89], [90] or acousto-optical modulation. The modulation is based on the principal of interference where the laser beam is split into two paths. One of the paths contains a non-linear optical material that causes a delay. The beams from the two paths are then recombined resulting in either constructive or destructive interference depending on the relative phase shift caused by the delay. In cases where diode lasers are used, the modulation can be achieved by directly modulating the laser driving current [91].

The PA signal based on modulated excitation of solid samples is described by Rosencwaig and Gersho who describe six different cases [92] depending on the thermal and optical properties of the sample with respect to its length. For glucose measurements across the skin, the PA signal amplitude S is dependent on the modulation frequency as [87], [93]

$$S_{PA} \propto \frac{\alpha(\lambda) I_0(\lambda)}{V f^{1.5}} \tag{2.3}$$

where $\alpha(\lambda), I_0(\lambda), V, f, L, \mu_a, \mu_s, \lambda$ represent the absorption coefficient, the incident laser intensity, the enclosed gas volume (within the acoustic resonator), the modulation frequency, the sample thickness, the optical penetration depth, the thermal diffusion length and the excitation wavelength respectively. Since the amplitude of the PA signal is inversely proportional to the modulation frequency, the laser intensity is modulated at audio frequencies of less than 10 kHz. However, electronic and external acoustic noise increase with decreasing frequency. As a result, the measurements from CW excitation usually have a low signal to noise ratio. The generated PA signal has the same frequency as the laser modulation frequency.

Pulsed lasers generate a heat pulse within the measured sample which excites an acoustic pulse [94]. This requires a short laser pulse such that thermal and stress confinement conditions are fulfilled [95], [96]. Thermal confinement indicates that thermal diffusion during laser illumination can be neglected while the stress confinement indicates that volume expansion of the sample during the illumination period can be neglected. Lasers with pulse duration in the nanosecond range fulfill this requirement

$$\tau < \tau_{st} = \frac{d_c}{v_s} < \tau_{th} = \frac{d_c^2}{D_t} \tag{2.4}$$

where $\tau, \tau_{st}, \tau th, d_c, v_s, D_t$ are the laser pulse duration, stress confinement threshold, thermal confinement threshold, the characteristic length of heat heterogeneity, speed of sound and thermal diffusivity respectively. The fractional volume expansion dV/V of a sample at a position $\mathbf{r}$ after pulse excitation is given by

$$\frac{dV}{V} = -kp(\mathbf{r}) + \beta T(\mathbf{r}) \tag{2.5}$$

where $k, p(\mathbf{r}), \beta, T(\mathbf{r})$ are the isothermal compressibility, change in pressure, thermal coefficient of volume expansion and change in temperature respectively. The local pressure increment from the short pulse can be expressed as

$$p(\mathbf{r}) = \frac{\beta T(\mathbf{r})}{k}. \tag{2.6}$$

Assuming that all the absorbed optical energy from the pulse is converted into heat, the temperature change is given by

$$T = \frac{A}{\rho C_v}, \tag{2.7}$$

where ρ, C_v, A are the density, heat capacity at constant volume and the absorbed optical energy deposition density respectively. A is the product of the absorption coefficient and local light fluence (energy of the laser pulse per illumination area). Substituting T in Equation 2.6 with Equation 2.7, we get:

$$P = \frac{\beta A}{k\rho C_v}. \tag{2.8}$$

Pulsed excitation generates a broadband PA signal that is frequency independent. As a result, measurements can be made at higher frequencies and hence low frequency noise components can be separated from the signal thus increasing the overall signal to noise ratio.

In the MIR range, glucose vibrational modes can be accessed using tunable CO_2 laser [97], [98], optical parametric oscillators [99], lead salt lasers or quantum cascade lasers. Lead salt lasers produce MIR wavelengths between 3 µm to 30 µm that is dependent on the energy band gap of IV-VI

semiconductor materials. However, they require cryogenic cooling due to the poor thermal conductivity of the semiconductor material and have low output power of around 0.1 mW to 0.5 mW making them unsuitable for sensitive PA measurements [68], [100].

CO_2 lasers produce high optical power in kilowatts range and have a relatively compact design. The laser emission has a narrow line width and is tunable over a broad spectral range that covers the glucose fingerprint region [100]. However, continuous wavelength tuning, and power stability are difficult to achieve [80], [101].

Optical parametric oscillators (OPO) are broadly tunable but their operation is complex compared to pure laser system. OPO generate wavelengths by utilising the second order non-linear susceptability of crystals. The process requires the phase matching condition to be satisfied. Given that the refractive index of the non-linear crystal is temperature dependent, phase matching conditions are difficult to achieve to enable continuous wavelength tuning of the OPO. Therefore, they are are not widely used in spectroscopic measurements.

Recent development of quantum cascade lasers (QCL) has resulted in a lot of interest in MIR glucose measurements and is the most widely used light source for glucose measurements. QCL provide a tunable light source with high spectral density, long lifetime of more than 10000 hours, low energy consumption with long-term wavelength and power stability [102]. Furthermore, QCL can be miniaturized which makes them an idea light source for producing a portable device and have high output power that can penetrate deep into the skin to the access the interstitial fluid. In this work, a QCL is used and its operation principle is described in Chapter 4.

2.1.2 Acoustic resonator

Acoustic resonators are used to enhance the generated PA signal. By matching the modulation frequency of a CW laser or the pulse repetition rate for a pulsed laser excitation with the resonator's acoustic eigenfrequency, acoustic modes of a resonator can be excited.

Acoustic resonators play a crucial role is in improving the sensitivity of photoacoustic measurements. Resonance amplification of the PA signal up to 10000 [103] have been reported. Additionally, resonators can provide insulation from external acoustic noise. The degree of signal amplification by the resonator is given by the quality factor Q ,that describes the ratio of the stored acoustic energy to the total energy losses in the resonator.

$$Q = \frac{f_0}{\Delta f} \tag{2.9}$$

Here f_0 is the peak resonance frequency and Δf is the full width of the resonance profile at half maximum (FWHM). When the the laser modulation frequency slightly deviates from peak resonance frequency f_0, a steep drop of the amplification occurs especially for resonances with very high Q factor.

The peak resonance frequency depends on the speed of sound, which is affected by temperature [104], [105] and humidity [106] in the propagating media. Changes in temperature and humidity affect the speed of sound thus shifting the peak resonance frequency. It is recommended that resonators with high Q factor implement sensors to monitor the humidity and temperature fluctuations during measurements [107]. A control loop system can then be implemented to match the laser modulation frequency with the peak resonance frequency.

Losses within the resonator lowers its quality factor and thus the resonant acoustical amplification. The losses are broadly categorized into surface and volume effects. Surface losses occur from the interaction of the acoustic wave with the interior resonator surface and are the dominant dissipation mechanism in resonators. The main losses include viscous and thermal losses at the resonator surface, dissipation at the microphone diaphragm, compliance of the chamber walls and acoustic wave scattering losses at obstacles inside the resonator [68], [94]. Volumetric losses include radiation losses, as well as viscous and thermal losses in the bulk of the fluid. Radiation loss effects are negligible in closed resonator since the acoustic waves are almost perfectly reflected by the resonator walls [94].

The simplest acoustic resonator is a cylindrical resonator. Its symmetry coincides well with the axis of the laser beam propagation along the cylinder axis and is the most frequently used resonator in PAS [94]. A cylindrical resonator has longitudinal, radial and azimuthal acoustic modes respectively (2.3).

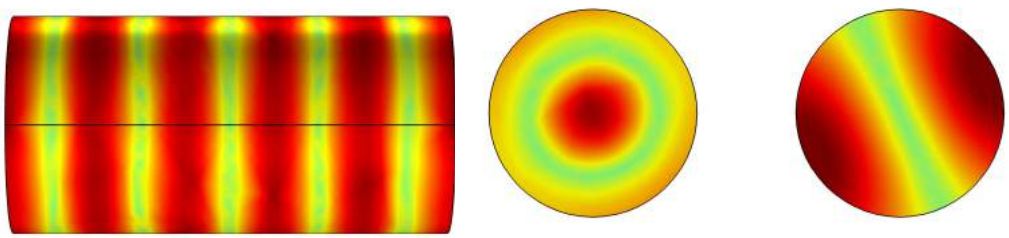

FIGURE 2.3: Longitudinal, radial and azimuthal modes of a cylindrical resonator respectively.

Depending on the application, various resonator shapes have been used for PA measurements such as a Helmholtz [108], H-shaped [109], T-shaped [110] and 'banana'cell [111].

2.1.3 Acoustic detector

The detection of PA signal is done using either microphones, piezoelectric transducers or optical detectors. The detector choice depends on numerous factors such as sensitivity, bandwidth, frequency, response time and detector size. Microphones are mostly selected for PA measurements as they are readily available and offer high sensitivity over a wide frequency range. This allows for the laser modulation frequency to be freely chosen.

Condenser and electret microphones are the standard microphones used in PAS [77]. A condenser microphone consists of a fixed back plate and a movable membrane. When pressure waves hit the membrane, the distance between the fixed back plate and the membrane changes which in turn changes the capacitance of the plates proportionate to the pressure amplitude. An electret microphone has a similar working principle to a condenser microphone. The membrane is however made using an electret material.

The signal from the microphone is processed using a lock-in amplifier so as to reduce noise levels and convert the signal to a digital format for storage and data processing. The reference frequency for the lock-in-amplifier is obtained from the modulation source when using CW excitation or pulse repetition rate of a pulsed laser.

Micro-electro-mechanical systems (MEMS) microphones were developed in 2002. They use the same principle as the condenser and electret microphone. Pedersen et al. [112] first used MEMS microphone for PAS and resulted in a significant improvement in thethe system performance. The MEMS microphones are smaller, cheap and suitable for developing a portable device [112].

Piezo electric transducers are based on the piezo electric effect found in materials without an inversion symmetry. The coupling between the internal dielectric polarization and strain of these materials causes an electric charge to be produced when pressure is applied. The most common piezo-electric transducer used for PA detection is a quartz tuning fork. A PA signal is generated between the two prongs of the tuning fork which induces anti-symmetric vibrations on the prongs. The vibrations are transformed to an electrical signal due to the piezoelectric effect of the material that is proportional to the PA signal. Acoustic signals that are not produced between the prongs induces symmetric vibrations on the prongs which does not generate a current [113]. As a result, detection with a turning fork is less sensitive to external acoustic noise. Tuning forks have resonances with high Q factor in the ultrasound region that are exploited to significantly amplify the PA signal. This requires that the frequency of the PA signal generated matches the resonance frequency of the tuning fork. At normal pressure, the resonance of a quartz turning fork has a width of approximately 4 Hz. Only pressure within this narrow spectral band can induce efficient excitation of the

quartz turning forks [113] thus further improving their immunity against external acoustic noise. However, precise alignment of the laser beam between the arms of the tuning fork is required to efficiently couple the generated pressure waves into the tuning fork. PAS measurements using tuning forks are commonly referred to as quartz enhanced photoacoustic spectroscopy (QEPAS) and have been broadly applied for trace gas measurements.

Optical detectors are based on refractometry and interferometry [114]. Refractometry based detection uses a probe laser to measure changes in the refractive index of a medium caused by the interaction of the medium with PA waves. Interferometric based detection monitors changes in optical interference pattern caused by the PA waves. The PA waves trigger changes in the mean free path or the optical phase depending on the interferometric configuration used [114].

2.2 PA glucose measurement

Glucose measurements are currently done in the MIR region due to strong glucose absorption and less interference from absorption of other tissue components. A glucose sensor should ideally be able to measure between the critically high and the critically low glucose levels i.e. between 30 mg/dl and 500 mg/dl. In-vitro studies have demonstrated glucose detection limits as low as 13.8 mg/dl in blood [115] and 4 mg/dl in aqueous glucose solution [116]. However, converting these in-vitro results to in-vivo detection is difficult since they do not bear additional challenges such as skin effects, artefacts from patient movement or blood pulsation.

Lilienfeld-Toal et al. [17] demonstrated that in-vivo MIR PA measurement of glucose in a complex matrix like the human skin is possible. They recorded the PA signal from the forearm of a healthy person during an oral glucose test using two pulsed QCLs emitting radiation at 1080 cm^{-1} and 1066 cm^{-1} which coincides with the maximum and the minimum of a glucose vibrational mode. The ratio between the wavelengths is used to indicate the changes of glucose levels. Their results demonstrate qualitative correlation between the glucose levels in the interstitial fluid and blood.

Kottmann et al.[62], [117] used a CW tunable external cavity quantum cascade laser (EC-QCL) to measure glucose deep in epidermal skin samples which closely resembles in-vivo measurement conditions. Skin transpiration during measurements caused a buildup of humidity inside the PA cell which can affect the sensitivity of the measurements. They demonstrated that by ventilating the PA cell with nitrogen gas stable measurement conditions can be achieved. Their measurements yielded a detection limit of 100 mg/dl with a SNR of 1 and a signal integration time of 1 s [62]. This detection limit is not sensitive enough for the approach to be developed into a glucose sensor.

Since PA measurements using CW excitation are performed in the audio frequency range, they are affected by noise and require longer time for signal integration. This makes the method susceptible to changes in temperature, small movements and even pulsation during in-vivo measurements. When they evaluated the feasibility of the approach in-vivo on a human forearm, an additional periodic signal to the PA signal was detected. The periodic signal was attributed to blood pulsation and could be significantly reduced with a longer integration time of around 1 s [117].

The latest study from Kottmann et al. [25] was an in-vivo measurement on the forearm of a healthy volunteer under oral glucose tolerance test. Two QCLs at fixed wavelengths corresponding with maximum and minimum glucose absorbance were employed. They performed out of phase wavelength modulation measurements to compensate for long term drifts and hence greatly improve the measurement stability. However, they reported that the detection sensitivity was still unsatisfactory for the physiological range of glucose concentration.

Pleitez et al. [61] used a pulsed external cavity quantum cascade laser (EC-QCL) tunable across the infrared glucose fingerprint region between 1000 cm^{-1} and 1245 cm^{-1}, with a photoacoustic cell (T-shaped) designed for ultrasound operation, to quantitatively measure the glucose concentration. Acoustic noise was reduced during measurements by operating the laser at high repetition rates and detecting the PA signal in the ultrasound region. They measured glucose levels non-invasively on a healthy and diabetic volunteer who had undergone a series of oral glucose tolerance test. They quantitatively measured glucose levels from the PA signal between the range of 50 mg/dl to 300 mg/dl. Their results demonstrated that their technique is sensitive to continuously follow changes in glucose levels over time and highly selective as they could multivariate data analysis to discriminate glucose signal from other interstitial constituents.

In a further study, Pleitez et al. [110] improved the stability of their measurement set up by using the T-shaped resonator in an open configuration. They demonstrated that the open configuration reduced the influence of pressure and temperature changes along with the buildup of humidity inside the cell caused by skin transpiration. Furthermore, the high repetition rate of the laser enabled recording of an entire spectrum between1000 cm^{-1} and 1245 cm^{-1} in a few seconds with a signal to noise ratio of 27. As a result, they demonstrated that PA glucose measurement using pulsed tunable EC-QCL excitation combined with ultrasound detection using an open T-shaped resonator provides enough selectivity and stability to be adopted into a portable sensor. However, the sensitivity of the method for in-vivo continuous measurement needs to be improved.

The open end of the T-shaped resonator used by Pleitez et al. leads to a leakage of the PA signal and therefore lowers the overall sensitivity of the set up. A method to boost the PA signal involves synergetic resonance matching

of the PA cell with the microphone [118] that is demonstrated by Sim et al. Using analytical and numerical calculations, they optimized the geometry of the resonator by calculating the its acoustic eigenmodes. They matched one of the resonances of the resonator with that of their microphone and which improved the signal to noise ratio by a factor of 3.5. The investigation was limited to a few selected resonator dimensions and leaves room for further optimization.

Chapter 3

Numerical simulation of a PA resonator

3.1 Introduction

Numerical methods have become an integral part of scientific research work and product development due to their ability to predict the physical behavior of devices or give greater understanding of a phenomenon. The methods are suitable for research fields where experimental testing maybe too expensive, experiments are not possible as they are too dangerous and in situations where an analytical solution to an engineering problem is impossible. Numerical methods have been boosted by the development of computers with excellent processing speed that has made calculations quicker and a cost-effective alternative to experimental prototyping. As a result, they have become a valuable tool for scientists and engineers.

The generation and propagation of acoustic waves is described using the fundamental equations of thermodynamics [119]. The equations express the motion of the fluid motion such as non-linearity and damping from viscosity and thermal loss. The acoustic waves generated during PAS are small perturbations of the equilibrium field, therefore, non-linear acoustic effects are neglected in the formalism since linear terms provide good approximation of the PA signal [120]. The linearized form of these governing equations, commonly referred to as linerized Navier-Stokes equations, are the basis of the viscothermal model described in section 3.2.2. The equations can be further simplified and reduced to the acoustic wave equation by assuming that the propagating fluid is adiabatic and that viscosity is negligible [119].

$$\nabla^2 p(\mathbf{r}) + k^2(\mathbf{r}) = 0, \tag{3.1}$$

The term $p(\mathbf{r})$ is the acoustic pressure at position $\mathbf{r}$ and k the acoustic wave number. The equation accounts for the propagation of acoustic waves only.

Therefore, a heat source term is supplemented to account for the thermal de-excitation of molecules after laser absorption responsible for the generation of the photoacoustic signal.

$$\nabla^2 p(\mathbf{r},\omega) + k^2 p(\mathbf{r},\omega) = i\omega \frac{\gamma - 1}{c^2} \mathcal{H}(\mathbf{r},\omega) \tag{3.2}$$

Here ω, γ is the ratio of isobaric and isochoric heat capacity and c is the speed of sound. The right hand side of the equation describes the excitation source where $\mathcal{H}(\mathbf{r},\omega)$ is the Fourier transform of the power density. The electromagnetic radiation responsible for the excitation in PAS is related to the power density by $\mathcal{H}(\mathbf{r},\omega) = \alpha I(\mathbf{r},\omega)$ if the absorption of the radiation by the molecules is not saturated and the modulation frequency is much smaller than relaxation rate of the molecular transition [121]. Here I is the intensity of the electromagnetic radiation and α is the absorption coefficient of the sample.

Equation 3.2 is the basis of the amplitude mode expansion model which is described in section 3.2.1 and the transmission line model. The transmission line model is the electrical circuit analogy for the acoustic wave equation where the resonator is expressed as circuit elements such as resistance, reactance, inductance and suseptance with the heat source term represented by a voltage source [94], [109], [122]. It is the most common used PA model due to it's simplicity and has been demonstrated in the design of PA acoustic resonators [122], [123]. However, the model is 1 dimensional and cannot describe 3D effects such as sound radiation at the resonator ends [94]. In a cylindrical resonator of radius r, the model can only be used for frequencies below a cutoff frequency w_{cutoff} , which is defined as the lowest transversal resonance frequency of the resonator [94].

$$\frac{w_{\text{cutoff}}}{c} r = 1.84 \tag{3.3}$$

The value of 1.84 is defined over the root of the Bessel-function of the eigenmodes in a cylindrical volume.

The solution of Equation 3.2 is solved by eigenmode expansion [119]. For resonators with simple and specific shapes such as spheres, cylinders, cubes, and rectangular prisms, the eigenmodes and eigenfrequencies can be analytical solved [94]. In a cylindrical resonator as an example, the homogeneous Helmholtz equation is expressed in the cylindrical coordinates as

$$\left[\frac{1}{r}\frac{\partial}{\partial r}(r\frac{\partial}{\partial r}) + \frac{1}{r^2}\frac{\partial^2}{\partial \varphi^2} + \frac{\partial^2}{\partial z^2}\right] p(r,\varphi,z) + k^2 p(r,\varphi,z) = 0. \tag{3.4}$$

Using sound hard boundary conditions, the solution of Equation 3.4 for a cylindrical resonator with length L_c and radius R_c becomes

$$p_j(r,\varphi,z) = \mathcal{N}_j J_m\left(\frac{r\pi\alpha_{mn}}{R_c}\right)\cos(m\varphi)\cos\left(\frac{\pi l z}{L_c}\right) \tag{3.5}$$

$$f_j = \frac{\omega_j}{2\pi} = \frac{c}{2}\sqrt{\left(\frac{l}{L_c}\right)^2 + \left(\frac{\alpha_{mn}}{R_c}\right)^2} \tag{3.6}$$

Here j represents the complete set of the eigenvalues of the longitudinal l, azimuthal m, and radial n modes respectively. α_{mn} is the mth root of the derivative of the nth Bessel function of the first kind divided by π while $\mathcal{N}_j$ is a normalization constant [121]. For the fundamental longitudinal modes, α_{mn} becomes zero and Equation 3.6 simplifies to

$$f_{lmn} = f_{100} = \frac{cl}{2L_c} \tag{3.7}$$

with l = 1,2,3,4....For complex resonator shapes an analytical solution is not possible and finite element methods are employed as they can handle complex geometries [121], [124].

3.2 Finite element method

Finite element method is used to solve partial differential equations by splitting the modelling domain into smaller, non-overlapping sections called finite elements. The discretization of the domain is performed by the construction of a mesh. The finite elements are connected at the nodes and the response of the elements are assembled at the nodes to form systems of equations that express the response of the entire modelling domain. The discretization of the modelling domain makes finite element method a versatile tool as it can handle irregular and curved domain boundaries.

Finite element simulations of photoacoustic signal were first demonstrated by Baumann et al. [121], [125]. They modelled the PA signal using the AME model in a closed T-shaped with the laser beam propagating axially along the cylinder length like in a gas detection set up with modulation frequencies between 0 Hz to 3.5 kHz. They performed qualitative analysis that demonstrated good agreement with experimental measurements and concluded that the model enabled the calculation of the PA response for any given resonator geometry. Later, Parvitte et al. [124] demonstrated quantitative PA simulations using the AME model in a differential Helmholtz resonator for measuring the concentrations of ethylene in nitrogen gas. Their results show accurate accordance between the simulations and measurements at modulation frequencies of between 0 Hz to 600 Hz. Glière et al. [126] compared the performance of the AME model, the VT model and third approach

in a micro differential Helmholtz resonator for gas sensing application. They simulated the PA response of a single resonance at around 20 kHz and concluded that for micro-resonators, the VT model provides highest accuracy while the AME model tended to overestimate the resonance frequency and amplitude. However, the AME model could be used to obtain quick and approximate results.

Finite element modelling of open resonators, to the best of my knowledge, has only been demonstrated in a cylindrical resonator using the VT model with perfectly matched layers at modulation frequency of around 4.5 kHz [127]. The authors modelled a Gaussian heat source diagonally across the resonator to represent the absorption of the laser beam by the nitrogen dioxide molecules. The simulation results demonstrated good accordance between the simulations and the measurements.

In this work, finite element modelling of the photoacoustic signal was performed using the software COMSOL Multiphysics. The photoacoustic signal generated inside a T-shaped resonator is calculated using the amplitude mode expansion model (AME) and viscothermal model (VT). While the two models have been studied in gaseous samples, their application in solid samples is yet to demonstrated. Additionally, their studies have mostly been limited to the audio range with little investigation of their performance in the ultrasound range. In this work, the performance of the models is extended to solid samples and the ultrasound range.

3.2.1 Amplitude mode expansion model

The AME method calculates the acoustic pressure $p(\mathbf{r}, \omega)$ at the location of the microphone $\mathbf{r}$ by solving the inhomogeneous Helmholtz Equation 3.2. The solution of Equation 3.2 can be expressed as a superposition of the acoustical eigenmodes of the resonator

$$p(\mathbf{r}, \omega) = \sum_j A_j(\omega) P_j(\mathbf{r}). \tag{3.8}$$

The modes $p_j(\mathbf{r})$ and corresponding eigenfrequencies ω_j are obtained by solving the homogeneous Helmholtz Equation 3.1 assuming a sound hard boundary. The boundary condition implies that the resonator wall perfectly reflects the pressure waves and is described using

$$\frac{\partial p}{\partial n} = 0. \tag{3.9}$$

The modes have to be normalized according to

$$\int_{V_c} p_i^* p_j dV = V_c \delta_{ij} \tag{3.10}$$

where V_C denotes the resonator volume and p_i^* is the complex conjugate of p_i. The amplitudes $A_j(\omega)$ are obtained using

$$A_j(\omega) = i \frac{\mathcal{A}_j \omega}{\omega^2 - \omega_j^2 + i\omega\omega_j l_j}. \tag{3.11}$$

The term $\mathcal{A}_j$ represents the excitation of an amplitude and is given by

$$\mathcal{A}_j = \frac{\alpha(\gamma - 1)}{V_c} \int_{V_c} p_j^* I \mathrm{d}V. \tag{3.12}$$

The integrand in Equation 3.12 is the overlap which describes how effective the laser beam excites a mode. Consequently, the excitation laser beam can be aligned through a resonator such that some resonances are not excited.

The in homogeneous Helmholtz equation 3.2 does not contain terms that account for losses. Losses mechanism are introduced by use of loss factors l_j in Equation 3.11. There are numerous loss effects that attenuate the pressure wave inside the resonator [70], however, only the surface and volume losses due to viscosity and thermal conduction are considered. The propagation of the pressure wave in the fluid is considered to be adiabatic therefore thermal conductivity of the fluid is minimal. However, temperature differences in the bulk of the propagating fluid, result in heat exchange that dissipate the pressure waves and adjacent fluid layers move at different speed through the resonator causing viscous friction. These thermal and viscous losses are estimated using

$$l_j^v = \frac{\omega_j}{c}(l_n + (\gamma - 1)l_k), \tag{3.13}$$

where l_n and l_k are the characteristic viscous and thermal length scales respectively given by

$$l_n = \frac{4\eta}{3\rho c}, \tag{3.14}$$

$$l_k = \frac{k}{\rho c_p c}. \tag{3.15}$$

The resonator walls are made from a metallic material whose thermal conduction coefficient is much greater than that of the propagating fluid. This

results in heat exchange between the resonator wall and the fluid thus the propagation becomes isothermal near the walls. The temperature drop also changes the velocity of the fluid which in turn increases the viscous friction. The region where the transition from adiabatic to isothermal behaviour occurs is called the boundary layer and is given by

$$d_k = \sqrt{\frac{2k}{\rho c_p \omega}} \tag{3.16}$$

where d_k representing the thermal boundary layer. The viscous boundary layer d_n is estimated by

$$d_n = \sqrt{\frac{2\eta}{\rho\omega}}. \tag{3.17}$$

The viscous losses at the wall are calculated by

$$l_n^s = \frac{1}{2}\left(\frac{c}{\omega_j}\right)^2 \frac{d_n}{V_c}\int_{s_c} |\nabla_{\mathbf{t}} p_j|^2 \mathrm{d}S. \tag{3.18}$$

The term $\nabla_{\mathbf{t}}$ is the gradient of the pressure component that is tangential to the resonator wall. The thermal surface losses are estimated using

$$l_k^s = \frac{1}{2}(\gamma - 1)\frac{d_k}{V_\mathrm{c}}\int_{s_\mathrm{c}} |p_j|^2 \mathrm{d}S. \tag{3.19}$$

3.2.2 Viscothermal model

The model is based on fundamental equations of fluid mechanics, that is the equations for conservation of mass, momentum (Navier-Stokes equation) and energy to solve for acoustic perturbations in pressure, velocity, and temperature [120].

$$\frac{\partial \rho}{\partial t} + \rho(\nabla.\mathbf{u}) = 0, \tag{3.20}$$

$$\rho\frac{\partial u}{\partial t} = \nabla.(-p\mathbf{I} + \mu(\nabla\mathbf{u} + (\mathbf{u})^T + (\mu_B - \frac{2}{3}\mu)(\nabla.\mathbf{u})\mathbf{I})) \tag{3.21}$$

$$\rho C_p\frac{\partial T}{\partial t} - \alpha_p T\frac{\partial p}{\partial t} = -\nabla.(k\nabla T) + Q. \tag{3.22}$$

Here $\rho, \mathbf{u}, p, \mu, \mu_B, C_p, T$ and α_p are density, velocity, pressure, dynamic viscosity, bulk viscosity, specific heat at constant pressure, temperature and the coefficient of thermal expansion of the propagating fluid, respectively. The field Q describes the spatial distribution of the heat source. In Addition, an equation of state has to be introduced to relate the variations in pressure, temperature, and density.

$$\rho = \rho(p, T) \tag{3.23}$$

The model assumes that the generated acoustic waves are due to small harmonic perturbation about the steady background properties. Therefore, the dependent variables are expressed as:

$$\mathbf{u} = \mathbf{u}_0 + \mathbf{u}_1 e^{i\omega t}, \tag{3.24}$$

$$T = T_0 + T_1 e^{i\omega t}, \tag{3.25}$$

$$p = p_0 + p_1 e^{i\omega t}. \tag{3.26}$$

The background quantities are represented with the subscript 0 while the perturbations with subscript 1. The background fluid is assumed to be quiescent so that $\mathbf{u}_0 = 0$. Equations 3.24 - 3.26 are inserted into Equations 3.24 - 3.26 . Since the perturbations are small, higher order terms are ignored and only linear terms retained.

$$i\omega\rho + \rho_0(\nabla.\mathbf{u}) = 0, \tag{3.27}$$

$$i\omega\rho_0\mathbf{u} = \nabla.(-p\mathbf{I} + \mu(\nabla\mathbf{u} + (\mathbf{u})^T + (\mu_B - \frac{2}{3}\mu)(\nabla.\mathbf{u})\mathbf{I})), \tag{3.28}$$

$$i\omega\rho_0 C_p T - \alpha_p T_0 i\omega p = -\nabla.(k\nabla T) + Q, \tag{3.29}$$

$$\rho = \rho_0(\beta_T p - \alpha_p T). \tag{3.30}$$

3.3 Modelling of a closed resonator

The procedure for implementing the two models in a closed cell is described. The VT model is implemented using COMSOL Multiphysic's thermoviscous acoustic module while the AME model is implemented using a Matlab script. The script connects with the COMSOL server to use the pressure acoustic module to determine the resonator's eigenfrequency and eigen modes by solving Equation 3.1. Air is selected as the propagating fluid with a temperature of 20 °C, the static pressure of 1013 hPa and with the parameters shown in Table 3.1.

Density	1.2044 kg/m^3
Sound velocity	343.2 m/s
Viscocity	1.814×10^{-8} Pa s
Coefficient of heat conduction	2.58×10^{-5} W/m K
Specific heat capacity at constant volume	7.1816×10^{2} J/kg K
Specific heat capacity at constant pressure	1.0054×10^{3} J/kg K

TABLE 3.1: Air parameters at a temperature of 20 °C and a static pressure of 1013 hPa [128]

Blood glucose measurements are done are performed by placing the patients skin at the end of the absorption cylinder. Therefore, the a

A heat source term is defined to represent the thermal energy deposited on the sample resulting from laser absorption. The laser beam is only absorbed at the end of the resonator where the patient's skin will be in contact with the resonator during blood glucose measurements. Therefore, the term is described at the end of the absorption cylinder using a circular profile that is limited within the cross-sectional area of the absorption cylinder as illustrated in Figure 3.1. The laser beam is assumed to be propagating along the z-axis of the resonator and is axially symmetric. The heat source term is restricted using

$$1 * (r_{\perp} < r_{abs}) * (z > (l_{cavity} + l_{abs}) * 0.9) \tag{3.31}$$

where r_{abs}, l_{abs} and l_{cavity} are the radius of the absorption cylinder, length of the absorption cylinder and the length of the cavity cylinder respectively. The term $r_{\perp}$ is the perpendicular distance from the z-axis given using

$$r_{\perp} = \sqrt{x^2 + y^2}. \tag{3.32}$$

The heat source term is set to 1 for simplicity and small variations in the size of the heat source do not have significant effects on the simulations [129].

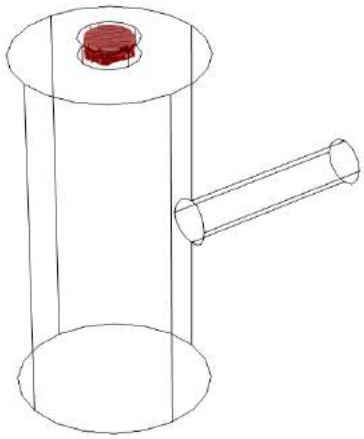

FIGURE 3.1: The position of the heat source term (red) within the resonator [91].

The walls of the PA cell are all set as sound hard (no slip and isothermal boundary conditions). The no-slip condition assumes that the fluid will have zero velocity relative to the boundary while the isothermal condition assumes that there are no temperature fluctuations at the boundary. This creates large thermal and viscous gradients at the walls of the resonator. Therefore, the walls of the resonator are lined with boundary layers to accurately capture thermal and viscous attenuation of the acoustic waves. The boundary layers are not required for accurate simulations with the AME model since losses are calculated using loss factors. The resonator is meshed using a swept mesh while sections where it could not be applied, a triangular mesh was used. The same mesh seen in Figure 3.2 was used for both the VT and AME models with the mesh properties presented in Table 3.2.

3.3.1 Convergence study

To check the quality of the generated mesh, a convergence study is performed with five different mesh sizes is conducted using the AME model. The accuracy of finite elements models improves as the mesh becomes refined. Starting with Mesh 0 (see Figure 3.3), the convergence study is performed by reducing the size of the mesh elements such that the degrees of freedom solved by the model increase by a factor of 2. However, when the number of mesh elements increase, the time required for the simulations increases as evident from Table 3.3. The convergence study of is only performed using the AME model.

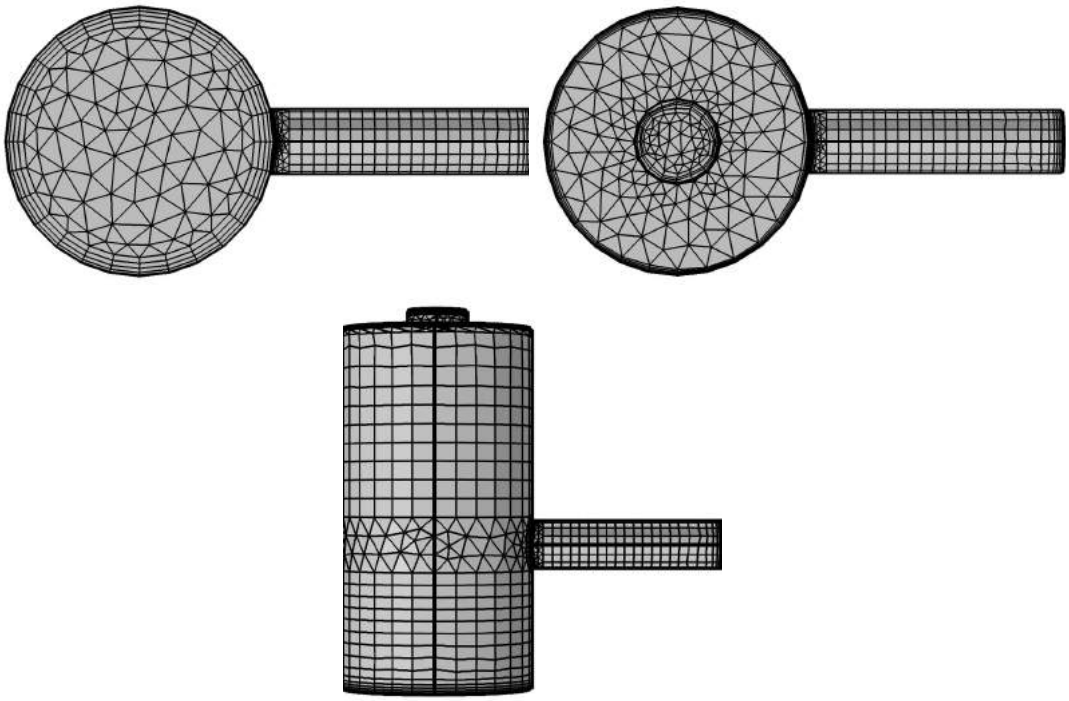

FIGURE 3.2: Top: Back and front view respectively of the mesh generated.Bottom: Side view of the mesh.

Mesh parameters	
Maximum element size (mm)	0.887
Minimum element size (mm)	0.0645
Maximum growth rate	1.4
Curvature factor	0.4
Resolution of narrow region	0.7
Number of boundary layers	4
Boundary layer stretching factor	1.2
Thickness adjustment factor	3
Number of elements	22451

TABLE 3.2: Parameters controlling the size of the mesh.

The plots indicate convergence since for different meshes similar spectral features are produced as seen in Figure 3.4.

	Mesh 0	Mesh 1	Mesh 2	Mesh 3	Mesh 4
Mesh elements	12354	22451	41409	79267	199264
DOF VT	266860	476980	875804	1804987	3722294
DOF AME	64589	115474	212041	437186	901678
AME solution time	5 min	7 min	11 min	24 min	52 min
VT solution time	-	1 week	-	-	-

TABLE 3.3: Properties and performance of the different mesh used for the convergence study.

3.4 Modelling of the open resonator

3.4.1 Perfectly matched layers

Perfectly matched layers (PML) is an artificial domain with anisotropic damping used to terminate unbounded domains. Waves incident on the PML are absorbed without reflections and attenuated by the PML domain. The approach was first introduced by Berengerin 1994 [130].

The radiating solution in infinite space is a superposition of plane waves. The solution can be decomposed into a function given by

$$\mathbf{u}(\omega, x) = e^{ikx} \tag{3.33}$$

where ω and k are the angular frequency and wave vector respectively. A wave propagating in the x-axis undergoes a complex coordinate transformation in the PML domain given by

$$\frac{d}{d\tilde{x}} \rightarrow \frac{d}{dx} = \frac{1}{1 + i\frac{\sigma_x(x)}{\omega}} \frac{d}{dx} \tag{3.34}$$

where $\sigma_x(x)$ is a function of x that represents the decay strength of the PML domain. In the PML domain, $\sigma_x > 0$ while in the simulation domain $\sigma_x = 0$ [131]. Applying the transformation to the wave e^{ikx}

$$e^{ik\tilde{x}} = e^{ikx} e^{-\frac{k}{\omega}\int^x \sigma_x(\acute{x})d\acute{x}} \tag{3.35}$$

The transformation introduces an exponentially decaying term in the solution. In the PML domain where $\sigma_x > 0$, the wave exponentially decays while in the modelling domain where $\sigma_x = 0$ it remains unchanged. The

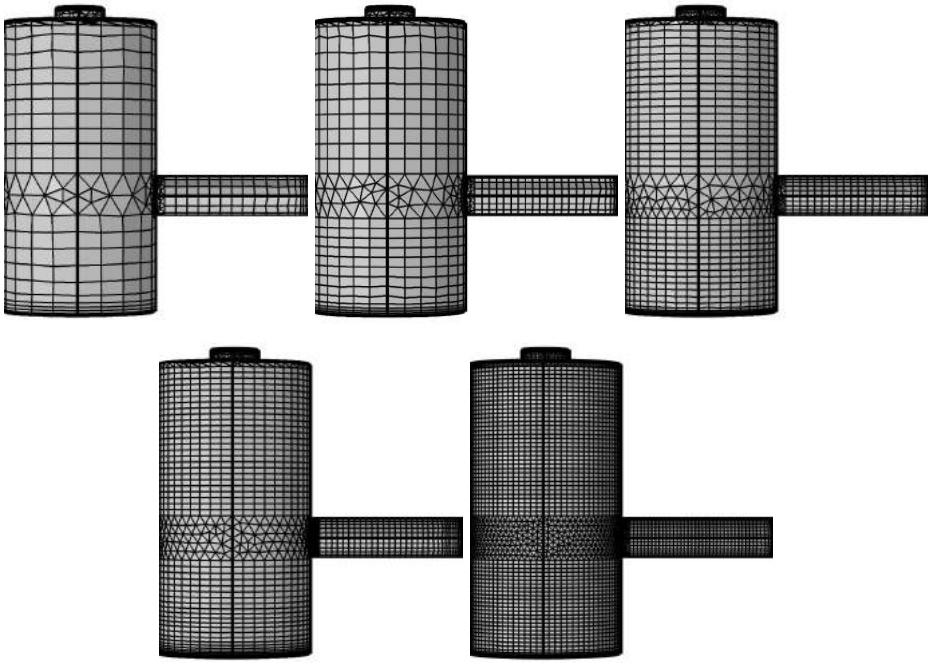

FIGURE 3.3: Top: Mesh O, Mesh 1 and Mesh 2 generated for the convergence study. Bottom: Mesh 4 and Mesh 5 generated for the convergence study.

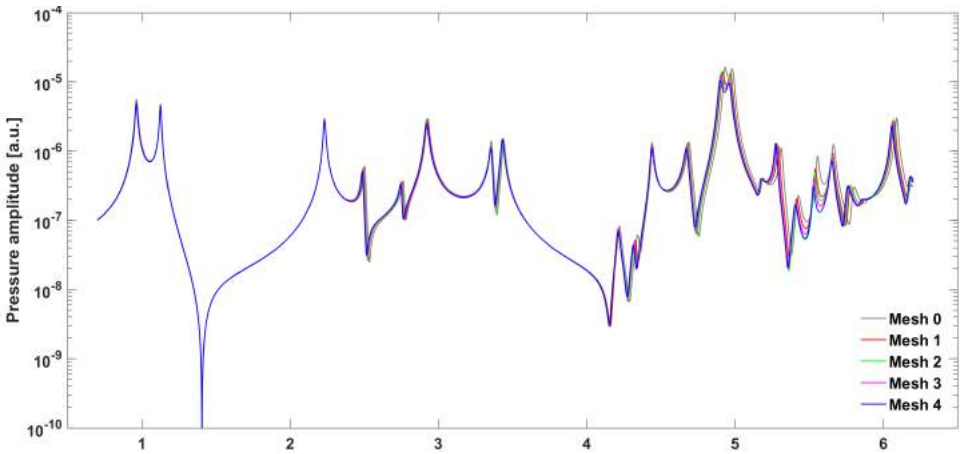

FIGURE 3.4: Frequency response plot of the AME model using the five meshes generated for the convergence study.

transformation is an analytical continuation of the original wave solution from x to $\tilde{x}$ where the solution does not change when $x = \tilde{x}$ [131]. As a result, the PML domain behaves like an absorbing medium with no reflections.

Waves decay quicker for higher values of σ_x. The PML does not generate any reflections when solving continuous wave equations. However, the discretisation of the equations generates some reflections. The reflections are reduced by gradually increasing the value of σ_x from zero on the PML interface.

The removal of the window at the cavity cylinder end opens the resonator to infinite free space. The free spac eis created using a hemisphere terminated with PML as seen in Figure 3.5. The PML extends the free space to infinity. The PML are used for both the viscothermal model (VT-PML) and the amplitude mode expansion model (AME-PML) to model the open resonator end.

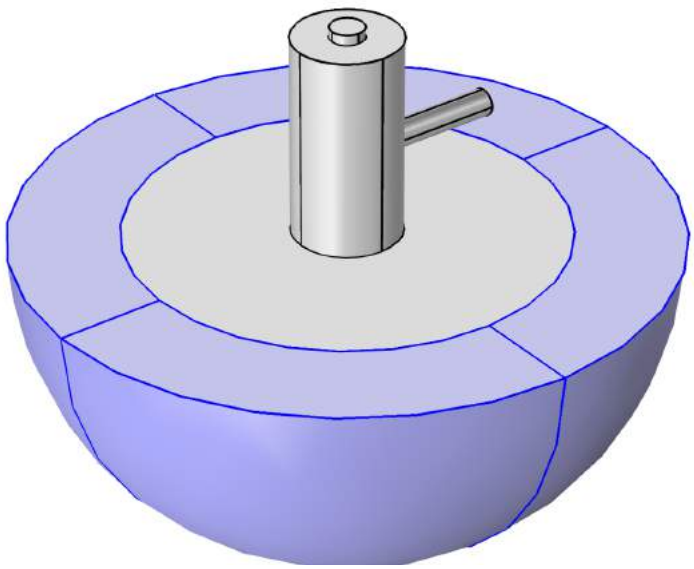

FIGURE 3.5: The resonator and the hemisphere representing the open end.Blue: The PML domain [132]

VT-PML

For the VT model, the resonator walls and flanged edge are set with no slip and isothermal boundary conditions. The hemisphere's radius is four times the radius of the opening while the thickness of the PML is twice the radius of the opening. The PML domain is meshed using a swept mesh while prism mesh element is selected for the flanged edge and resonator. The quality of the mesh generated is checked by generating an additional mesh with finer mesh elements to perform convergence study. The properties of the generated mesh pair and their properties are presented in Table 3.4. The simulations are performed ere performed between 10 kHz to 60 kHz with 50 Hz increment.

To check the quality of the PML, its thickness is varied by 10 % and investigated between 46 kHz and 51 kHz. Changing the PML thickness slightly affected the amplitude of the resonance, however, the peak resonance frequency was unaffected as seen in Figure 3.6. When the amplitude decreased, a peak-like feature between 48 kHz and 49 kHz became more prominent. The results with the larger hemisphere (which corresponds to larger air volume)

Mesh parameters	Fine mesh	Finest mesh
	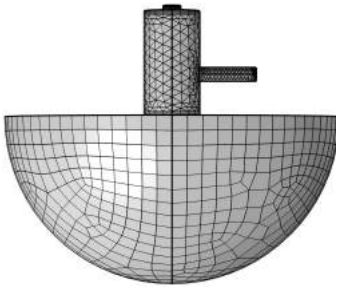	
Max. element size (mm)	1.429	1.2
Min. element size (mm)	0.481	0.481
Maximum growth rate	1.4	1.1
Curvature factor	0.4	0.4
Resolution of narrow region	0.7	0.7
Number of boundary layers	4	4
Boundary layer stretching factor	1.2	1.2
Thickness adjustment factor	3	3
DOF	654416	1176891

TABLE 3.4: Properties of the meshes generated for the VT-PML simulations [132]

resembles the measurement results more closely since the peak-like feature of the resonance between 48 kHz and 49 kHz is also not very prominent.

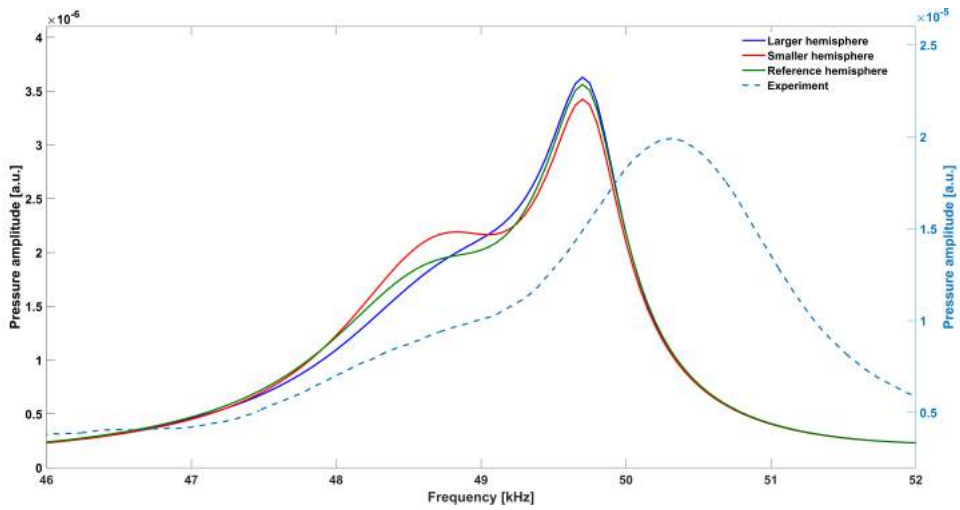

FIGURE 3.6: Frequency response of the VT model with different PML thickness against the experiment

AME-PML

For the AME model, the open resonator end is modelled with a smaller hemisphere terminated with the PML. This is because larger hemispheres increased the number of spurious modes produced when solving Equation 3.1. Spurious modes are due to non-physical phenomena and the scaling inside the PML [120]. These spurious modes exist outside the resonator domain and are not the resonator's acoustic eigenmodes as seen in Figure 3.7. The contribution from these modes is not considered during modal summation stage of Equation 3.8. This is accomplished by integrating the absolute pressure within the hemisphere and the resonator. The modes with a higher integrated pressure in the in hemisphere compared to the resonator are classified as spurious modes.

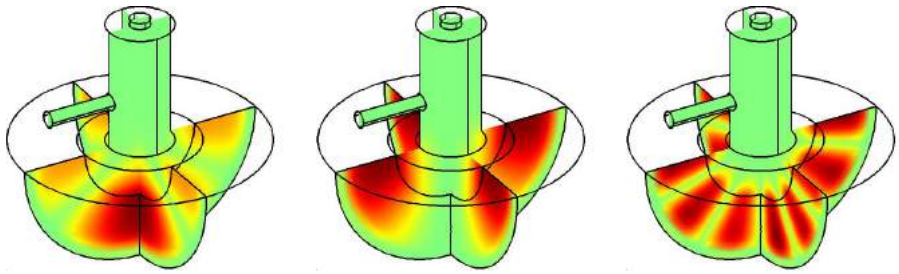

FIGURE 3.7: Distribution of the absolute value of the pressure for some spurious mode (from left to right: 18.5 kHz, 22.8 kHz, 31.8 kHz). Green represents nodes, red represents antinodes

The convergence of the model is checked using 3 different hemispheres with radii of 1.61, 1.785 and 1.8 times the cavity cylinder radius and are shown in Figure 3.8.

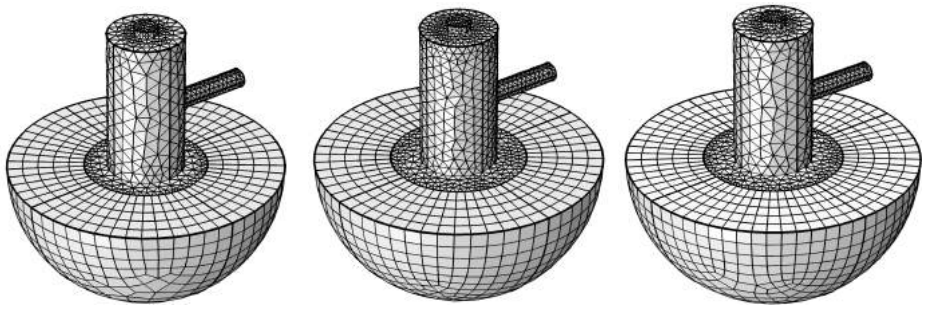

FIGURE 3.8: Mesh of the resonator with three different hemisphere sizes. From left to right: HS 1, HS 2 and HS 3 are hemispheres with radius 1.610, 1.785 and 1.800 times the radius of the opening respectively.

3.4.2 Boundary element method

Boundary element method (BEM) is a numerical method for solving a partial differential equation (PDE) by reformulating it as an integral equation that

is defined on the boundary of a domain. The integral relates the boundary solution to the solution at points in the domain [133], [134]. The method requires the discretization of only the boundary(s) of the domain of the PDE rather than the entire domain (as is the case with finite element method). This is the main advantage of BEM since the number of degrees of freedom solved and the computational time are greatly reduced. As a result, the method is ideal for simulation problems with a finite or semi-finite domain.

BEM give rise to fully populated matrices and hence the computational storage requirements will grow according to the square of the problem size. In contrast to finite element method, matrices are sparsely populated and therefore the computational storage requirements grow linearly with the problem size [120].

A multiphysics coupling between the pressure acoustic module which is used by the AME model and boundary element method module is currently not possible using the COMSOL Multiphysics software. Therefore, PA simulations of the open resonator ending using the BEM are performed only with the viscothermal model (VT-BEM). The viscothermal module is defined inside the resonator domain while the boundary element method is defined in the free space domain. A multiphysics coupling is established at the open resonator end. BEM requires a mesh only at the open boundary which significantly reduces the number of mesh elements in comparison to the PML.

To check the convergence of the VT-BEM approach, two meshes with different sizes were generated. The mesh parameters were kept the same as in the VT-PML approach to enable comparison. The mesh parameters are presented in Table 3.5. Interestingly, for the same mesh quality, the degree of freedom for the VT-PML approach is almost 3 times the VT-BEM approach.

Mesh parameters	**Fine mesh**	**Finest mesh**
Max. element size (mm)	1.429	1.2
Min. element size (mm)	0.481	0.481
Max. growth rate	1.4	1.1
Curvature factor	0.4	0.4
Resolution of narrow region	0.7	0.7
Number of boundary layers	4	4
Boundary layer stretching factor	1.2	1.2
Thickness adjustment factor	3	3
DOF	205272	407242

TABLE 3.5: Properties of the mesh generated for the VT-BEM approach.

Chapter 4

PA measurement setup

4.1 Overview

The photoacoustic measurement in this project are used to validate the results from the simulation models. The measurements are limited to probing a carbon black sample, a broadband absorbing material, to obtain the frequency response of the T-shaped resonator. Quantitative glucose measurements have not been performed. The schematic of the experimental setup is illustrated in Figure 4.1. The experimental work performed in this project can be classified into a set of 3:

- closed resonator measurements
- open resonator measurements
- optimized resonator measurements.

4.2 Optical source

The excitation of the carbon black sample is achieved using a diode laser and a quantum cascade laser. As detailed in Chapter 2, quantum cascade lasers are currently used for PA glucose measurements. The laser was however acquired during the course of this work. Since the carbon black sample can be excited without matching the laser emission to a specific transition, a diode laser was initially used. Diode lasers are readily available and cheap compared to other laser sources and was thus a suitable alternative. The diode laser is used for the closed and open resonator measurements. The quantum cascade laser is used for the optimized resonator measurements.

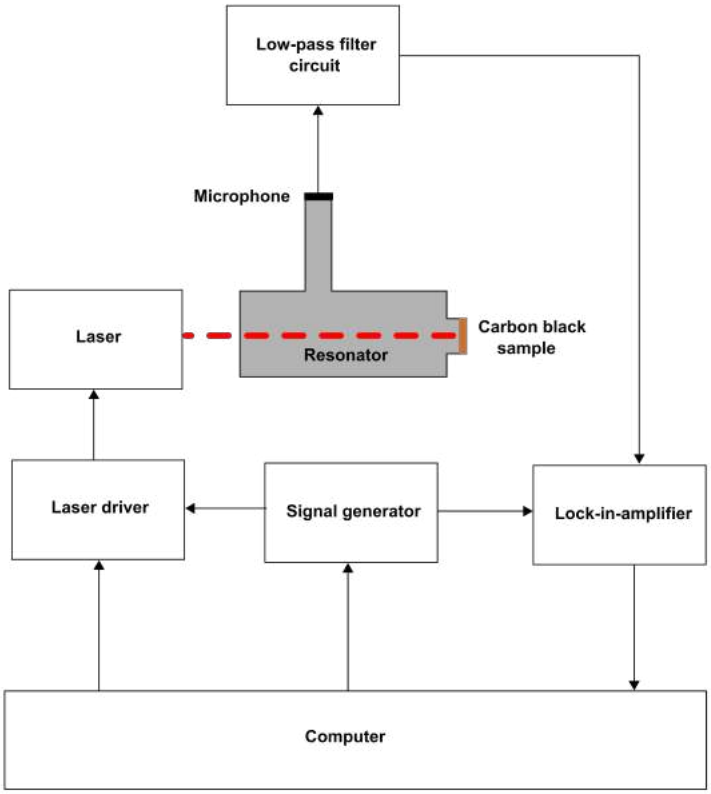

FIGURE 4.1: Schematic of the experimental setup. The arrows indicate the direction of the transmitted signal. The red dashed line represents the modulated laser beam.

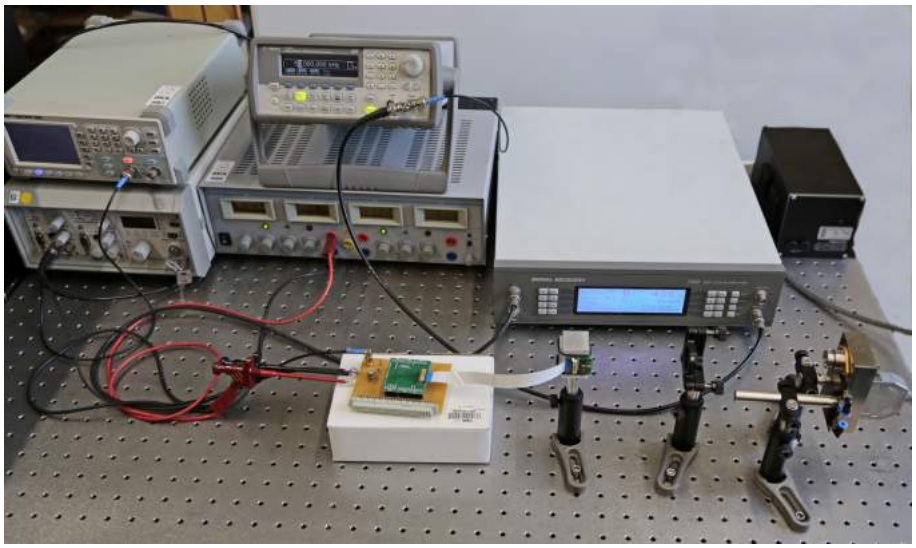

FIGURE 4.2: Photograph of the experimental setup with the quantum cascade laser.

4.2.1 Diode laser

Diode laser is made from doped semiconductor material forming a PN junction. Photons are emitted when an electron and a hole recombine in the depletion area of the p- and n- type material. The depletion area is small in size with the width much larger than the height. As a result, the laser output is asymmetric with the divergence in the horizontal direction relative to the active layer much larger than the vertical divergence. The diode laser beam thus has an elliptical profile.

A CW diode laser (IMM photonics U-LD-651071A) with a wavelength of 655 nm was used for the measurements. A current control unit (LDC 402B, Thorlabs) is used to provide precise control of the laser driving current. A signal generator (Agilent 33220A) producing a square wave of 50 % duty cycle is connected to the current control unit to modulate the laser driving current. The square wave signal is also connected to the lock-in- amplifier to provide the reference frequency for signal detection. The diode laser is used to obtain the frequency response of the T-shaped resonator (4.4) in both closed and open configuration. An average of 10 measurements are recorded with the laser modulation frequency swept between 10 kHz and 60 kHz with an increment of 10 Hz.

4.2.2 Quantum cascade laser

Quantum cascade lasers are semiconductor laser sources where photons are generated from intersubband transitions as illustrated in Figure 4.3. QCL consist of a periodic series of semiconductor quantum well hetero-structures. Electrons are pumped to a given energy level of a quantum well and eventually decay to a lower energy level within the quantum well by releasing a photon. The electron tunnels into the next quantum well where it undergoes another transition to generate another photon. The process is repeated for many periods within the semiconductor thus generating multiple photons of identical wavelength from a single electron. As a result, QCL produce higher output power compared to diode lasers.

QCL can be classified based on their operation as either external cavity quantum cascade laser (EC-QCL) or distributed feedback quantum cascade laser (DFB QCL). In an EC-QCL, the cleaved facets of the semiconductor material has an anti-reflection coating and thus, the material serves as the gain medium. The semiconductor material is placed inside an external optical cavity. A DFB QCL has a periodic grating that is fabricated in the semiconductor material to allows single longitudinal mode operation of the laser.

The PA signal of the optimized T-shaped resonator is excited using a DFB

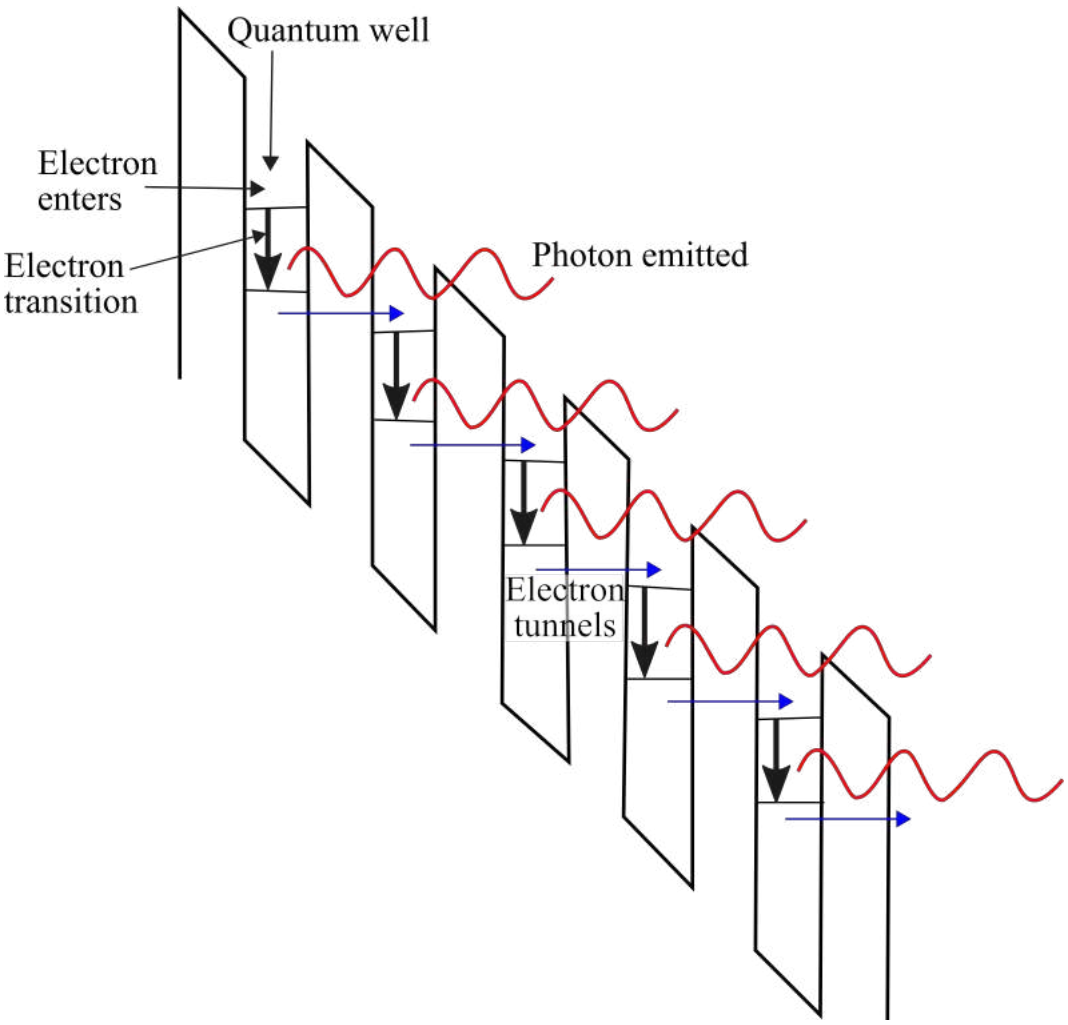

FIGURE 4.3: Typical QCL energy structure of the conduction band [135].

QCL (Nanoplus, Oberer Kirschberg, Germany). The laser emission wavelength is between 9200 nm to 9250 nm which covers a strong glucose absorption peak at 1085 cm^{-1} and would be ideal for future glucose measurements. Since the measurements are performed on a carbon black sample, tuning the laser wavelength to match a particular transition is not necessary.

The laser is operated using a driver (Q-MACS SC, Griefswald, Germany) that has a built-in control loop system for the laser current, voltage and temperature. The pulse generation of the DFB QCL is triggered using a square wave signal produced by the signal generator (Agilent 33220A). The frequency of the square wave during the measurements is swept between 10 kHz to 60 kHz with 30 Hz interval. To compare the signal improvement of the optimized T-shaped resonator, the open resonator measurement is performed using the DFB QCL between 46 kHz to 54 kHz with 30 Hz increment.

The laser temperature is maintained at 16 °C during the measurements and produced pulses of 100 ns width. The average power of the laser is

recorded using a power meter (Thorlab S401C) at different pulse repetition rates. To account for the laser power fluctuations during the measurements, the measured PA signal is normalized according to the laser power.

4.3 Acoustic resonator

In this project a T-shape resonator is used. Typically, T-shaped resonators are formed using two cylinders, an absorption cylinder where laser absorption by the sample occurs and a perpendicularly mounted resonance cylinder where PA detection occurs, forming a T-like structure. Compared to a cylindrical resonator design, the T-shaped resonator design allows for independent optimization of the key parameters affecting signal strength [121], [125].

The T-shaped resonator used for PA glucose measurements is however, formed using three interconnected cylinder, i.e. the so called cavity cylinder, absorption cylinder and resonance cylinder. The large cavity cylinder is longitudinally connected to a smaller absorption cylinder and a horizontally intersecting resonance cylinder as illustrated in Figure 4.4. The sample is placed at the end of the small absorption cylinder while a digital micro-electro-mechanical system (MEMS) microphone is placed at the end of the resonance cylinder which in effect seals these resonator ends. The absorption cylinder end where the sample is placed has a smaller radius compared to the cavity cylinder so as to minimize changes caused by skin shape deformation during PA glucose measurements [110]. The cavity cylinder end where the laser beam enters the resonator can be sealed using a polycarbonate window with 85 % optical transmission in the visible spectral region. The resonator is operated in a closed configuration when the window is used and in an open configuration without the window.

The T-shaped resonator with similar dmension to the one used by Pleitez et al. [61], [110] for glucose measurements was produced. After the production of the resonator, the accuracy of the resonator dimensions was checked using a high precision optical scanner (ZEISS MICURA, ZEISS, Oberkochen, Germany) of 1 µm resolution that revealed deviations in the resonator dimensions. Ideally, the resonator dimensions from the point measurement would be used in the simulations since resonance amplification strongly depends on the geometry of the resonator. However, this would be computationally very demanding and would make the simulation time longer. An average of the point measurements is made for each resonator dimension and are used as the resonator dimensions during the simulations. These average dimensions are depicted in Figure 4.4.

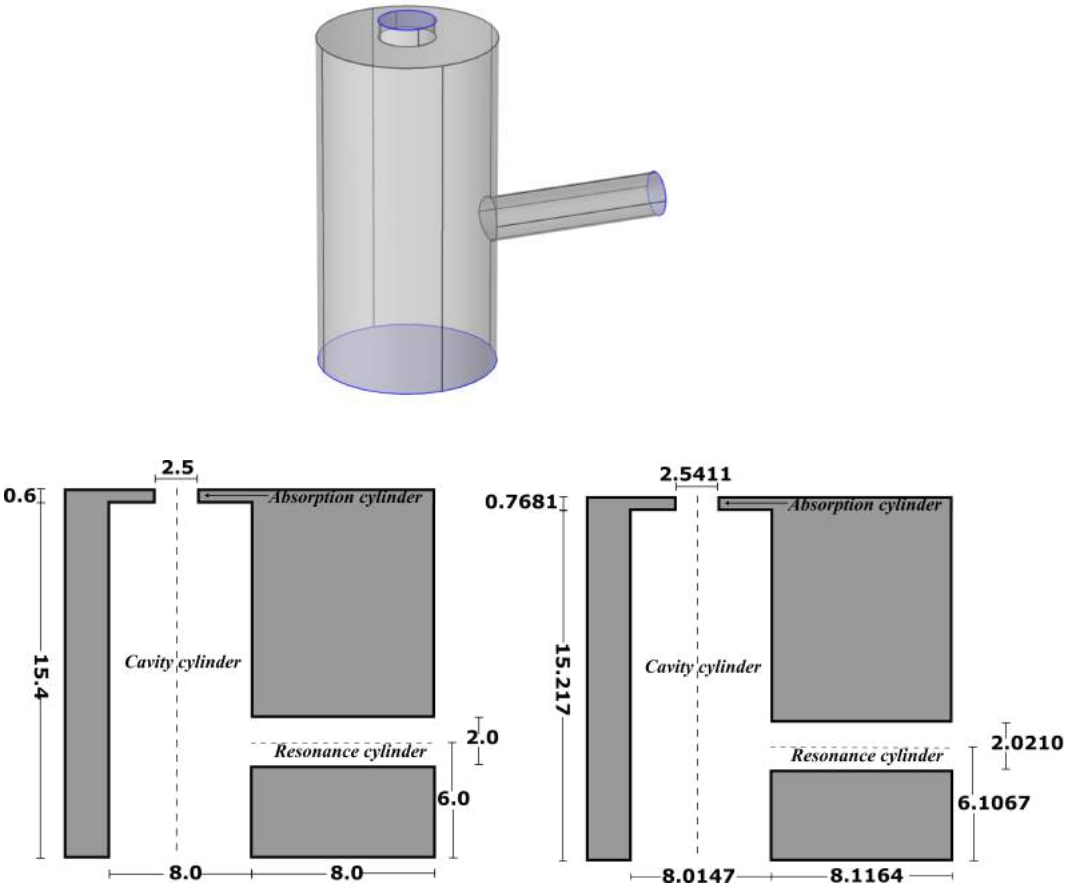

FIGURE 4.4: Top: the T-shape resonator with the openings highlighted in blue. Bottom: schematic of its cross-section (white) showing the size of each cylinder in mm. The dimensions of the resonator used by Pleitez et al. (left) [61], [110]. The mean values from high precision measurement of the produced resonator (right) [136]. The dashed lines represent cylindrical symmetry.

4.4 Acoustic detector

A digital MEMS microphone (Knowles SPH0641LU4H-1) is used to detect the PA signal generated by the laser excitation. The microphone is optimized for detection of acoustic waves with frequencies between 100 Hz to 80 kHz making it ideal for this application. The microphone is enclosed in a package size is 3.5 mm long, 2.65 mm wide and 0.98 mm thick which protects the microphone from mechanical damage and electromagnetic radiation. The microphone package is mounted onto the resonator using a printed circuit board (PCB). A PCB for the microphone was designed and manufactured. A sensor for measuring the ambient temperature and pressure is integrated in the PCB design. This sensor was not used during this work, however,

would be useful in future PA measurements on patients. The schematic of the microphone's PCB is attached in the appendix.

The MEMS microphone has a resonance around 25 kHz and a fairly flat frequency response between 35 kHz and 65 kHz as seen in Figure 4.5.

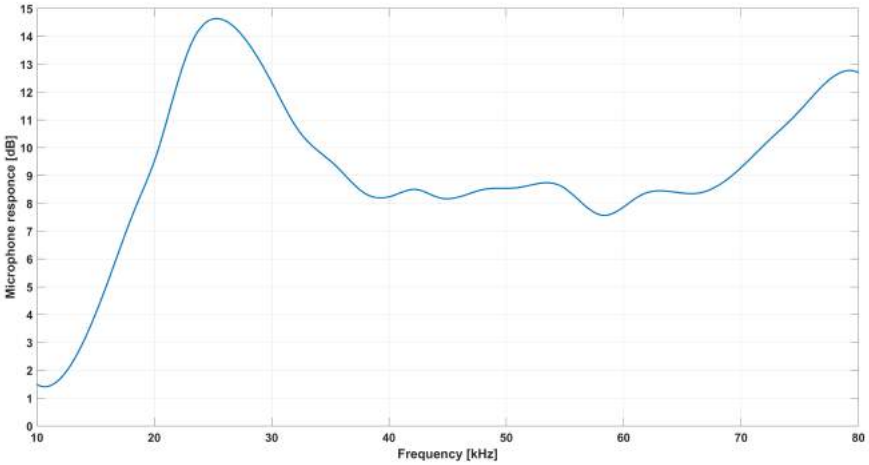

FIGURE 4.5: frequency response plot of the MEMS microphone [132]

The microphone is equipped with an analogue to digital converter and a pulse density modulator inside its enclosure. As a result, its output is a digital pulse density modulated signal (PDM). To filter out noise from the signal, a lock-in amplifier (Signal Recovery7265 DSP Lock-in-Amplifier) with a time constant of 100 ms is used. The lock-in amplifier has an analogue input port, therefore, the digital output from the MEMS microphone is first passed through a low-pass filter circuit for demodulation before being feed to the lock-in-amplifier.

The digital output interface of the MEMS microphone is designed such that two microphone outputs are multiplexed on a single data line using a single clock. The output pulse train of one microphone is transmitted in the first half of the sampling period with the other microphone transmitting in the second half. In this application, only one microphone is used causing a discontinuous pulse train since there is no output in one half of the sampling period. This lowers the overall sensitivity of the setup since the analog output voltage from the low-pass filter circuit digital to analogue conversion (DAC) process is the product of the converter operating voltage and the PDM duty cycle. In this case, the PDM pulse duty cycle is 50 % from the discontinuity which in turn halves the maximum possible output from the digital to analogue conversion and hence the signal-to -noise ratio.

The output from the lock-in-amplifier is recorded on a computer.

4.5 Results

4.5.1 Closed resonator

The simulation results from the AME model, VT model and measurement for the closed T-shaped resonator are shown in Figure 4.6. Both simulation models are performed using a 64-bit computer with a processor speed of 2.5 GHz and 32 GB RAM using COMSOL Multiphysics version 5.2. The simulations with the AME model with 10 Hz increment took 7 minutes whereas the VT model with 50 Hz increment took 1 week.

The models predict a similar frequency response for the resonator albeit with small shifts in the peak resonance frequency of not more than 1.8 %. The differences are expected since the losses in the AME model are estimated using quality factors while the VT model accurately captures the losses at the resonator walls using boundary layers. From the pressure distribution plots in Table 4.1 longitudinal modes are attributed to the resonances at low modulation frequencies lower than 30 kHz and at frequencies above 50 kHz, radial modes are also supported which could account for the increased number of resonances. The overlapping of resonances from two degenerate modes at 49.2 kHz to 49.5 kHz (see Table 4.1) is responsible for the broad resonance peak between 48 kHz and to 51 kHz.

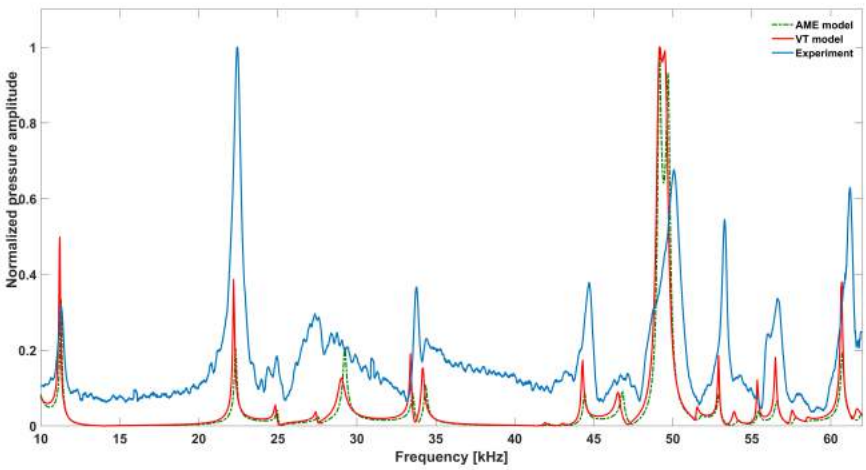

FIGURE 4.6: The frequency response plot of the closed cell configuration using the AME model, VT model and experimental measurements [91]

The AME model is observed to overestimate bulk loss effects and underestimate surface loss effects in comparison to the VT model. The relative height of the resonance amplitudes of the AME model to the VT model depended on the location of the antinode within the resonator. When the antinode is mainly located in the resonance cylinder where the surface area to

volume ratio is large, the AME model underestimates the losses in comparison to the VT model. This results in larger amplitudes than the latter (the resonance amplitude ratio of AME/VT model was >1). However, when the antinode is in the cavity cylinder, where the surface area to volume ratio is small, the AME model slightly overestimates the losses in comparison to the VT model (resonance amplitude ratio <1) as shown in Table 4.1. The two effects mitigate each other in cases where the antinode is in both cylinders (resonance amplitude ratio close to 1).

f_{res} in kHz	$\lvert p \rvert$-profile of acoustic mode	location of antinodes	$\frac{A^{AME}(f_{res})}{A^{VT}(f_{res})}$
11.20	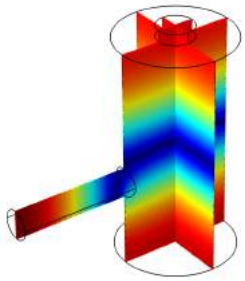	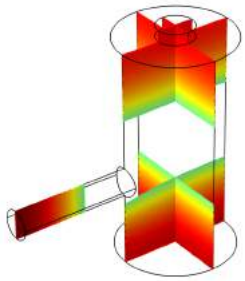	0.91
22.20	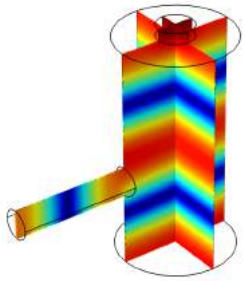	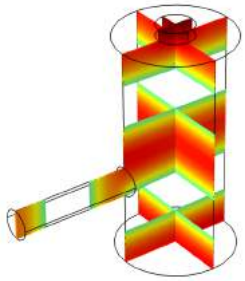	0.71
29.05	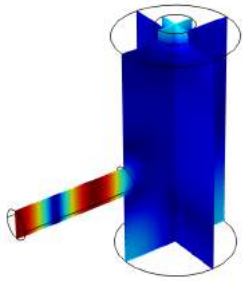	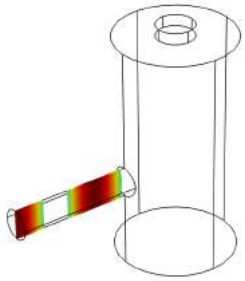	2.23
33.40	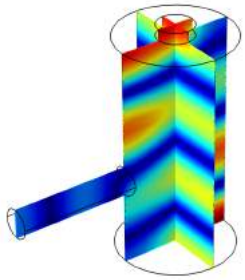	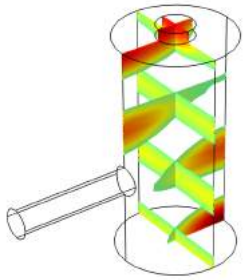	0.59
34.20	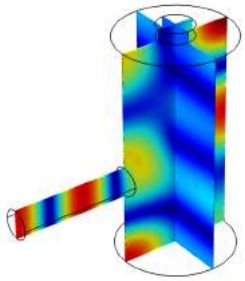	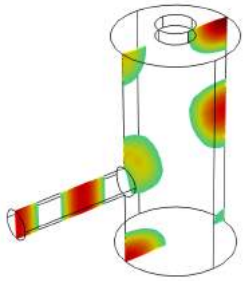	0.97

f_{res} in kHz	$\lvert p \rvert$-profile of acoustic mode	location of antinodes	$\frac{A^{AME}(f_{res})}{A^{VT}(f_{res})}$
44.30	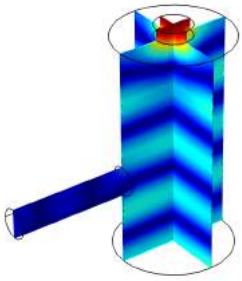	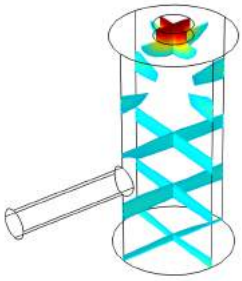	0.68
46.55	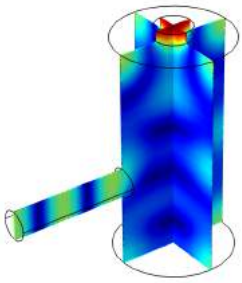	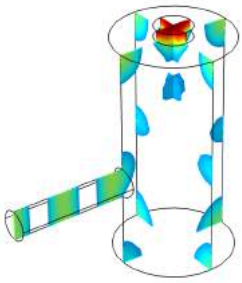	1.42
49.20	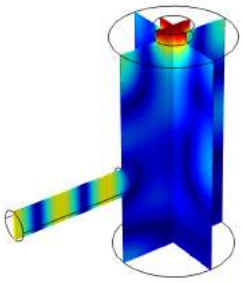	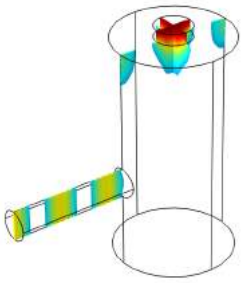	1.30
49.50	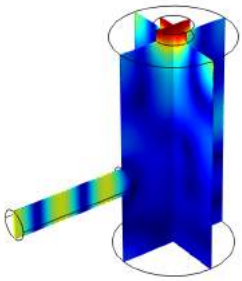	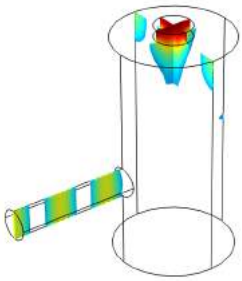	1.27
52.90	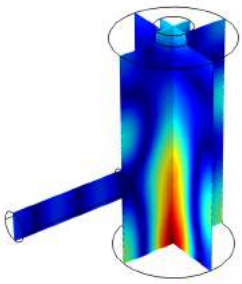	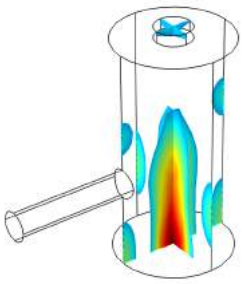	0.60

f_{res} in kHz	$\lvert p \rvert$-profile of acoustic mode	location of antinodes	$\frac{A^{AME}(f_{res})}{A^{VT}(f_{res})}$
55.35	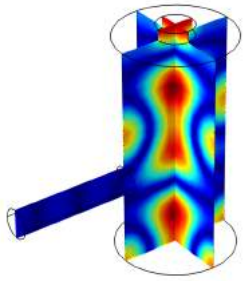	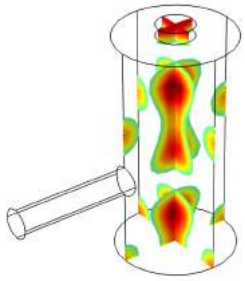	0.47
56.50	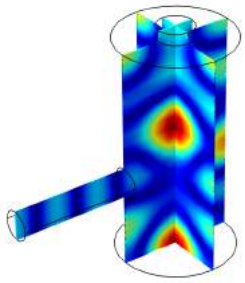	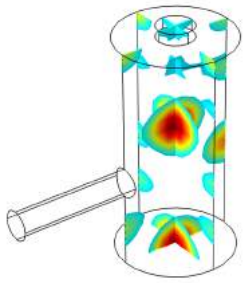	0.49
60.70	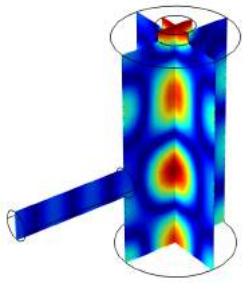	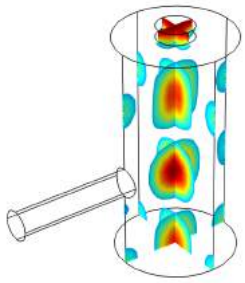	0.65

TABLE 4.1: Resonance frequency, corresponding mode, location of strong antinodes and amplitude ratio for the strongest resonances. The location of the antinodes has been determined by lifting the lower limit of the depicted data range appropriately [91]

The simulation models show fairly good accordance with the measurements since almost all the resonances are experimentally detected. The signal to noise ratio of the measurements is 29.411 and is calculated from the resonance at 50 kHz as a ratio of the mean to the standard deviation. The relative difference in the peak resonance frequency of the measurement with the VT model is not more than 1.1%. The shift might be caused by temperature variations of the air within the resonator or losses in the experimental setup. Temperature variations during measurements can affect the speed of sound and shift the resonance frequencies. Losses within the measurement system can be attributed to leakage of the PA signal at the microphone mount. The simulation model assumes that resonator end sealed by the microphone mount is a sound hard wall.

The significant difference in the simulated and measured Q factors supports the idea of a loss mechanism within the setup. Table 4.2 compares the Q factors of the most prominent resonances of the measurements against the viscothermal model. The Q factors were calculated according to Equation 4.2.

f_{res} **in kHz**	Q_{VT}	Q_{mes}
11.2	80	19
22.2	123	34
44.3	211	55
52.9	353	124
60.7	304	80

TABLE 4.2: Resonance quality factors of simulated and measured resonances [91]

The measurement setup has high base noise level that can be attributed to the laser beam interaction with the window. Light scattering at the window can cause mechanical vibrations through the transfer of the photon momentum to the window surface. The window has 85% transmission in the visible range and window absorption can generate coherent acoustic signal. Furthermore,the edges of the diode laser's elliptical beam are suspected to induce resonator wall excitation. The base noise level is highest between 35 kHz to 40 kHz. It is suspected that one of the small simulated resonances in the range could not be distinguished in the measurement as a result. The simulated resonances between 55 kHz to 57 kHz could not be resolved in the measurements as they are merged due to resonance broadening.

The strongest measured resonance is at 22.2 kHz. However, the simulation results do not reflected by the simulation results. It is suspected that the strength is caused by synergistic resonance amplification by both the resonance and the MEMS microphone whose frequency response has a resonance in this frequency range.

4.5.2 Open resonator

Figure 4.7 shows the results from the convergence study of the VT-BEM, VT-PML and AME-PML approaches for simulating the PA signal in an open T-shaped resonator. To prevent overlapping of the curves and thus enable easy viewing, the plots have been re-scaled and the pressure amplitudes presented in a logarithmic scale.

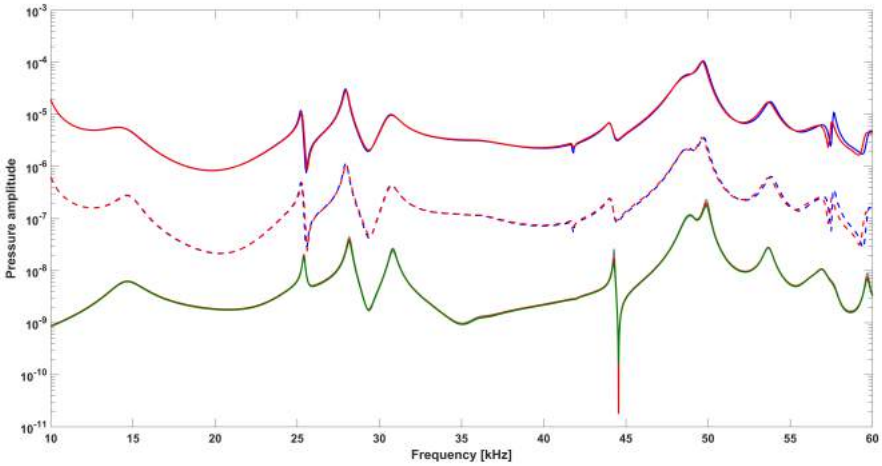

FIGURE 4.7: Frequency response of the different models. The upper solid lines represent the VT-PML results, the middle-dashed lines represent the results from the VT-BEM approach (blue: mesh 1, red: mesh 2). The lower full lines represent the results from AME-PML model with different hemispheres (grey, red and green refer to HS 1, HS 2 and HS 3 respectively) [132]

The convergence study of the AME model using three different hemispheres indicates that the model is approaching the solution since similar resonant frequencies were produced. Small differences in the amplitudes are observed probably from the influence of the PML. The VT model using the PML and BEM has generated similar spectral features indicating that the simulations are converging towards the solution. However, the mesh resolution at frequencies above 55 kHz needs to be improved as demonstrated by the slight resonance frequency shifts and differences in the amplitude from the different mesh sizes.

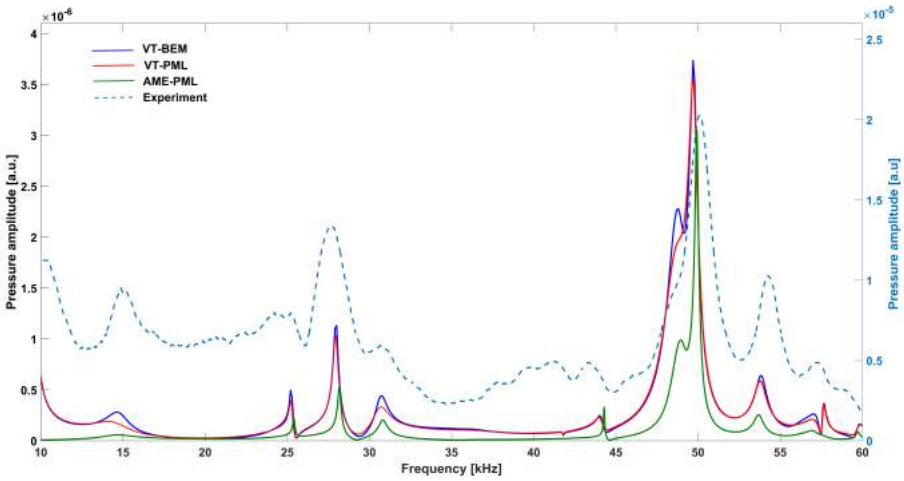

FIGURE 4.8: Frequency response of the experiment against the simulations for the open resonator configuration [132].

The frequency response of the open cell configuration shows fairly good agreement between the VT-PML (fine mesh), VT-BEM (fine mesh) , AME-PML (HS 1) and the measurements as seen in Figure 4.8. The major resonances from the simulations have been measured. The peak frequency of the measured resonances is shifted by less than 1.04 % compared to the peak frequency of the VT-PML approach. Like with the closed configuration, the damping in the measurement system is high as reflected by the larger width of the measured resonances compared to the simulation. Furthermore, the high base noise levels make it difficult to distinguish the resonances with small amplitudes. A signal to noise ratio of 16.46 is calculated from the strongest resonance as a ratio of the mean to the standard deviation.

The resonances from the AME model have narrower widths and are slightly shifted to higher frequencies compared to the VT model. This is expected since the thermal and viscous losses are estimated using quality factors while the VT model uses boundary layers to accurately captures the losses at walls of the resonator.

The two VT approaches are in very good agreement. The peak resonant frequencies of the VT-BEM are shifted to higher frequencies by less than 0.2 %. The amplitudes from the VT-BEM approach are slightly higher compared to the VT-PML approach indicating that the VT-BEM approach under calculates the losses. VT-PML mirrors the measurements most accurately compared to the other approaches hence can be considered the most accurate of the three approaches.

The wide resonance between 45 kHz to 52 kHz is as a result of superposition of close lying resonances. The resonator eigen modes responsible for the resonance are obtained from the AME-PML approach and illustrated in Figure 4.9.

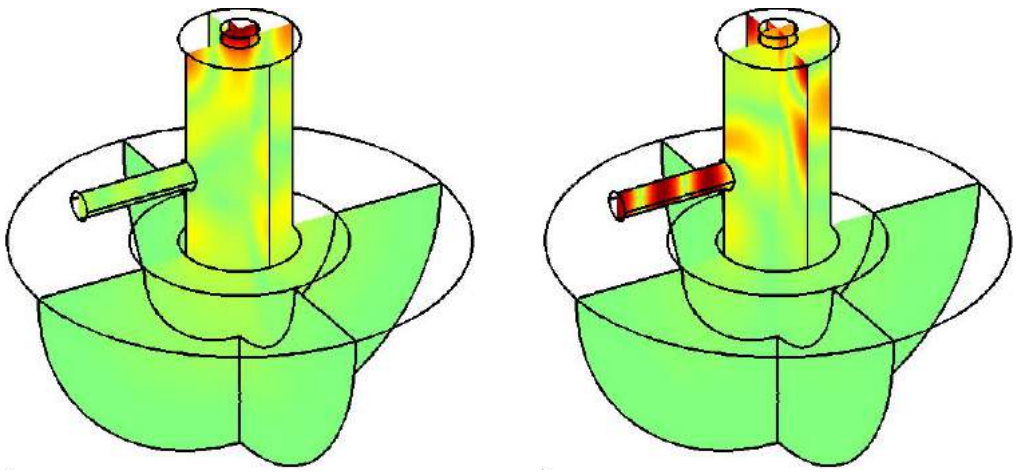

FIGURE 4.9: The acoustic modes showing the absolute value of the pressure at 49 kHz and 49.9 kHz respectively. The plots are normalized by the highest value of the individual plot.[132]

The VT-BEM and AME-PML approach underestimate losses compared to

the VT-PML. This is because both models (VT-BEM and AME-PML) have a peak like feature on the wing of the broad resonance 45kHz to 52 kHz. This feature is diminished in the VT-PML approach much like in the measurements and as a result, the VT-PML approach is rated the most reliable approach.

The VT-PML approach requires longer computational time compared to the VT-BEM approach. This is attributed to the hemisphere which introduces the extra region for the model to solve the equations. Thus the VT-PML model has extra degrees of freedom that the model must calculate. The VT-PML took ca. 102 hours to simulate a10 kHz range with 10 Hz increment while VT-BEM approach took approximately 21 hours for the same range using 2 Intel Xeon CPUs with 14 cores each, running at 2.6 GHz with 384 GB of RAM.

Chapter 5

Optimization of an open PA resonator

5.1 Introduction

Optimization is an important tool for improving the performance of devices, improving its design or finding new solutions. The interest in numerical optimization methods has greatly increased with the improvement of computational capacity that enables engineers and scientists to investigate complex systems.

In an optimization problem, a quantitative measure of a device's performance referred to as the objective function, is either maximized or minimized. The objective function is dependent on the device's characteristics called variables. The relation between the variables and the objective function is described using the governing equations. The optimization process selects the best combination of variables from a set of defined variables that results in the minimization (or maximization) of the objective function. Numerical optimization can be categorized into 3 parts [137]:

- Parameter optimization is used to reliably determine the values of a set of parameters that provide simulated data which best reflects the measured data [137]. An example of parameter optimization is solving inverse problems that are widely used in biomedical imaging and curve fitting problem.
- Topology optimization is used to maximize the performance of a system by considering the best material lay out within a design space for a given set of constraints. This approach allows for the design to take any shape within the design parameters and as a result enable the realization of new, non-intuitive designs.
- Shape optimization is used to find the geometrical dimensions of a certain shape that maximizes performance of a system under certain constraints. Unlike topology optimization, the design shape is fixed.

The numerical and experimental optimization of a photoacoustic setups has been reported in numerous studies. This chapter focuses on numerical optimization. Some of the experimental optimization of PA setups includes using more sensitive detection system like quartz tuning fork [138] that increase the sensitivity of the method, replacing the mechanical chopper with an electro-optical modulation system [89] that reduces background noise from the chopper and using a multi-pass photoacoustic resonator [139], [140] that increases the optical path length. Some studies have employed a differential cell that consists of two acoustic resonators with microphones having the same responsivity at the resonance frequency of the cell [141]. The PA signal is generated in only one of the two resonators and the difference between the two signals removes noise components that are coherent in both resonators.

5.2 Numerical optimization of PA resonators

A standard method for optimizing PA resonators is not available with different approaches reported. Bijnen et al. [109] optimized the sensitivity of a cylindrical resonator capped with buffer volumes (H-cell resonator) used for trace gas application. They employed the transmission line model to calculate the PA signal and established that larger buffer volume radii sufficiently suppressed background signals caused by window absorption and improved the sensitivity of the measurements. Furthermore, they investigated the effect of positioning an additional cylindrical volume referred to as tunable air columns close to the window to further reduce the signal resulting from window heating. The signal was effectively suppressed when the length of the tunable air columns is half the resonator's length. Cai et al. [142] and Tavakoli et al. [122] have also used the transmission line model to optimize the buffer volume of H-cell resonators to realise a high sensitivity and signal to noise ratio.

Optimization efforts based on finite element modelling of the PA signal have mostly been performed on closed resonators using the AME model to calculate the PA signal. Baumann et al. [143] optimized the PA signal of H-cell resonator using the AME model. The resonator was split into axially symmetric cones of equal length before optimizing the shape of each individual cone. The optimized resonator had an hourglass shape and a signal improvement of 32% compared to the original H-cell. Experimental confirmation showed an increment of around 13%. Risser et al. employed the AME model to optimize the dimensions of a differential Helmholtz resonator for maximum PA signal. They reported good agreement between the simulation and the measurements from the chosen resonator dimensions [144].

Cottrell et al. [145] optimized a single cylindrical resonator capped with cylindrical buffer volumes used for aerosol detection by employing the VT

model. The studies were aimed at improving the signal to background ratio and the results were verified with experimental measurements. They demonstrated that signal to background ratio (SBR) is maximized by using buffer volumes with large radii and with lengths half the length of the resonator. The inclusion of tunable air columns improved the SBR however, they concluded that its impact depends on the dimensions of other cell domains. Later, they extended their study by optimizing the geometry of a two-resonator PA cell used in aerosol detection applications with the aim of improving the signal to background ratio. Their results showed the optimal buffer volume length for the resonator was 0.7 times the resonator length. Their study concluded that the general rule of setting the buffer length to half the resonator length was not universal [146].

Haouair et al. [147] performed topology optimization of a closed cylindrical resonator using the VT model to maximize the sound pressure at the location of the microphone. The optimized resonator had a shape that resembled a potato and had increased the photoacoustic signal by a factor of two. Topology optimization of PA acoustic resonator has rarely been demonstrated due to the difficulty of manufacturing resonators with unconventional geometries. This is underlined by the fact that experimental confirmation of the simulation results has yet to be performed.

Numerical optimization of open PA resonators, to the best of my knowledge, has not been demonstrated using finite element modelling. In this work, the optimization of an open T-shaped resonator for maximum signal detection in the ultrasound range is demonstrated using finite element modelling.

5.3 Optimization method

The procedure for optimizing the geometry of the open T-shaped resonator designed for PA glucose measurements is described. The objective function is to maximize the signal detected at the location of the microphone. The resonator's geometrical dimensions are selected as the optimization variables and are related to the objective function using the VT-PML model. The VT-PML model is selected for calculating the PA signal since it showed the best accordance with the experimental measurements compared to the VT-BEM and AME-PML approach.

Non-invasive PA glucose measurements utilize the resonance at around 50 kHz [110] which is formed by a superposition of two close lying resonances between 48 kHz and 51 kHz. The PA signal is calculated using the VT-PML approach in this range using the finest mesh (mesh details found in Table 3.4).

The dimensions of the cavity cylinder and the resonance cylinder are particularly determining for the resonance frequency. This is because the main resonator modes reside in the cavity cylinder and PA detection occurs at the end of the resonance cylinder. Therefore, their geometrical parameters are selected as variables for the optimization.

A course parameter sweep of the cylinders is performed in two stages. In the first stage, the resonance cylinder length and its position are changed, in the second stage only the cavity cylinder length and radius are changed. In both stages, all other resonator dimensions are left unchanged. This approach enables better insight on the effect of each variable to the detected PA signal. The insight gathered during the paramtere sweep would hopefully help reduce reduce the optimization search space. The resonator's acoustic modes which are utilized for the PA signal amplification are dependent on all the geometric dimensions of the resonator, therefore this two-stage approach investigates a limited range of possibilities.

5.3.1 Resonance cylinder sweep

A resonance cylinder sweep is performed by varying its length and position of insertion along the cavity cylinder. The length is varied from 0 mm (without resonance cylinder) to 17 mm in 1 mm intervals. The position of the resonance cylinder along the cavity cylinder is described relative to the the open end. The resonance cylinder is moved from the open end of the cavity cylinder to the end where the absorption cylinder is connected in 1 mm intervals, that is between 2mm and 14 mm. All possible combinations of the resonance cylinder position and length are explored while keeping the other resonator dimensions constant as shown in the Table 5.1.

The highest PA signal value of each parameter sweep combinations S_{sweep}, is normalized with regard to the highest PA signal value of the reference resonator of the resonance at 50 kHz S_{ref}. The normalization is used to demonstrate the quality of the solution for each parameter combination relative to the reference resonator. The ratio is referred to as the quality ratio ζ in this work and is defined as

$$\zeta = \frac{S_{sweep}}{S_{ref}}. \tag{5.1}$$

The results of the resonance cylinder sweep are presented in Figure 5.1. The discussion is limited to six peaks whose quality ratio is more than 1.5. The peaks are observed when the length of the resonance cylinder is 1 mm, 8 mm and 15 mm while its position along the cavity cylinder is at either 4 mm or 5 mm and at 12 mm.

Resonator parameters	Reference cylinder dimensions	Range of sweep	Increment step
Resonance cylinder length	8.1146	0 - 17	1
Resonance cylinder position	6.1067	2 - 14	1
Resonance cylinder radius	1.0105	-	-
Cavity cylinder length	15.2713	-	-
Cavity cylinder radius	4. 00735	-	-
Absorption cylinder length	0.7681	-	-
Absorption cylinder radius	1.27055	-	-

TABLE 5.1: The resonator dimensions in mm used in the resonance cylinder sweep.

The resonance cylinder supports a longitudinal acoustic mode as depicted in Figure 5.2. According to Miklós et al. [94] resonance occurs in an open–closed cylinder when its length is equal to an odd integer multiple of the quarter wavelength.

$$L = \frac{(2m-1)c}{4f}. \tag{5.2}$$

Where m=1,2,3.... The terms c and f are the speed of sound and resonance frequency respectively. L represents the length of the cylinder together with the so-called end correction. Independently, the resonance cylinder can be seen as an open-closed resonator. Assuming that the resonance frequency is 50 kHz, the speed of sound is 343 m/s^2 and using Equation 5.2, its lengths for m=1 to m=5 are 1.72 mm, 5.15 mm, 8.58 mm, 12.01 mm and 15.44 mm. Thus it can be concluded that the peaks at 1 mm, 8 mm and 15 mm are due to resonance effect. At the same resonance cylinder position, the quality ratio is highest when the length is 8 mm compared to 1 mm and 15 mm, however the difference is small.

The antinodes in the cavity cylinder are suspected to be located at either 4 mm or 5 mm and at 12 mm. When cavity cylinder position coincides with

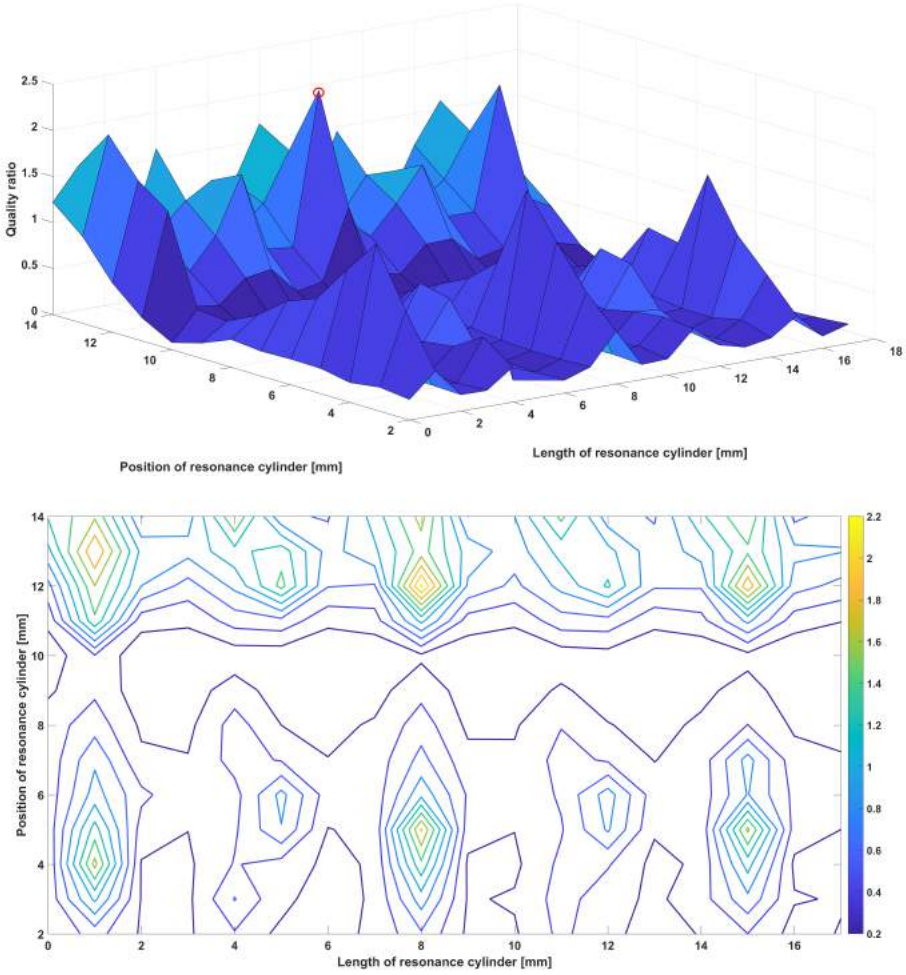

FIGURE 5.1: Above: Quality ratio of all the possible combinations of the resonance cylinder parameter sweep. The highlighted peak is the region with the highest increment. Below: Contour plot of the resonance cylinder parameter sweep. The colour scale gives the values of the quality ratio.

their location, they are coupled into the resonance cylinder. At the same resonance cylinder length, the quality ratio is higher when the resonance cylinder is located at 12 mm than when located at either 4 mm or 5 mm. Therefore, it can be concluded that the position of the resonance cylinder along the cavity cylinder affects the strength of the signal more than the length of the resonance cylinder. This is reflected in the pressure distribution plot in Figure 5.2. The pressure distribution inside the cavity cylinder changes by changing the position of the resonance cylinder and is fairly similar when only the resonance cylinder length is changed.

The highest quality ratio value of 2.2 is observed when the resonance cylinder is located 12 mm from and has a length of 8 mm (highlighted in Figure 5.1). A finer parametric sweep of this search space is performed by changing the resonance cylinder length between 7 mm to 9 mm with 0.1 mm

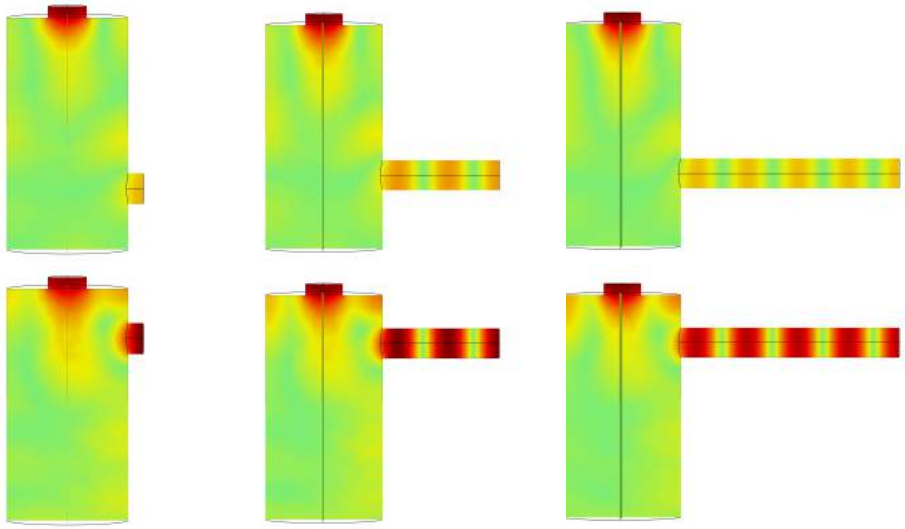

FIGURE 5.2: The absolute pressure distribution plots of the six peaks. The hemisphere with the PML representing the free space domain is not shown. Top: resonance cylinder position 4 mm (left) and 5 mm (middle and right). Bottom: resonance cylinder position 12 mm. The length of the resonance cylinder is 1 mm, 8 mm and 15 mm respectively.

step size while the position is varied between 11 - 13 mm with 0.1 mm intervals. Figure 5.3 shows the results from the finer parametric sweep. The highest quality ratio value from the finer sweep increased from 2.2 to 2.5.

5.3.2 Cavity cylinder sweep

The cavity cylinder radius is swept between 2 mm and 5 mm in 0.5 mm step size while the length was swept between 12 mm to 24 mm in 1 mm step size. All possible combinations of the cavity cylinder radii and lengths are explored with all the other resonator dimensions kept constant as shown in Table 5.2.

The peak amplitude from all the combinations is normalized as described for the resonance cylinder sweep. The results from the cavity cylinder parameter sweep are presented in Figure 5.4. The quality ratio is higher than 1 (indicating an increase in the PA signal relative to the reference resonator) when the cavity cylinder radius ranges between 3.5 mm and 4.5 with a optimum radius of 4 mm. Cavity radii outside this range resulted in a lower signal compared to the reference resonator.

When the cavity cylinder radii is 4 mm, increasing the length of the cylinder from 15 mm to 17 mm increased the quality ratio. The quality ratio decreases when the length is longer than 17 mm. The highest quality ratio of 2.2

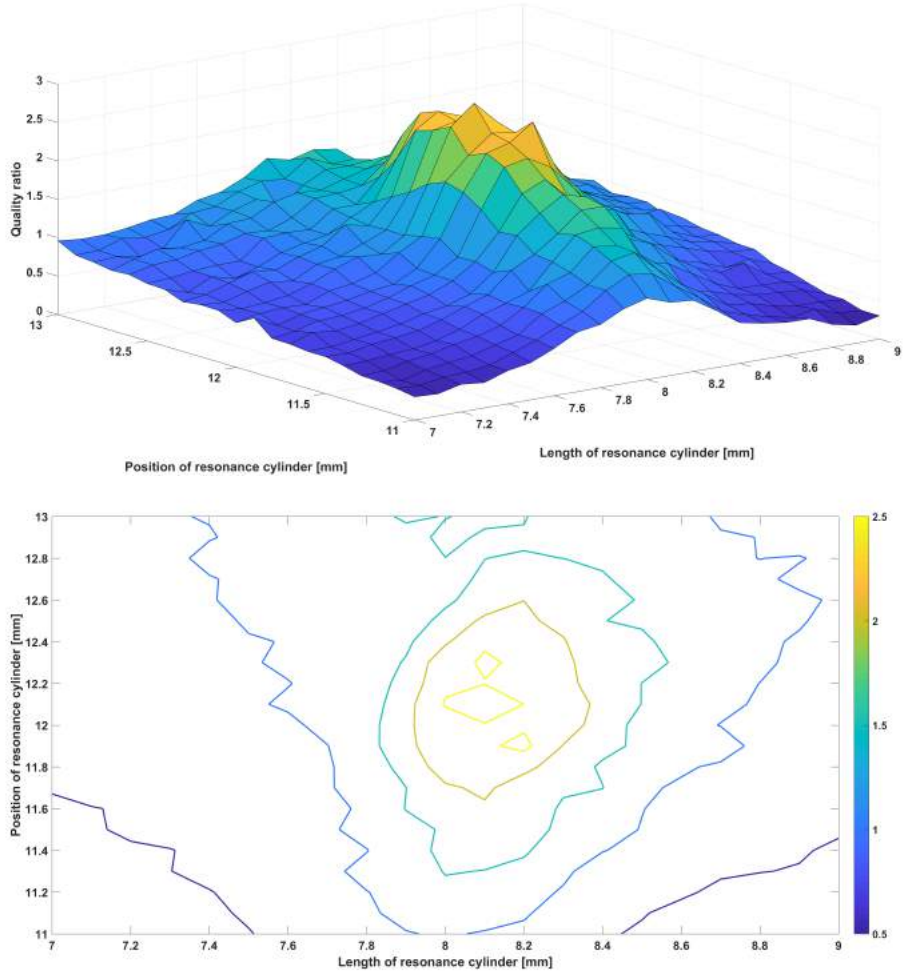

FIGURE 5.3: Above: Quality ratio of all possible combinations for the finer resonance cylinder sweep. Below: contour plot of the finer resonance cylinder sweep. The color scale gives the values of the quality ratio.

is observed when the cavity cylinder length reaches 17 mm and the radius is 4 mm (highlighted in Figure 5.4).

From the two stages of the parameter sweep, the length of the cavity cylinder and the position of the resonance cylinder caused the most significant signal improvement. In a final stage, a finer parameter sweep of these two variables is performed. The cavity cylinder length is changed in the search space where the highest quality ratio is obtained, that is between 16.6 mm and 17.3 mm with 0.1 mm step size. The resonance cylinder position is swept in the two locations where the cavity cylinder antinode are expected, that is between 11.5 mm to 14 mm and 5.5 mm to 6.5 mm from the open end with 0.5 mm step size. The resonator dimensions for the sweep are illustrated in Table 5.3.

Resonator parameters	Reference cylinder dimensions	Range of sweep	Increment step
Resonance cylinder length	8.1146	-	-
Resonance cylinder position	6.1067	-	-
Resonance cylinder radius	1.0105	-	-
Cavity cylinder length	15.2713	12 - 24	1
Cavity cyl. radius	4. 00735	2 - 5	0.5
Absorption cylinder length	0.7681	-	-
Absorption cyl. radius	1.27055	-	-

TABLE 5.2: The resonator dimensions in mm used in the cavity cylinder sweep.

The quality ratio from the combined parameter sweep of both the resonance cylinder and the cavity cylinder are presented in Figure 5.5. The highest quality ratio of 3.5 is obtained when the resonance cylinder position is between 5.5 mm to 6.5 mm and the cavity cylinder is 17.1 mm long (highlighted in Figure 5.5). A lower quality ratio of around 2 is obtain when the resonance cylinder is located further away from the resonator opening (between 11.5 mm and 14 mm). The quality ratio is lower than the value obtain during the resonance cylinder sweep. Changing the cavity cylinder length affects the pressure distribution within the cavity cylinder which accounts for the decrease. This demonstrates the disadvantage of this two stage approach and the importance of performing an optimization of all the geometric resonator dimensions.

5.3.3 Optimization model

The optimization is carried out using COMSOL Multiphysics's optimization module on a 2 Intel Xeon CPUs with 14 cores each, running at 2.6 GHz with 384 GB of RAM. The module's optimization algorithm is described as either gradient based or gradient-free. Gradient based algorithms calculate first order derivatives of the objective function with respect to the control variables.

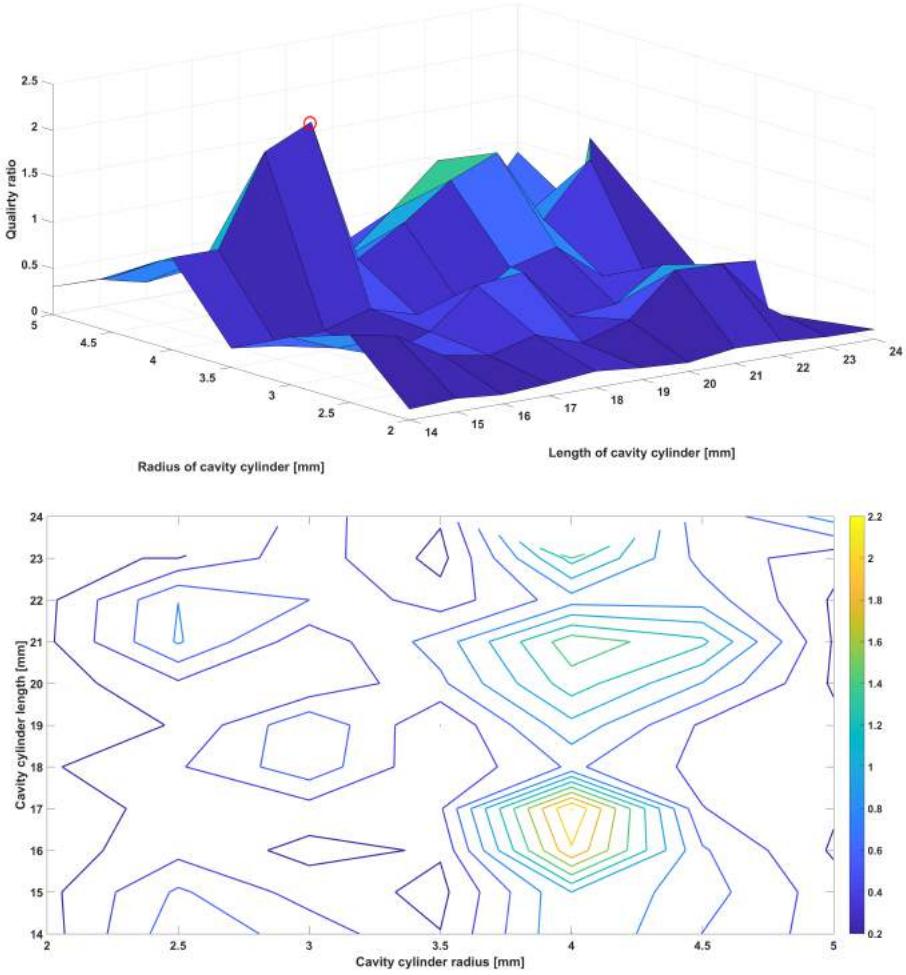

FIGURE 5.4: Top: Quality ratio of the different cavity cylinder parameter sweep combinations. The highlighted peak is the region with the highest increment. Below: contour plot of the cavity cylinder sweep. The color scale gives the values of the quality ratio

Generally, gradient based algorithms will lead to a local minimum, meaning that the optimal solution for a problem may not be found. Gradient-free algorithms do not require the objective function to be differentiable and are suitable for problems where the objective function is discrete, discontinuous or noisy [137]. The objective function is instead sampled at different positions within the search space.

A derivative free approach is selected for the optimization since the objective function is noisy. Changing the resonator geometry during the optimization generates different mesh elements that superimpose varying discretization errors on the objective function. The Monte-Carlo algorithm is selected for the optimization. The algorithm randomly samples points within the control variable search space with uniform distribution to obtain the optimal solution [137]. The algorithm explores the entire search space and as

Resonator parameters	Reference cylinder dimensions	Range of sweep	Increment step
Resonance cylinder length	8.1146	-	-
Resonance cylinder position	6.1067	5.5 – 6.5 11.5 - 14	0.5
Resonance cylinder radius	1.0105	-	-
Cavity cylinder length	15.2713	16.6 -17.3	0.1
Cavity cylinder radius	4. 00735	-	-
Absorption cylinder length	0.7681	-	-
Absorption cylinder radius	1.27055	-	-

TABLE 5.3: The resonator dimensions in mm used in the combined parameter sweep of both the cavity and resonance cylinder.

a result does not get stuck at a local minimum. This is particularly advantageous since the coarse parameter study indicate presence of numerous local minima.

The optimization problem is selected to maximize the objective function which in this case was pressure at the location of the microphone. The pressure is calculated using the VT-PML model described in the previous chapter between 48 kHz to 51 kHz since the resonance spans the entire frequency range. The results from the parameter sweep indicate that changing the cavity cylinder length together with the position and length of the resonance cylinder had the greatest PA signal increase. Furthermore, the results from the parameter sweep are used to reduce the optimization search space as shown in the Table 5.4. Typically, the optimization model would be imposed with constraints that limit the size of the radii of through which the laser beam propagates such that resonator wall excitations are avoided. This is not necessary in this work since the radii are already large enough to allow the laser beam to freely propagate without hitting the interior walls of the resonator.

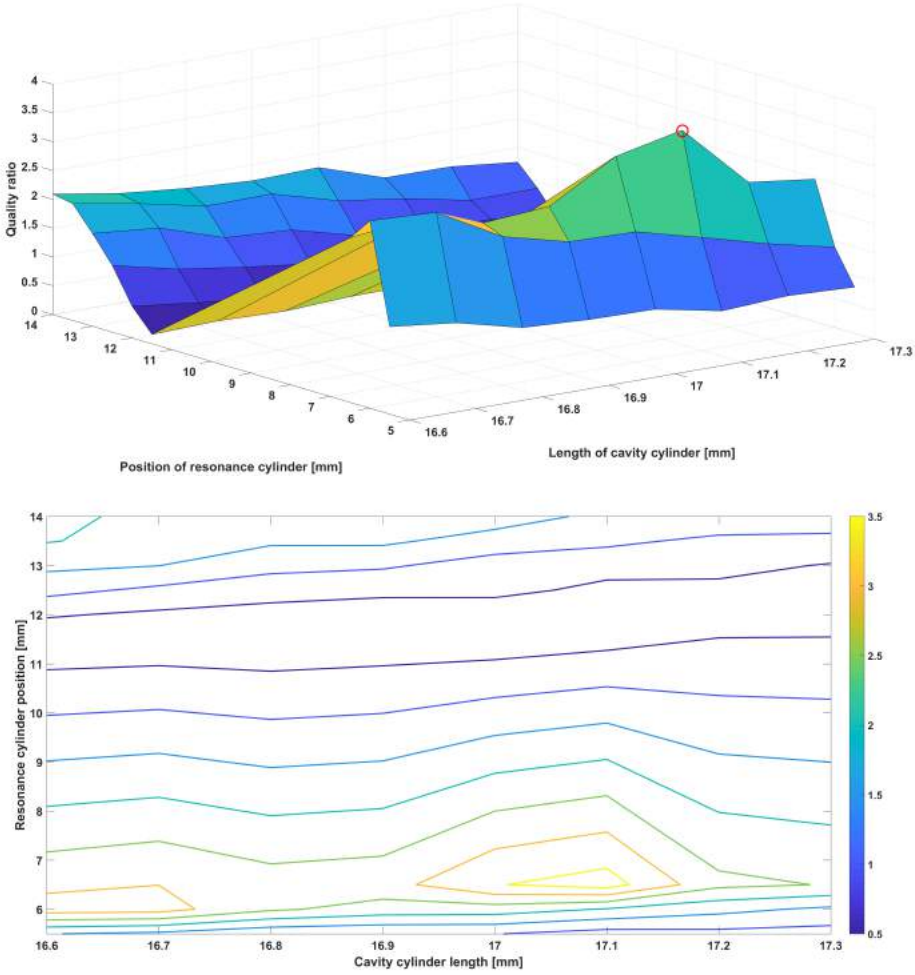

FIGURE 5.5: Top: quality ratio of the parameter sweep of the resonance cylinder position with the cavity cylinder length. The highlighted peak is the region with the highest increment. Below: contour plot of the cavity cylinder sweep. The color scale gives the values of the quality ratio

5.4 Optimization results

The results of the optimization showed the strength of the signal increased by a factor of 7.23. The optimized resonator has a cavity cylinder length of 17.146 mm, a resonance cylinder length of 1.1195 mm and its position 6.7924 mm away from the open end. The peak resonance frequency is at 49.2 kHz. Since the resonance results from the merging of two close resonances, comparing the quality factor is not possible due to difficulty in resolving the two resonances. The pressure distribution plot of the optimized resonator at 49.2 kHz is shown in Figure 5.6. From the plot, the antinode of the generated pressure wave is situated at the position of the microphone diaphragm which is important for detecting a high signal.

Resonator parameters	Reference cylinder dimensions	Range of variables
Resonance cylinder length	8.1146	1 - 8
Resonance cylinder position	6.1067	6 - 8
Resonance cylinder radius	1.0105	-
Cavity cylinder length	15.2713	16.9 - 17.2
Cavity cylinder radius	4. 00735	-
Absorption cylinder length	0.7681	-
Absorption cylinder radius	1.27055	-

TABLE 5.4: The resonator dimensions in mm used in the optimization.

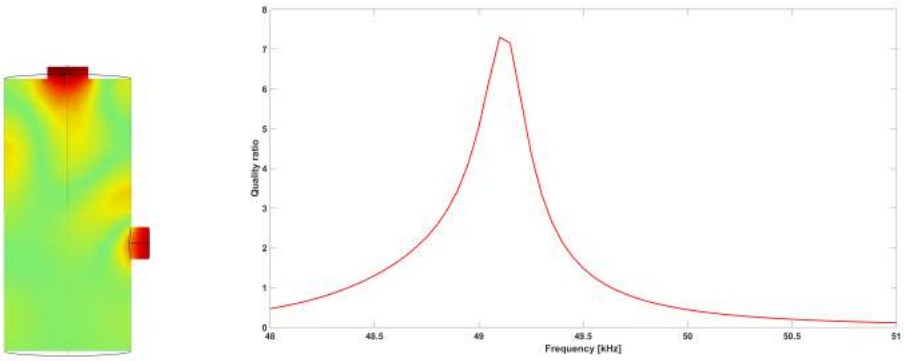

FIGURE 5.6: Left:the pressure distribution plot of the optimized resonator. Red indicates antinodes of the pressure wave. Right: Quality ratio of the optimized resonator.

The optimized resonator is manufactured by drilling the cylinders from a block of stainless steel. The tolerance of the resonator production process is 0.01 mm which hinders the development of a resonator with the exact dimensions as the ones obtained from the optimization. The dimensions of the new resonator are rounded off to account for the production limits. A cross-sectional view of the manufactured resonator and it's geometric dimensions are seen in Figure 5.7.

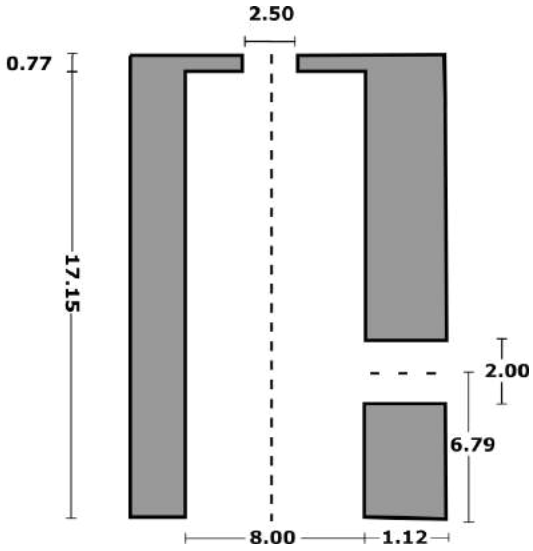

FIGURE 5.7: Schematic of the cross-section of optimized resonator dimensions (white). The dashed lines represent cylindrical symmetry.

The optimization results are verified by experimentally measuring the resonator frequency response using a DFB QCL as the optical excitation source and the carbon black sample. Furthermore, PA simulations of the produced resonator are performed using the three different approaches of simulating the PA signal in open resonators.

5.4.1 Simulation of optimized resonator

The frequency response plots of the produced resonator using the VT-PML, VT-BEM and AME-PML approaches is shown in Figure 5.8. The AME-PML simulation is performed with frequency intervals of 10 Hz. The VT-PML and VT-BEM simulations are performed at intervals of 300 Hz. All three approaches predict similar spectral features. The plots indicate that the resonance with a peak at 49 kHz has the highest amplitude with the other resonances diminished in comparison, thus confirming the optimization of the resonator. The peak resonance frequency of the optimized resonance is shifted from 49.2 kHz to 49 kHz and the quality ratio has decreased from 7.23 to 4.587. This difference is expected since the resonator dimensions are rounded off. Despite the decrease, the signal strength of the new resonator is an improvement compared to the original resonator dimensions.

5.4.2 Measurement of optimized resonator

The results from the measurement of the open reference resonator using the DFB QCL against the VT-PML simulation results are shown in Figure 5.8 for

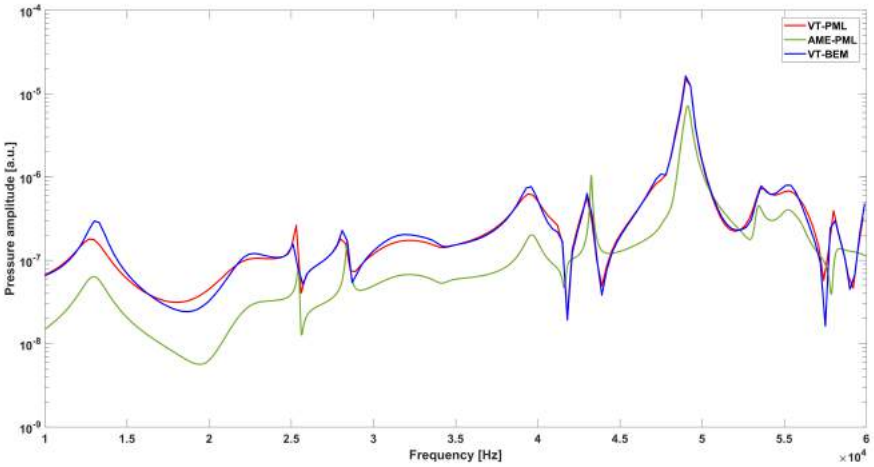

FIGURE 5.8: Frequency response plot of the optimized resonator dimensions using the three different simulation approaches

the resonance of interest. The signal to noise ratio of the measurement is 22.988. The measurements and the simulations had similar spectra features.

Figure 5.9 is the reference response plot of the produced resonator measured using the DFB QCL against the simulation results using the VT-PML and VT-BEM approach. The measurement is normalized according to the average laser output power. The measurement and the simulations show fairly good accordance. The strongest resonance in both the measurements and the simulations spans a wide frequency range between 45 kHz to 51 kHz, however, the peak resonance frequency is shifted in the measurements from 49 kHz (simulation) to 48.3 kHz. This is mainly attributed to damping effects that have been discussed in the previous section. The simulation resonances with weak amplitudes are hard to discern in the measurement due to the high base noise level. The measured amplitude of the optimized resonator was found to be 2.34 times stronger than the amplitude of the reference resonator.

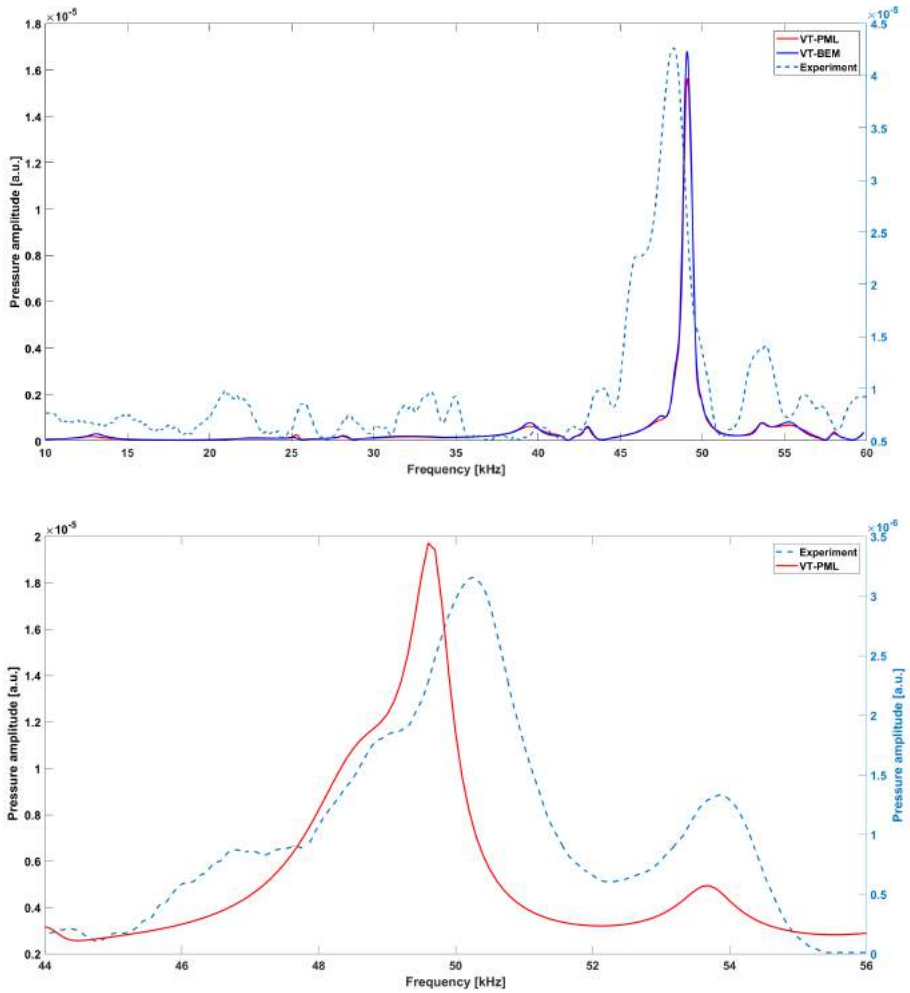

FIGURE 5.9: Frequency response plot of the optimized resonator dimensions

Chapter 6

Conclusion and outlook

This work is aimed at contributing to the development of a non-invasive photoacoustic sensor for blood glucose measurements by tackling the problem of the so far low detection sensitivity. The focus is to improve the qualitative performance of the photoacoustic resonator employed during the measurements by optimizing its geometry for maximum signal amplification using finite element modelling. This is because resonance amplification is strongly dependent on the shape and geometry of the resonator.

In the first step, finite element modelling of the photoacoustic signal from a solid sample is demonstrated for the first time. The signal is modelled inside a macroscopic closed T-shaped resonator using the VT and AME models. The ability of the AME model to accurately simulate the PA signal in the ultrasound region is demonstrated for the first time. This is significant since the method is computationally less demanding compared to the VT model and hence provides a faster alternative for PA simulation. The models provide a good framework for modelling the photoacoustic signal inside complex resonators shapes where simple simulation models like the transmission line model fails. The framework can be applied by engineers and scientists to further optimize closed PA resonators and in the design of new resonators.

The established models are then extended to an open resonator configuration using perfectly matched layers (PML) and boundary element method (BEM). The performance of the VT-PML approach to simulate the PA signal is demonstrated for the first time in the ultrasound range using solid sample. Additionally, two new approaches are for the first time presented for simulating the PA signal of open resonators using the AME-PML and VT-BEM. Their performance is analyzed and validated in both the audio and ultrasound range. The AME-PML approach stands out due to its computational speed however, it is susceptible to damping from the PML which lowers its accuracy. Therefore, the AME-PML can provide quick and approximate simulation results. The VT-BEM approach is shown to be approximately 5 times faster than the VT-PML approach while providing almost the same degree of accuracy. The three approaches provide engineers tasked with designing and optimizing open PA resonators different simulation options. Furthermore, the methods can be modified for gaseous samples and applied to resonators

of different geometry.

The procedure for the shape optimization of the T-shaped resonator is described using the Monte-carlo method that employed VT-PML approach to simulate the PA signal. To my knowledge, this is the first time the VT-PML method has been used for optimization of open PA resonators. The simulation results are confirmed experimentally and demonstrated that the signal strength is increased by a factor of 2.34 compared to the reference resonator. Given that with the reference cell glucose levels were detected in vivo to around 50 mg/dl, the increased signal strength from the optimization will further improve the sensitivity of the method to levels that are acceptable for sensor development.

In the future, in vivo glucose measurements using a pulsed QCL and the optimized resonator are recommended to determine the improvement in the sensitivity of the method and the detection limits of the method. Since resonances with narrow widths are more susceptible to temperature and humidity changes, a temperature and humidity sensor can be implemented into the resonator to track and calibrate for fluctuations that may occur during measurements. This will further improve the stability of the method.

The experimental setup used in this work can be improved further. A micro-controller can be integrated in the set up for processing and recording the digital output from the MEMS microphone. The microphone is adapted for such an application which would eliminate the need for using a low pass filter circuit for signal demodulation and the bulky lock-in-amplifier. A micro-controller would improve the sensitivity of the detection set up which is significantly lowered by the digital to analogue signal conversion using the low pass filter circuit. Furthermore, a micro-controller would enable miniaturization of the overall set up.

The resonator can still be further optimized since not all the geometrical parameters were investigated. The improvement of the signal strength is not mutually independent of other resonator geometries. Therefore, there is an opportunity for further resonator optimization. Complete investigations of all the resonator geometrical combinations requires a lot of computational power and with the increase in computational capabilities such an optimization could be possible in the near future. In addition, the overall signal improvement is limited by the manufacturing tolerances due to the inability to manufacture extremely precise resonators. However, with the increasing development of 3D printing such precise manufacturing would be possible. As such, a topology optimization investigation could be performed to search for new non-intuitive design solutions that result in much higher signal improvement.

Further improvement in the sensitivity can be accomplished by developing a MEMS microphone that has a resonance coinciding with the resonance of the resonator as demonstrated by Sim et al. [72].

Appendix A

MEMS microphone PCB

The PCB is held on the resonator surface by screwing it at the holes X1. The MEMS microphone is placed at K1 while the temperature and pressure sensor located at K2. C1 and C2 represent the condenser for the microphone and temperature and pressure sensor respectively.

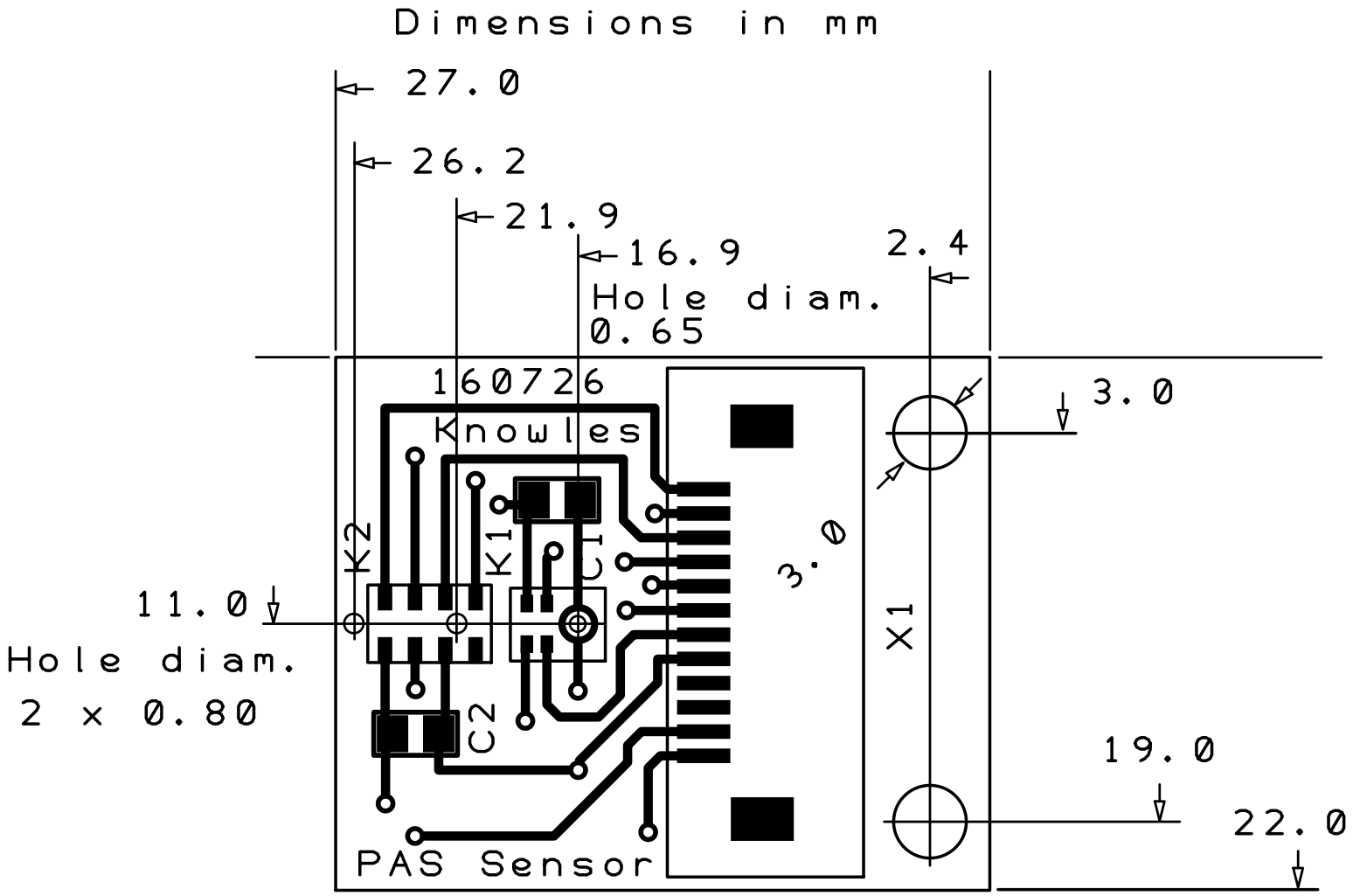
Dimensions in mm
27.0
26.2
21.9
16.9
2.4
Hole diam.
0.65
160726
Knowles
3.0
K2
K1
C1
3.0
X1
11.0
Hole diam.
2 x 0.80
C2
19.0
22.0
PAS Sensor

Bibliography

[1] W. H. Organisation. (). "Diabetes," [Online]. Available: https://www.who.int/news-room/fact-sheets/detail/diabetes. (accessed: 17.03.2020).

[2] T. Battelino, I. Conget, B. Olsen, I. Schütz-Fuhrmann, E. Hommel, R. Hoogma, U. Schierloh, N. Sulli, J. Bolinder, and t. S. S. Group, "The use and efficacy of continuous glucose monitoring in type 1 diabetes treated with insulin pump therapy: A randomised controlled trial," *Diabetologia*, vol. 55, no. 12, p. 3155, Dec. 2012. DOI: 10.1007/s00125-012-2708-9.

[3] M. Breton, A. Farret, D. Bruttomesso, S. Anderson, L. Magni, S. Patek, C. D. Man, J. Place, S. Demartini, S. D. Favero, C. Toffanin, C. Hughes-Karvetski, E. Dassau, H. Zisser, F. J. Doyle, G. D. Nicolao, A. Avogaro, C. Cobelli, E. Renard, B. Kovatchev, and o. b. o. T. I. A. P. (S. Group, "Fully integrated artificial pancreas in type 1 diabetes: Modular closed-loop glucose control maintains near normoglycemia," *Diabetes*, vol. 61, no. 9, pp. 2230–2237, Sep. 1, 2012, ISSN: 0012-1797, 1939-327X. DOI: 10.2337/db11-1445.

[4] B. M. Frier, "Morbidity of hypoglycemia in type 1 diabetes," *Diabetes Research and Clinical Practice*, Dietary management of diabetes and the challenges of intensive blood glucose control, vol. 65, S47–S52, Sep. 1, 2004, ISSN: 0168-8227. DOI: 10.1016/j.diabres.2004.07.008.

[5] D. M. Nathan, "Long-term complications of diabetes mellitus," *New England Journal of Medicine*, vol. 328, no. 23, pp. 1676–1685, Jun. 10, 1993, ISSN: 0028-4793. DOI: 10.1056/NEJM199306103282306.

[6] I. L. Jernelv, K. Milenko, S. S. Fuglerud, D. R. Hjelme, R. Ellingsen, and A. Aksnes, "A review of optical methods for continuous glucose monitoring," *Applied Spectroscopy Reviews*, vol. 54, no. 7, pp. 543–572, Aug. 9, 2019, ISSN: 0570-4928. DOI: 10.1080/05704928.2018.1486324.

[7] Diabetes Control and Complications Trial Research Group, D. M. Nathan, S. Genuth, J. Lachin, P. Cleary, O. Crofford, M. Davis, L. Rand, and C. Siebert, "The effect of intensive treatment of diabetes on the development and progression of long-term complications in insulin-dependent diabetes mellitus," *The New England Journal of Medicine*, vol. 329, no. 14, pp. 977–986, 1993, ISSN: 0028-4793. DOI: 10.1056/NEJM199309303291401.

[8] G. van den Berghe, P. Wouters, F. Weekers, C. Verwaest, F. Bruyninckx, M. Schetz, D. Vlasselaers, P. Ferdinande, P. Lauwers, and R. Bouillon, "Intensive insulin therapy in critically ill patients," *The New England Journal of Medicine*, vol. 345, no. 19, pp. 1359–1367, Nov. 8, 2001, ISSN: 0028-4793. DOI: 10.1056/NEJMoa011300.

[9] V. V. Tuchin, *Handbook of Optical Sensing of Glucose in Biological Fluids and Tissues*. CRC Press, Dec. 22, 2008, ISBN: 978-1-58488-975-5.

[10] Z. Zhao, "Pulsed photoacoustic techniques and glucose determination in human blood and tissue," Doctoral Dissertation, University of Oulu, Faculty of Technology, Department of Electrical Engineering and Infotech Oulu, May 24, 2002.

[11] G. B. Christison and H. A. MacKenzie, "Laser photoacoustic determination of physiological glucose concentrations in human whole blood," *Medical and Biological Engineering and Computing*, vol. 31, no. 3, pp. 284–290, May 1, 1993, ISSN: 1741-0444. DOI: 10.1007/BF02458048.

[12] J. P. Auses, S. L. Cook, and J. T. Maloy, "Chemiluminescent enzyme method for glucose," *Analytical Chemistry*, vol. 47, no. 2, pp. 244–249, Feb. 1, 1975, ISSN: 0003-2700. DOI: 10.1021/ac60352a008.

[13] J. Illingworth, "Methods of enzymatic analysis: Third edition: Editor-in-chief: Hans ulrich bergmeyer. verlag chemie, 1983 (vols i–III), 1984 (vols IV & v) DM258 each volume or DM2240 vols i–x inclusive," *Biochemical Education*, vol. 13, no. 1, pp. 38–38, 1985, ISSN: 1879-1468. DOI: https://doi.org/10.1016/0307-4412(85)90136-0.

[14] W. Villena Gonzales, A. T. Mobashsher, and A. Abbosh, "The progress of glucose monitoring—a review of invasive to minimally and non-invasive techniques, devices and sensors," *Sensors (Basel, Switzerland)*, vol. 19, no. 4, Feb. 15, 2019, ISSN: 1424-8220. DOI: 10.3390/s19040800.

[15] M. Shokrekhodaei and S. Quinones, "Review of non-invasive glucose sensing techniques: Optical, electrical and breath acetone," *Sensors (Basel, Switzerland)*, vol. 20, no. 5, Feb. 25, 2020, ISSN: 1424-8220. DOI: 10.3390/s20051251.

[16] J. C. Pickup, F. Hussain, N. D. Evans, and N. Sachedina, "In vivo glucose monitoring: The clinical reality and the promise," *Biosensors & Bioelectronics*, vol. 20, no. 10, pp. 1897–1902, Apr. 15, 2005, ISSN: 0956-5663. DOI: 10.1016/j.bios.2004.08.016.

[17] H. von Lilienfeld-Toal, M. Weidenmüller, A. Xhelaj, and W. Mäntele, "A novel approach to non-invasive glucose measurement by mid-infrared spectroscopy: The combination of quantum cascade lasers (QCL) and photoacoustic detection," *Vibrational Spectroscopy*, A Collection of Papers Presented at the 3rd International Conference "Shedding Light on Disease: Optical Diagnostics for the New Millenium (SPEC 2004", Newark, NJ, USA, 19-23 June 2004. Dedicated to Professor Henry Mantsch, vol. 38, no. 1, pp. 209–215, Jul. 29, 2005, ISSN: 0924-2031. DOI: 10.1016/j.vibspec.2005.02.025.

[18] H. D. Park, K. J. Lee, H. R. Yoon, and H. H. Nam, "Design of a portable urine glucose monitoring system for health care," *Computers in Biology and Medicine*, vol. 35, no. 4, pp. 275–286, May 1, 2005, ISSN: 0010-4825. DOI: 10.1016/j.compbiomed.2004.02.003.

[19] A. S. Panchbhai, "Correlation of salivary glucose level with blood glucose level in diabetes mellitus," *Journal of Oral & Maxillofacial Research*, vol. 3, no. 3, e3, 2012, ISSN: 2029-283X. DOI: 10.5037/jomr.2012.3303.

[20] S. Iguchi, H. Kudo, T. Saito, M. Ogawa, H. Saito, K. Otsuka, A. Funakubo, and K. Mitsubayashi, "A flexible and wearable biosensor for tear glucose measurement," *Biomedical Microdevices*, vol. 9, no. 4, pp. 603–609, Aug. 2007, ISSN: 1387-2176. DOI: 10.1007/s10544-007-9073-3.

[21] J. T. Baca, D. N. Finegold, and S. A. Asher, "Tear glucose analysis for the noninvasive detection and monitoring of diabetes mellitus," *The Ocular Surface*, vol. 5, no. 4, pp. 280–293, Oct. 2007, ISSN: 1542-0124. DOI: 10.1016/s1542-0124(12)70094-0.

[22] M. J, W. D, F. I, W. B, and P. R. (May 2012). "Correlation between sweat glucose and blood glucose in subjects with diabetes," Diabetes technology & therapeutics.

[23] S. Delbeck, T. Vahlsing, S. Leonhardt, G. Steiner, and H. M. Heise, "Non-invasive monitoring of blood glucose using optical methods for skin spectroscopy-opportunities and recent advances," *Analytical and Bioanalytical Chemistry*, vol. 411, no. 1, pp. 63–77, Jan. 2019, ISSN: 1618-2650. DOI: 10.1007/s00216-018-1395-x.

[24] M. Pleitez, H. von Lilienfeld-Toal, and W. Mäntele, "Infrared spectroscopic analysis of human interstitial fluid in vitro and in vivo using FT-IR spectroscopy and pulsed quantum cascade lasers (QCL): Establishing a new approach to non invasive glucose measurement," *Spectrochimica Acta. Part A, Molecular and Biomolecular Spectroscopy*, vol. 85, no. 1, pp. 61–65, Jan. 2012, ISSN: 1873-3557. DOI: 10.1016/j.saa.2011.09.007.

[25] J. Kottmann, J. M. Rey, and M. W. Sigrist, "Mid-infrared photoacoustic detection of glucose in human skin: Towards non-invasive diagnostics," *Sensors*, vol. 16, no. 10, p. 1663, Oct. 2016. DOI: 10.3390/s16101663.

[26] E. Cengiz and W. V. Tamborlane, "A tale of two compartments: Interstitial versus blood glucose monitoring," *Diabetes Technology & Therapeutics*, vol. 11 Suppl 1, S11–16, Jun. 2009, ISSN: 1520-9156. DOI: 10.1089/dia.2009.0002.

[27] M. S. Boyne, D. M. Silver, J. Kaplan, and C. D. Saudek, "Timing of changes in interstitial and venous blood glucose measured with a continuous subcutaneous glucose sensor," *Diabetes*, vol. 52, no. 11, pp. 2790–2794, Nov. 2003, ISSN: 0012-1797. DOI: 10.2337/diabetes.52.11.2790.

[28] S. Gebhart, M. Faupel, R. Fowler, C. Kapsner, D. Lincoln, V. McGee, J. Pasqua, L. Steed, M. Wangsness, F. Xu, and M. Vanstory, "Glucose sensing in transdermal body fluid collected under continuous vacuum pressure via micropores in the stratum corneum," *Diabetes Technology & Therapeutics*, vol. 5, no. 2, pp. 159–166, Apr. 1, 2003, ISSN: 1520-9156. DOI: 10.1089/152091503321827812.

[29] M. J. Tierney, Y. Jayalakshmi, N. A. Parris, M. P. Reidy, C. Uhegbu, and P. Vijayakumar, "Design of a biosensor for continual, transdermal glucose monitoring," *Clinical Chemistry*, vol. 45, no. 9, pp. 1681–1683, Sep. 1, 1999, ISSN: 0009-9147. DOI: 10.1093/clinchem/45.9.1681.

[30] J. Kost, S. Mitragotri, R. A. Gabbay, M. Pishko, and R. Langer, "Transdermal monitoring of glucose and other analytes using ultrasound," *Nature Medicine*, vol. 6, no. 3, pp. 347–350, Mar. 2000, ISSN: 1546-170X. DOI: 10.1038/73213.

[31] S. Mitragotri, M. Coleman, J. Kost, and R. Langer, "Transdermal extraction of analytes using low-frequency ultrasound," *Pharmaceutical Research*, vol. 17, no. 4, pp. 466–470, Apr. 1, 2000, ISSN: 1573-904X. DOI: 10.1023/A:1007537222591.

[32] J. Li, T. Igbe, Y. Liu, Z. Nie, W. Qin, L. Wang, and Y. Hao, "An approach for noninvasive blood glucose monitoring based on bioimpedance difference considering blood volume pulsation," *IEEE Access*, vol. 6, pp. 51 119–51 129, 2018, Conference Name: IEEE Access, ISSN: 2169-3536. DOI: 10.1109/ACCESS.2018.2866601.

[33] S. K. Vashist and J. H. T. Luong, *Point-of-care Glucose Detection for Diabetic Monitoring and Management*. CRC Press, Jan. 12, 2017, 164 pp., Google-Books-ID: SvziDQAAQBAJ, ISBN: 978-1-315-34918-3.

[34] C. E. Ferrante do Amaral and B. Wolf, "Current development in noninvasive glucose monitoring," *Medical Engineering & Physics*, vol. 30, no. 5, pp. 541–549, Jun. 2008, ISSN: 1350-4533. DOI: 10.1016/j.medengphy.2007.06.003.

[35] J. J. Burmeister and M. A. Arnold, "Evaluation of measurement sites for noninvasive blood glucose sensing with near-infrared transmission spectroscopy," *Clinical Chemistry*, vol. 45, no. 9, pp. 1621–1627, Sep. 1999, ISSN: 0009-9147. DOI: 10.1093/clinchem/45.9.1621.

[36] K. H. Hazen, M. A. Arnold, and G. W. Small, "Measurement of glucose in water with first-overtone near-infrared spectra," *Applied Spectroscopy*, vol. 52, no. 12, pp. 1597–1605, Dec. 1, 1998.

[37] J. Liu, R. Liu, and K. Xu, "Accuracy of noninvasive glucose sensing based on near-infrared spectroscopy," *Applied Spectroscopy*, vol. 69, no. 11, pp. 1313–1318, Nov. 2015, ISSN: 1943-3530. DOI: 10.1366/14-07728.

[38] J. T. Olesberg, M. A. Arnold, C. Mermelstein, J. Schmitz, and J. Wagner, "Tunable laser diode system for noninvasive blood glucose measurements," *Applied Spectroscopy*, vol. 59, no. 12, pp. 1480–1484, Dec. 2005, ISSN: 0003-7028. DOI: 10.1366/000370205775142485.

[39] A. Tura, A. Maran, and G. Pacini, "Non-invasive glucose monitoring: Assessment of technologies and devices according to quantitative criteria," *Diabetes Research and Clinical Practice*, vol. 77, no. 1, pp. 16–40, Jul. 2007, ISSN: 0168-8227. DOI: 10.1016/j.diabres.2006.10.027.

[40] R. J. McNichols and G. L. Coté, "Optical glucose sensing in biological fluids: An overview," *Journal of Biomedical Optics*, vol. 5, no. 1, pp. 5–16, Jan. 2000, ISSN: 1083-3668. DOI: 10.1117/1.429962.

[41] J. Yadav, A. Rani, V. Singh, and B. M. Murari, "Prospects and limitations of non-invasive blood glucose monitoring using near-infrared spectroscopy," *Biomedical Signal Processing and Control*, vol. 18, pp. 214–227, Apr. 1, 2015, ISSN: 1746-8094. DOI: 10.1016/j.bspc.2015.01.005.

[42] M. Ibrahim, M. Allam, H. Elhaes, and A. Leon, "Analysis of the structure and vibrational spectra of glucose and fructose," *Ecl. Quim., Sao Paulo*, vol. 31, Mar. 7, 2006. DOI: 10.1590/S0100-46702006000300002.

[43] A. M. K. Enejder, T. G. Scecina, J. Oh, M. Hunter, W.-C. Shih, S. Sasic, G. L. Horowitz, and M. S. Feld, "Raman spectroscopy for noninvasive glucose measurements," *Journal of Biomedical Optics*, vol. 10, no. 3, p. 031 114, Jun. 2005, ISSN: 1083-3668. DOI: 10.1117/1.1920212.

[44] J. Shao, M. Lin, Y. Li, X. Li, J. Liu, J. Liang, and H. Yao, "In vivo blood glucose quantification using raman spectroscopy," *PloS One*, vol. 7, no. 10, e48127, 2012, ISSN: 1932-6203. DOI: 10.1371/journal.pone.0048127.

[45] N. Li, H. Zang, H. Sun, X. Jiao, K. Wang, T. C.-Y. Liu, and Y. Meng, "A noninvasive accurate measurement of blood glucose levels with raman spectroscopy of blood in microvessels," *Molecules (Basel, Switzerland)*, vol. 24, no. 8, Apr. 17, 2019, ISSN: 1420-3049. DOI: 10.3390/molecules24081500.

[46] J. L. Lambert, C. C. Pelletier, and M. Borchert, "Glucose determination in human aqueous humor with raman spectroscopy," *Journal of Biomedical Optics*, vol. 10, no. 3, p. 031 110, Jun. 2005, ISSN: 1083-3668. DOI: 10.1117/1.1914843.

[47] M. Kinnunen and Z. Zhao, "Pulsed photoacoustic techniques and glucose determination in human blood and tissue," pp. 419–455, Dec. 1, 2008. DOI: 10.1201/9781584889755.ch14.

[48] C. Chou, C. Y. Han, W. C. Kuo, Y. C. Huang, C. M. Feng, and J. C. Shyu, "Noninvasive glucose monitoring in vivo with an optical heterodyne polarimeter," *Applied Optics*, vol. 37, no. 16, pp. 3553–3557, Jun. 1, 1998, ISSN: 1559-128X. DOI: 10.1364/ao.37.003553.

[49] B. H. Malik and G. L. Coté, "Real-time, closed-loop dual-wavelength optical polarimetry for glucose monitoring," *Journal of Biomedical Optics*, vol. 15, no. 1, p. 017 002, Feb. 2010, ISSN: 1560-2281. DOI: 10.1117/1.3290819.

[50] B. H. Malik, C. W. Pirnstill, and G. L. Coté, "Dual-wavelength polarimetric glucose sensing in the presence of birefringence and motion artifact using anterior chamber of the eye phantoms," *Journal of Biomedical Optics*, vol. 18, no. 1, p. 17 007, Jan. 2013, ISSN: 1560-2281. DOI: 10.1117/1.JBO.18.1.017007.

[51] J. S. Baba, B. D. Cameron, S. Theru, and G. L. Coté, "Effect of temperature, pH, and corneal birefringence on polarimetric glucose monitoring in the eye," *Journal of Biomedical Optics*, vol. 7, no. 3, pp. 321–328, Jul. 2002, ISSN: 1083-3668. DOI: 10.1117/1.1484163.

[52] S. F. Malin, T. L. Ruchti, T. B. Blank, S. N. Thennadil, and S. L. Monfre, "Noninvasive prediction of glucose by near-infrared diffuse reflectance spectroscopy," *Clinical Chemistry*, vol. 45, no. 9, pp. 1651–1658, Sep. 1999, ISSN: 0009-9147.

[53] K. Maruo, M. Tsurugi, M. Tamura, and Y. Ozaki, "In vivo noninvasive measurement of blood glucose by near-infrared diffuse-reflectance spectroscopy," *Applied Spectroscopy*, vol. 57, no. 10, pp. 1236–1244, Oct. 2003, ISSN: 0003-7028. DOI: 10.1366/000370203769699090.

[54] J. S. Maier, S. A. Walker, S. Fantini, M. A. Franceschini, and E. Gratton, "Possible correlation between blood glucose concentration and the reduced scattering coefficient of tissues in the near infrared," *Optics Letters*, vol. 19, no. 24, pp. 2062–2064, Dec. 15, 1994, ISSN: 1539-4794. DOI: 10.1364/OL.19.002062.

[55] M. Kohl, M. Cope, M. Essenpreis, and D. Böcker, "Influence of glucose concentration on light scattering in tissue-simulating phantoms," *Optics Letters*, vol. 19, no. 24, pp. 2170–2172, Dec. 15, 1994, ISSN: 0146-9592. DOI: 10.1364/ol.19.002170.

[56] K. V. Larin, M. S. Eledrisi, M. Motamedi, and R. O. Esenaliev, "Noninvasive blood glucose monitoring with optical coherence tomography," *Diabetes Care*, vol. 25, no. 12, pp. 2263–2267, 2002, ISSN: 0149-5992. DOI: 10.2337/diacare.25.12.2263.

[57] M. Friebel, J. Helfmann, and M. C. Meinke, "Influence of osmolarity on the optical properties of human erythrocytes," *Journal of Biomedical Optics*, vol. 15, no. 5, p. 055 005, Oct. 2010, ISSN: 1560-2281. DOI: 10.1117/1.3486542.

[58] Y. T. Lan, Y. P. Kuang, L. P. Zhou, G. Y. Wu, P. C. Gu, H. J. Wei, and K. Chen, "Noninvasive monitoring of blood glucose concentration in diabetic patients with optical coherence tomography," *Laser Physics Letters*, vol. 14, no. 3, p. 035 603, Feb. 2017, ISSN: 1612-202X. DOI: 10.1088/1612-202X/aa58c0.

[59] K. V. Larin, M. Motamedi, T. V. Ashitkov, and R. O. Esenaliev, "Specificity of noninvasive blood glucose sensing using optical coherence tomography technique: A pilot study," *Physics in Medicine and Biology*, vol. 48, no. 10, pp. 1371–1390, May 21, 2003, ISSN: 0031-9155. DOI: 10.1088/0031-9155/48/10/310.

[60] X. Guo, A. Mandelis, A. Matvienko, K. Sivagurunathan, and B. Zinman, "Wavelength-modulated differential laser photothermal radiometry for blood glucose measurements," *Journal of Physics: Conference Series*, vol. 214, p. 012 025, Mar. 1, 2010, ISSN: 1742-6596. DOI: 10.1088/1742-6596/214/1/012025.

[61] M. A. Pleitez, T. Lieblein, A. Bauer, O. Hertzberg, H. von Lilienfeld-Toal, and W. Mäntele, "In vivo noninvasive monitoring of glucose concentration in human epidermis by mid-infrared pulsed photoacoustic spectroscopy," *Analytical Chemistry*, vol. 85, no. 2, pp. 1013–1020, Jan. 15, 2013, ISSN: 1520-6882. DOI: 10.1021/ac302841f.

[62] J. Kottmann, J. M. Rey, J. Luginbühl, E. Reichmann, and M. W. Sigrist, "Glucose sensing in human epidermis using mid-infrared photoacoustic detection," *Biomedical Optics Express*, vol. 3, no. 4, pp. 667–680, Apr. 1, 2012, ISSN: 2156-7085. DOI: 10.1364/BOE.3.000667.

[63] "Selenium and the photophone 1," *Nature*, vol. 22, no. 569, pp. 500–503, Sep. 1, 1880, ISSN: 1476-4687. DOI: 10.1038/022500a0.

[64] W. H. Preece and W. Spottiswoode, "I. on the conversion of radiant energy into sonorous vibrations," *Proceedings of the Royal Society of London*, vol. 31, no. 206, pp. 506–520, Jan. 1, 1881. DOI: 10.1098/rspl.1880.0071.

[65] J. Tyndall, "III. action of an intermittent beam of radiant heat upon gaseous matter," *Proceedings of the Royal Society of London*, vol. 31, no. 206, pp. 307–317, Jan. 1, 1881. DOI: 10.1098/rspl.1880.0037.

[66] W. C. Röntgen, "Ueber töne, welche durch intermittirende bestrahlung eines gases entstehen," *Annalen der Physik*, vol. 248, no. 1, pp. 155–159, 1881, ISSN: 1521-3889. DOI: https://doi.org/10.1002/andp.18812480114.

[67] E. L. Kerr and J. G. Atwood, "The laser illuminated absorptivity spectrophone: A method for measurement of weak absorptivity in gases at laser wavelengths," *Applied Optics*, vol. 7, no. 5, pp. 915–921, May 1, 1968, ISSN: 1559-128X. DOI: 10.1364/AO.7.000915.

[68] F. J. M. Harren and S. M. Cristescu, "Photoacoustic spectroscopy in trace gas monitoring," in *Encyclopedia of Analytical Chemistry*, American Cancer Society, 2019, pp. 1–29, ISBN: 978-0-470-02731-8. DOI: 10.1002/9780470027318.a0718.pub3.

[69] M. W. Sigrist, S. Bernegger, and P. L. Meyer, "Infrared-laser photoacoustic spectroscopy," *Infrared Physics*, vol. 29, no. 2, pp. 805–814, May 1, 1989, ISSN: 0020-0891. DOI: 10.1016/0020-0891(89)90129-2.

[70] M. W. Sigrist, "Trace gas monitoring by laser-photoacoustic spectroscopy," *Infrared Physics & Technology*, Proceedings of the Sixth International Conference on Infrared Physics, vol. 36, no. 1, pp. 415–425, Jan. 1, 1995, ISSN: 1350-4495. DOI: 10.1016/1350-4495(94)00093-Z.

[71] P. Poulet and J. E. J. Chambron, "In vivo cutaneous specroscopy by photoacoustic detection," *Medical and Biological Engineering and Computing*, vol. 23, no. 6, pp. 585–588, Nov. 1, 1985, ISSN: 1741-0444. DOI: 10.1007/BF02455314.

[72] G. Puccetti, F. Lahjomri, and R. M. Leblanc, "Pulsed photoacoustic spectroscopy applied to the diffusion of sunscreen chromophores in human skin: The weakly absorbent regime," *Journal of Photochemistry and Photobiology B: Biology*, vol. 39, no. 2, pp. 110–120, Jun. 1, 1997, ISSN: 1011-1344. DOI: 10.1016/S1011-1344(96)00017-6.

[73] T. Watanabe, A. Tamura, Y. Yoshimura, and H. Nakazawa, "Determination of melanin in human hair by photoacoustic spectroscopy," *Analytical Biochemistry*, vol. 254, no. 2, pp. 267–271, Dec. 15, 1997, ISSN: 0003-2697. DOI: 10.1006/abio.1997.2429.

[74] J. McClelland, "Condensed matter photoacoustic spectroscopy and detection using gas phase signal generation," in *1980 Ultrasonics Symposium*, Nov. 1980, pp. 610–617. DOI: 10.1109/ULTSYM.1980.197471.

[75] R. B. Somoano, "Photoacoustic spectroscopy of condensed matter," *Angewandte Chemie International Edition in English*, vol. 17, no. 4, pp. 238–245, 1978, ISSN: 1521-3773. DOI: 10.1002/anie.197802381.

[76] C. Hernández-Aguilar, A. Domínguez-Pacheco, A. Cruz-Orea, and R. Ivanov. (Jan. 13, 2019). "Photoacoustic spectroscopy in the optical characterization of foodstuff: A review," Journal of Spectroscopy.

[77] A. Elia, P. M. Lugarà, C. Di Franco, and V. Spagnolo, "Photoacoustic techniques for trace gas sensing based on semiconductor laser sources," *Sensors*, vol. 9, no. 12, pp. 9616–9628, Dec. 2009. DOI: 10.3390/s91209616.

[78] J.-P. Besson, S. Schilt, and L. Thévenaz, "Multi-gas sensing based on photoacoustic spectroscopy using tunable laser diodes," *Spectrochimica Acta. Part A, Molecular and Biomolecular Spectroscopy*, vol. 60, no. 14, pp. 3449–3456, Dec. 2004, ISSN: 1386-1425. DOI: 10.1016/j.saa.2003.11.046.

[79] F. K. Tittel, D. Richter, and A. Fried, "Mid-infrared laser applications in spectroscopy," in *Solid-State Mid-Infrared Laser Sources*, ser. Topics in Applied Physics, I. T. Sorokina and K. L. Vodopyanov, Eds., Berlin, Heidelberg: Springer, 2003, pp. 458–529, ISBN: 978-3-540-36491-7. DOI: 10.1007/3-540-36491-9_11.

[80] D. C. Dumitraş, D. C. A. Dutu, C. Matei, A. M. Magureanu, M. Petrus, and C. Popa. (2007). "Laser photoacoustic spectroscopy: Principles, instrumentation, and characterization."

[81] M. Mannoor, J. Hwang, and S. Kang, "Numerical study of geometrical effects on the performance of an h-type cylindrical resonant photoacoustic cell," *Journal of Mechanical Science and Technology*, vol. 32, no. 12, pp. 5671–5683, Dec. 1, 2018, ISSN: 1976-3824. DOI: 10.1007/s12206-018-1114-8.

[82] D. Kumar, D. P. Ghai, and R. K. Soni, "Ultrasonic photoacoustic spectroscopy of trace hazardous chemicals using quantum cascade laser," *Optics Communications*, vol. 381, pp. 271–276, Dec. 15, 2016, ISSN: 0030-4018. DOI: 10.1016/j.optcom.2016.07.017.

[83] K. H. Michaelian, *Photoacoustic IR Spectroscopy: Instrumentation, Applications and Data Analysis*. John Wiley & Sons, Dec. 1, 2010, 404 pp., ISBN: 978-3-527-63321-0.

[84] C. B. Hirschmann, J. Uotila, S. Ojala, J. Tenhunen, and R. L. Keiski, "Fourier transform infrared photoacoustic multicomponent gas spectroscopy with optical cantilever detection:" *Applied Spectroscopy*, DOI: 10.1366/000370210790918490.

[85] W. L. Xia J Yao J. (). "Photoacoustic tomography: Principles and advances."

[86] K. Luft, W. Schaefer, and G. Wiebleb, "50 jahre NDIR-gasanalyse," *Technische Messen*, vol. 60, pp. 363–371, 1993.

[87] J. Kottmann, U. Grob, J. M. Rey, and M. W. Sigrist, "Mid-infrared fiber-coupled photoacoustic sensor for biomedical applications," *Sensors*, vol. 13, no. 1, pp. 535–549, Jan. 2013. DOI: 10.3390/s130100535.

[88] X. Mao, P. Zheng, X. Wang, and S. Yuan, "Breath methane detection based on all-optical photoacoustic spectrometer," *Sensors and Actuators B: Chemical*, vol. 239, pp. 1257–1260, Feb. 1, 2017, ISSN: 0925-4005. DOI: 10.1016/j.snb.2016.09.132.

[89] H. Bruhns, Y. Saalberg, and M. Wolff, "Photoacoustic hydrocarbon spectroscopy using a mach-zehnder modulated cw OPO," *Sensors and Transducers*, vol. 188, pp. 40–47, May 1, 2015.

[90] H. Bruhns, M. Wolff, Y. Saalberg, and K. M. Spohr, "Quantitative evaluation of broadband photoacoustic spectroscopy in the infrared with an optical parametric oscillator," *Sensors (Basel, Switzerland)*, vol. 18, no. 11, Nov. 15, 2018, ISSN: 1424-8220. DOI: 10.3390/s18113971.

[91] S. El-Busaidy, B. Baumann, M. Wolff, L. Duggen, and H. Bruhns, "Experimental and numerical investigation of a photoacoustic resonator for solid samples: Towards a non-invasive glucose sensor," *Sensors (Basel, Switzerland)*, vol. 19, no. 13, Jun. 29, 2019, ISSN: 1424-8220. DOI: 10.3390/s19132889.

[92] A. Rosencwaig and A. Gersho, "Theory of the photoacoustic effect with solids," *Journal of Applied Physics*, vol. 47, no. 1, pp. 64–69, Jan. 1, 1976, ISSN: 0021-8979. DOI: 10.1063/1.322296.

[93] J. Kottmann, J. M. Rey, and M. W. Sigrist, "New photoacoustic cell design for studying aqueous solutions and gels," *Review of Scientific Instruments*, vol. 82, no. 8, p. 084 903, Aug. 1, 2011, ISSN: 0034-6748. DOI: 10.1063/1.3622154.

[94] A. Miklós, P. Hess, and Z. Bozóki, "Application of acoustic resonators in photoacoustic trace gas analysis and metrology," *Review of Scientific Instruments*, vol. 72, no. 4, pp. 1937–1955, Mar. 27, 2001, ISSN: 0034-6748. DOI: 10.1063/1.1353198.

[95] L. V. Wang, "Tutorial on photoacoustic microscopy and computed tomography," *IEEE Journal of Selected Topics in Quantum Electronics*, vol. 14, no. 1, pp. 171–179, Jan. 2008, Conference Name: IEEE Journal of Selected Topics in Quantum Electronics, ISSN: 1558-4542. DOI: 10.1109/JSTQE.2007.913398.

[96] J. Xia, J. Yao, and L. V. Wang, "Photoacoustic tomography: Principles and advances," *Electromagnetic waves (Cambridge, Mass.)*, vol. 147, p. 1, 2014, Publisher: NIH Public Access.

[97] Y. Gotshal, I. Adam, and A. Katzir, "Glucose measurements in solutions using fiber optic evanescent wave spectroscopy and tunable CO2 laser," in *Surgical-Assist Systems*, vol. 3262, International Society for Optics and Photonics, Jun. 5, 1998, pp. 192–196. DOI: 10.1117/12.309483.

[98] M. Meinke, G. Müller, H. Albrecht, C. Antoniou, H. Richter, and J. Lademann, "Two-wavelength carbon dioxide laser application for in-vitro blood glucose measurements," *Journal of Biomedical Optics*, vol. 13, no. 1, p. 014 021, Feb. 2008, ISSN: 1083-3668. DOI: 10.1117/1.2870093.

[99] S. Haidar, K. Miyamoto, and H. Ito, "Generation of tunable mid-IR (5.5–9.3 microm) from a 2-microm pumped ZnGeP2 optical parametric oscillator," *Optics Communications*, vol. 241, no. 1, pp. 173–178, Nov. 1, 2004, ISSN: 0030-4018.

[100] S. Yu, D. Li, H. Chong, C. Sun, H. Yu, and K. Xu, "In vitro glucose measurement using tunable mid-infrared laser spectroscopy combined with fiber-optic sensor," *Biomedical Optics Express*, vol. 5, no. 1, pp. 275–286, Dec. 17, 2013, ISSN: 2156-7085. DOI: 10.1364/BOE.5.000275.

[101] Y. Ma and D. Liang, "<!– *** custom HTML *** –>tunable and frequency stabilized CO_2 waveguide laser," *Optical Engineering*, vol. 41, no. 12, pp. 3319–3323, Dec. 2002, ISSN: 0091-3286, 1560-2303. DOI: 10.1117/1.1518033.

[102] L. Hvozdara, N. Pennington, M. Kraft, M. Karlowatz, and B. Mizaikoff, "Quantum cascade lasers for mid-infrared spectroscopy," *Vibrational Spectroscopy*, Papers Presented at the 1st International Conference on Advanced Vibrational Spectroscopy, Turku, Finland, August 19-24, 2001, vol. 30, no. 1, pp. 53–58, Sep. 18, 2002, ISSN: 0924-2031. DOI: 10.1016/S0924-2031(02)00038-3.

[103] M. R. Moldover, J. P. M. Trusler, T. J. Edwards, J. B. Mehl, and R. S. Davis, "Measurement of the universal gas constant r using a spherical acoustic resonator," *Physical Review Letters*, vol. 60, no. 4, pp. 249–252, Jan. 25, 1988. DOI: 10.1103/PhysRevLett.60.249.

[104] M. Niu, Q. Liu, K. Liu, Y. Yuan, and X. Gao, "Temperature-dependent characteristics of a photoacoustic detector," *Optik*, vol. 124, no. 16, pp. 2450–2454, Aug. 1, 2013, ISSN: 0030-4026. DOI: 10.1016/j.ijleo.2012.08.021.

[105] M. Szakáll, J. Csikós, Z. Bozóki, and G. Szabó, "On the temperature dependent characteristics of a photoacoustic water vapor detector for airborne application," *Infrared Physics & Technology*, vol. 51, no. 2, pp. 113–121, Oct. 1, 2007, ISSN: 1350-4495. DOI: 10.1016/j.infrared.2007.04.001.

[106] N. Barreiro, A. Peuriot, G. Santiago, and V. Slezak, "Water-based enhancement of the resonant photoacoustic signal from methane–air samples excited at 3.3 microm," *Applied Physics B*, vol. 108, no. 2, pp. 369–375, Aug. 1, 2012, ISSN: 1432-0649. DOI: 10.1007/s00340-012-5018-5.

[107] J. Hodgkinson and R. P. Tatam, "Optical gas sensing: A review," *Measurement Science and Technology*, vol. 24, 2013. DOI: 10.1088/0957-0233/24/1/012004.

[108] T. Starecki and A. Geras, "Improved open photoacoustic helmholtz cell," *International Journal of Thermophysics*, vol. 35, no. 11, pp. 2023–2031, Nov. 1, 2014, ISSN: 1572-9567. DOI: 10.1007/s10765-013-1479-y.

[109] F. G. C. Bijnen, J. Reuss, and F. J. M. Harren, "Geometrical optimization of a longitudinal resonant photoacoustic cell for sensitive and fast trace gas detection," *Review of Scientific Instruments*, vol. 67, no. 8, pp. 2914–2923, Aug. 1, 1996, ISSN: 0034-6748. DOI: 10.1063/1.1147072.

[110] M. A. Pleitez, T. Lieblein, A. Bauer, O. Hertzberg, H. von Lilienfeld-Toal, and W. Mäntele, "Windowless ultrasound photoacoustic cell for in vivo mid-IR spectroscopy of human epidermis: Low interference by changes of air pressure, temperature, and humidity caused by skin contact opens the possibility for a non-invasive monitoring of glucose in the interstitial fluid," *The Review of Scientific Instruments*, vol. 84, no. 8, p. 084 901, Aug. 2013, ISSN: 1089-7623. DOI: 10.1063/1.4816723.

[111] A. L. Ulasevich, A. V. Gorelik, A. A. Kouzmouk, and V. S. Starovoitov, "A miniaturized prototype of resonant banana-shaped photoacoustic cell for gas sensing," *Infrared Physics & Technology*, vol. 60, pp. 174–182, Sep. 1, 2013, ISSN: 1350-4495. DOI: 10.1016/j.infrared.2013.04.011.

[112] M. Pedersen and J. McClelland, "Optimized capacitive MEMS microphone for photoacoustic spectroscopy (PAS) applications," vol. 5732, pp. 108–121, Mar. 1, 2005, Conference Name: Quantum Sensing and Nanophotonic Devices II. DOI: 10.1117/12.597136.

[113] P. Patimisco, G. Scamarcio, F. K. Tittel, and V. Spagnolo, "Quartz-enhanced photoacoustic spectroscopy: A review," *Sensors*, vol. 14, no. 4, pp. 6165–6206, Apr. 2014. DOI: 10.3390/s140406165.

[114] G. Wissmeyer, M. A. Pleitez, A. Rosenthal, and V. Ntziachristos, "Looking at sound: Optoacoustics with all-optical ultrasound detection," *Light: Science & Applications*, vol. 7, no. 1, p. 53, Aug. 15, 2018, ISSN: 2047-7538. DOI: 10.1038/s41377-018-0036-7.

[115] R. Vonach, J. Buschmann, R. Falkowski, R. Schindler, B. Lendl, and R. Kellner, "Application of mid-infrared transmission spectrometry to the direct determination of glucose in whole blood:" *Applied Spectroscopy*, Aug. 30, 2016. DOI: 10.1366/0003702981944553.

[116] C. Vrančić, A. Fomichova, N. Gretz, C. Herrmann, S. Neudecker, A. Pucci, and W. Petrich, "Continuous glucose monitoring by means of mid-infrared transmission laser spectroscopyin vitro," *Analyst*, vol. 136, no. 6, pp. 1192–1198, Feb. 28, 2011, ISSN: 1364-5528. DOI: 10.1039/C0AN00537A.

[117] J. Kottmann, J. M. Rey, and M. W. Sigrist, "New photoacoustic cell with diamond window for mid-infrared investigations on biological samples," in *Photons Plus Ultrasound: Imaging and Sensing 2012*, vol. 8223, International Society for Optics and Photonics, Feb. 23, 2012, 82231A. DOI: 10.1117/12.905973.

[118] J. Y. Sim, C.-G. Ahn, C. Huh, K. H. Chung, E.-J. Jeong, and B. K. Kim, "Synergetic resonance matching of a microphone and a photoacoustic cell," *Sensors*, vol. 17, no. 4, p. 804, Apr. 2017. DOI: 10.3390/s17040804.

[119] P. M. Morse and K. Ingard, *Theoretical Acoustics*. Princeton University Press, Princeton, NJ, 1986, 740 pp., ISBN: 0-691-08425-4.

[120] C. MUltiphysics, *Acoustic module user's guide version 5.3*. [Online]. Available: www.comsol.com.

[121] B. Baumann, M. Wolff, B. Kost, and H. Groninga, "Finite element calculation of photoacoustic signals," *Applied Optics*, vol. 46, no. 7, pp. 1120–1125, Mar. 1, 2007, ISSN: 2155-3165. DOI: 10.1364/AO.46.001120.

[122] M. Tavakoli, A. Tavakoli, M. Taheri, and H. Saghafifar, "Design, simulation and structural optimization of a longitudinal acoustic resonator for trace gas detection using laser photoacoustic spectroscopy (LPAS)," *Optics & Laser Technology*, vol. 42, no. 5, pp. 828–838, Jul. 1, 2010, ISSN: 0030-3992. DOI: 10.1016/j.optlastec.2009.12.012.

[123] V. Zeninari, V. A. Kapitanov, D. Courtois, and Y. N. Ponomarev, "Design and characteristics of a differential helmholtz resonant photoacoustic cell for infrared gas detection," *Infrared Physics & Technology*, vol. 40, no. 1, pp. 1–23, Feb. 1, 1999, ISSN: 1350-4495. DOI: 10.1016/S1350-4495(98)00038-3.

[124] B. Parvitte, C. Risser, R. Vallon, and V. Zéninari, "Quantitative simulation of photoacoustic signals using finite element modelling software," *Applied Physics B*, vol. 111, no. 3, pp. 383–389, May 1, 2013, ISSN: 1432-0649. DOI: 10.1007/s00340-013-5344-2.

[125] B. Baumann, B. Kost, H. Groninga, and M. Wolff, "Eigenmode analysis of photoacoustic sensors via finite element method," *Review of Scientific Instruments*, vol. 77, no. 4, p. 044 901, Apr. 1, 2006, ISSN: 0034-6748. DOI: 10.1063/1.2186808.

[126] A. Glière, J. Rouxel, M. Brun, B. Parvitte, V. Zéninari, and S. Nicoletti, "Challenges in the design and fabrication of a lab-on-a-chip photoacoustic gas sensor," *Sensors*, vol. 14, no. 1, pp. 957–974, Jan. 2014. DOI: 10.3390/s140100957.

[127] B. Lang and A. Bergmann, "Design framework for a gas sensor based on an open photoacoustic resonator," in *2016 IEEE SENSORS*, Oct. 2016, pp. 1–3. DOI: 10.1109/ICSENS.2016.7808433.

[128] V. Gesellschaft, *VDI-Wärmeatlas*. Springer: Berlin/Heidelberg, Germany, 2002, 740 pp., ISBN: 978-3-662-10743-0.

[129] B. Baumann, M. Wolff, and M. Teschner, "Open photoacoustic cell for blood sugar measurement: Numerical calculation of frequency response," *arXiv:1507.05189 [physics]*, Jul. 18, 2015. arXiv: 1507.05189.

[130] J.-P. Berenger, "A perfectly matched layer for the absorption of electromagnetic waves," *Journal of Computational Physics*, vol. 114, no. 2, pp. 185–200, Oct. 1, 1994, ISSN: 0021-9991. DOI: 10.1006/jcph.1994.1159.

[131] S. Johnson, *Notes on perfectly matched layers (pmls)*. [Online]. Available: https://math.mit.edu/~stevenj/18.369/pml.pdf.

[132] S. A. S. El-Busaidy, B. Baumann, M. Wolff, and L. Duggen, "Modelling of open photoacoustic resonators," *Photoacoustics*, vol. 18, p. 100 161, Jun. 2020, ISSN: 2213-5979. DOI: 10.1016/j.pacs.2020.100161.

[133] S. Kirkup, "The boundary element method in acoustics: A survey," *Applied Sciences*, vol. 9, no. 8, p. 1642, Jan. 2019. DOI: 10.3390/app9081642.

[134] S. Kirkup and J. Yazdani, "A gentle introduction to the boundary element method in matlab/freemat," in *Proceedings of the 10th WSEAS international conference on Mathematical methods, computational techniques and intelligent systems*, ser. MAMECTIS'08, Stevens Point, Wisconsin, USA, Oct. 26, 2008, pp. 46–52, ISBN: 978-960-474-012-3.

[135] Engineering360. (). "Chapter 9.9: Quantum cascade lasers," [Online]. Available: https://www.globalspec.com/reference/13695/160210/chapter-9-9-quantum-cascade-lasers (visited on 11/26/2020).

[136] C. K. Lim and J. Lederle, "Validierung von photoakustischen zellen.," Master thesis report, Hamburg University of Applied Science, Hamburg, 2017.

[137] C. MUltiphysics, *Optimization module user's guide version 5.4*. [Online]. Available: www.comsol.com.

[138] V. Spagnolo, P. Patimisco, and F. K. Tittel, "15 - quartz-enhanced photoacoustic spectroscopy for gas sensing applications," in *Mid-infrared Optoelectronics*, ser. Woodhead Publishing Series in Electronic and Optical Materials, E. Tournié and L. Cerutti, Eds., Woodhead Publishing, Jan. 1, 2020, pp. 597–659, ISBN: 978-0-08-102709-7. DOI: 10.1016/B978-0-08-102709-7.00015-2.

[139] A. Miklós, S.-C. Pei, and A. H. Kung, "Multipass acoustically open photoacoustic detector for trace gas measurements," *Applied Optics*, vol. 45, no. 11, pp. 2529–2534, Apr. 10, 2006, ISSN: 2155-3165. DOI: 10.1364/AO.45.002529.

[140] K. Krzempek, A. Hudzikowski, A. Głuszek, G. Dudzik, K. Abramski, G. Wysocki, and M. Nikodem, "Multi-pass cell-assisted photoacoustic/photothermal spectroscopy of gases using quantum cascade laser excitation and heterodyne interferometric signal detection," *Applied Physics B*, vol. 124, no. 5, p. 74, Apr. 6, 2018, ISSN: 1432-0649. DOI: 10.1007/s00340-018-6941-x.

[141] A. Miklós, P. Hess, Á. Mohácsi, J. Sneider, S. Kamm, and S. Schäfer, "Improved photoacoustic detector for monitoring polar molecules such as ammonia with a 1.53 microm DFB diode laser," *AIP Conference Proceedings*, vol. 463, no. 1, pp. 126–128, Mar. 15, 1999, ISSN: 0094-243X. DOI: 10.1063/1.58187.

[142] Y. Cai, N. Arsad, M. Li, and Y. Wang, "Buffer structure optimization of the photoacoustic cell for trace gas detection," *Optoelectronics Letters*, vol. 9, no. 3, pp. 233–237, May 1, 2013, ISSN: 1993-5013. DOI: 10.1007/s11801-013-3017-3.

[143] M. Wolff, B. Kost, and B. Baumann, "Shape-optimized photoacoustic cell: Numerical consolidation and experimental confirmation," *International Journal of Thermophysics*, vol. 33, no. 10, pp. 1953–1959, Nov. 1, 2012, ISSN: 1572-9567. DOI: 10.1007/s10765-012-1257-2.

[144] C. Risser, B. Parvitte, R. Vallon, and V. Zeninari, "Optimization and complete characterization of a photoacoustic gas detector," *Applied Physics B*, vol. 118, no. 2, pp. 319–326, Feb. 1, 2015, ISSN: 1432-0649. DOI: 10.1007/s00340-014-5988-6.

[145] M. I. Cotterell, G. P. Ward, A. P. Hibbins, J. M. Haywood, A. Wilson, and J. M. Langridge, "Optimizing the performance of aerosol photoacoustic cells using a finite element model. part 1: Method validation and application to single-resonator multipass cells," *Aerosol Science and Technology*, vol. 53, no. 10, pp. 1107–1127, Oct. 3, 2019, ISSN: 0278-6826. DOI: 10.1080/02786826.2019.1650161.

[146] M. I. Cotterell, G. P. Ward, A. P. Hibbins, A. Wilson, J. M. Haywood, and J. M. Langridge, "Optimizing the performance of aerosol photoacoustic cells using a finite element model. part 2: Application to a two-resonator cell," *Aerosol Science and Technology*, vol. 53, no. 10, pp. 1128–1148, Oct. 3, 2019, ISSN: 0278-6826. DOI: 10.1080/02786826.2019.1648749.

[147] R. Haouari, V. Rochus, L. Lagae, and X. Rottenberg, "Topology optimization of a 3d printed acoustic chamber for photoacoustic spectroscopy," in *2017 18th International Conference on Thermal, Mechanical and Multi-Physics Simulation and Experiments in Microelectronics and Microsystems (EuroSimE)*, Apr. 2017, pp. 1–5. DOI: 10.1109/EuroSimE.2017.7926292.